The Hong Kong Polytechnic University
Department of Building Services Engineering

Lightning-induced Impulse Magnetic Fields in High-rise Buildings

ZHOU QiBin

A thesis submitted in partial fulfillment of the requirements for the Degree of Doctor of Philosophy

February, 2007

Certificate of Originality

I hereby declare that this thesis is my own work and that, to the best of my knowledge and belief, it reproduces no material previously published or written, nor material that has been accepted for the award of any other degree or diploma, except where due acknowledgement has been made in the text.

ZHOU QiBin

Department of Building Services Engineering

The Hong Kong Polytechnic University

Hong Kong SAR, China

February, 2007

Abstract

Abstract of thesis entitled: Lightning-induced Impulse Magnetic Fields in High-rise Buildings

Submitted by : ZHOU QiBin

For the degree of : Doctor of Philosophy

at The Hong Kong Polytechnic University in February, 2007.

With the development of lightning protection system (LPS) installed in high-rise buildings, the probability of breakage on building due to lightning strokes has decreased to a very low level. However, the application of LPS imports another hazard to the electronic sensitive equipment in the high-rise buildings, i.e. lightning-induced impulse magnetic field (LIMF). This is because the working principle of a LPS is to attract lightning at their air terminals. An extremely large lightning current will flow through the downconductors of LPS into the earth. This current will generate an intense transient magnetic field around the downconductors inside the building. This transient magnetic field will bring serious electromagnetic interference to sensitive equipment inside the buildings, such as the malfunction or even destruction of sensitive electronic equipment, the over-voltage inside power and communication cables, the pace voltage and touching voltage to threaten human lives and so on. With the increasing application of electronic equipment and network in high-rise buildings in the past decade, such as computers network and telecommunication equipment, the hazard of LIMF becomes an important problem and proper measures should be taken to protect those properties and occupants against it.

Before seeking proper measures for the protection against LEMI, the lightning-induced electromagnetic environment (LIEE) inside buildings should be studied in advance. The previous studies on the LIEE inside the buildings protected by LPS focused on the conventional LPS which uses the internal metal structure of buildings as downconductors. Recently, the early emission streamer (ESE) LPS which uses isolated downconductors (e.g. coaxial cables) instead of the building structure is widely applied in modern high-rise buildings. Unlike the conventional LPS, large lightning currents are introduced into the buildings directly by the isolated downconductors. Then harsher LIEE will be induced around the buildings and greater threat will be imposed on properties and occupants. The issue of LIMF inside the building protected by the ESE LPS has been little addressed. In the previous studies, the building metal structures made of reinforcing bars were considered as a wire-grid structure. Recently, metal plates, e.g. metal decking, are widely adopted in the construction of high-rise buildings. The issues of modeling the building structure with metal plates and characterization of LIMF around the structure have been little addressed.

In this thesis, the equivalent circuit (EC) modeling approach for a high-rise building installed with the ESE LPS is proposed. The corresponding solution procedure in the time domain is developed by using Electromagnetic Transient Program (EMTP). With the modeling approach and corresponding solution procedure, LIMF inside a typical building in Hong Kong was evaluated and characterized. Furthermore, empirical formulas for evaluating the shielding effect of a gridlike building structure with an isolated downconductor were derived by the curve fitting technique. With these formulas, the shielding effect against the structure dimension, the grid width and the distance between downconductor and structure, could be evaluated quickly.

For metal plates, a partial element equivalent circuit (PEEC) modeling approach was proposed and the corresponding solution procedure in the frequency domain was developed in this thesis. The PEEC modeling approach of metal plates was integrated with the EC modeling approach for the wire-grid structure. A novel modeling technique, named as the hybrid analytical-numerical equivalent circuit (HANEC) modeling technique, was proposed. With the HANCE modeling technique, LIMF inside a scaled wire-plate structure were characterized. In order to validate the proposed EC modeling approach, the PEEC modeling approach and the HANEC modeling technique, a series of experiments conducted in laboratories were presented in this thesis.

From the characterization results of a typical building in Hong Kong, it is found that LIMF around the isolated downconductor is significantly high and the metal building structure can attenuate LIMF obviously. Some recommendations on the installation of a LPS and the placement of electrical and electronic equipment are provided and some measures to protect the sensitive systems and equipment in critical areas are also proposed. From the characterization results of a scaled wire-plate structure, it is found the building structure with metal plates has much better shielding effect than that without metal plates. From the validation experiments, it is found that the measured results agreed with the simulation results quite well.

With the proposed modeling approach and the corresponding solution procedure in this thesis, researchers can study LIMF as well as related issues in high-rise buildings, such as protection measures of critical equipment, induced-voltage in power and telecommunication cables. With the characterization results and empirical formulas, practicing engineers can assess the threat of LIMF to critical equipment in a high-rise building. So proper measures can be taken to protect the critical equipment, e.g.

placing critical equipment in safety areas and enclose critical equipment with proper shielding. Furthermore, under the guide of the work in this thesis, the architecture designer can optimize the design of a building structure to minimize LIMF radically.

Publications

I. Papers in Journals

- **QiBin Zhou** and Y. Du, 2005. Using EMTP for Evaluation of Surge Current Distribution in Metallic Gridlike Structures. ***IEEE Transaction on IAS***, Vol. 41, No. 4, pp. 1113-1117

- Y. Du and **QiBin Zhou**, 2005. Capacitance Matrix of the Screened/Isolated Single-Core Cables of Finite Length. ***IEE Proceedings: Science, Measurement and Technology***, Vol. 152, No. 5, Sept. pp. 233-239.

- Y. Du and **QiBin Zhou**, 2006. Analysis of Lightning-Induced Impulse Magnetic Fields in the Building with an Isolated Down Conductor. ***IEEJ Transactions on Fundamentals and Materials***, Vol. 126, No. 2, pp.71-77.

- L. Xu, Y. Du and **QiBin Zhou**, 2004. The Magnetic Field and Induced Current Arising from a Cylindrical Shell Loop with an Unbalanced Current. ***Electric Power System Research***, Vol. 71, Issue 1, Sept. 2004, pp: 21-26

- Y. Du, Lin Xu and **QiBin Zhou**, 2004, Magnetic Fields of a Cylindrical Shell Excited by an Unbalanced Current Source, ***HKIE Transactions***, Vol.11, No.13, pp:5-9

II. Papers in Conferences

- Y. Du and **QiBin Zhou**, 2007, Lightning-induced Magnetic Field in Buildings with Metallic Plates, ***13th International Conference on Atmospheric Electricity (ICAE)***, Aug. 13-17, Beijing, China

- **QiBin Zhou** and Y. Du, 2006, Using EMTP to Evaluate the Current Distribution in a Building Structure during a Lightning Strike with PEEC Modeling Approach. ***The 7th EMC Europe International Symposium***, OThC3-3, Sept. 4-8, Barcelona, Spain

- **QiBin Zhou** and Y. DU, 2006, Lightning Transient Analysis for DC Traction Power System of Electrified Railway by EMTP Simulation, ***IEEE / IAS 2006 41st Annual Meeting***, Oct. 8-12, Tampa, Florida, U.S.A

- **QiBin Zhou** and Y. Du, 2006, Numerical Evaluation of Magnetic Fields in the Presence of Non-ferromagnetic Plates. ***The Twelfth Biennial IEEE Conference on Electromagnetic Field Computation***, April 30-May 3, Miami, U.S.A

- **QiBin Zhou** and Y. Du, 2006, Numerical Analysis of the Charge Distribution on a Building Structure in the Preliminary Breakdown Phase of Lightning. ***The 17th International Zurich Symposium on Electromagnetic Compatibility***, No.FSC-273, Feb. 27-March 3, Singapore

- **QiBin Zhou** and Y. Du, 2004, Using EMTP for Evaluation of Surge Current Distribution in Metallic Gridlike Structures, ***IEEE/IAS 2004 39th Annual Meeting***, Oct. 3-7, Seattle, Washington, U.S.A

- **QiBin Zhou** and Y. Du, 2004, Numerical Evaluation of Magnetic Field inside a Typical Laboratory Struck by Lightning**.** ***Asia-Pacific Radio Science Conference (AP-RASC'01)***, Aug. 24-27, Qingdao, China

- **QiBin Zhou**, Y. Du and L. Xu, 2004, An Experimental Study of the Magnetic Field from a Coaxial Cable Carrying a Lightning Discharge Current. ***IEEE/DRPT Conference***, No. 151, April 5-8, Hong Kong, China

III. Submitted Papers

- Y. Du, **QiBin Zhou** and Mingli Chen, Lightning-induced Magnetic Fields in Buildings with Metallic Plates

- Y. Du and **QiBin Zhou**, Lightning Equivalent Circuit Approach for Evaluating Low-frequency Magnetic Fields in the Presence of Non-ferromagnetic Plates

Acknowledgements

I must express my grateful thanks to my Chief Supervisor, Dr. Du Yaping, and my Co-supervisor, Dr. Chen Mingli, from the Department of Building Services Engineering, The Hong Kong Polytechnic University, for their readily available supervisions, valuable suggestions, patient guidance, continuous helps and encouragements throughout the course of the work.

I highly appreciate senior instructor Mr. Leung Chun-sing and technician Mr. Fung Wing-kwong, Mr. Cheng Chak-kit, Mr. Lau Wai-pang and Mr. Leung Tat-wah in the department, for their assistance in laboratory work in Hong Kong. In addition, I also highly appreciate Prof. Fu Zhengcai from Shanghai Jiaotong University for providing great help in laboratory work in China. Finally, I would appreciate Dr. W. S. Meyer and Dr. Tsu-huei Liu in Portland, USA for their useful help during my research.

Finally I would like to express my deepest appreciation to my family and my beloved wife, Bian Xiaoyan, for their love, encouragement, moral support and understanding.

Table of Contents

List of Figures

List of Tables

Nomenclature

Variable	Description	Unit
R	Resistance	Ω
L	Inductance	H
C	Capacitance	F
P	Potential coefficient	Column/V
A	Vector magnetic potential	Wb/m
J	Current density	kg m^{-3} s^{-1}
U	Voltage	V
I	Current	A
B	Magnetic flux density	Tesla
H	Magnetic field intensity	A/m
E	Electric field intensity	V/m
D	Electric flux density	FV/m^2
V	Volume	m^3
f	Frequency	Hz
t	Time	second

Greek symbols

ϕ	Scalar electric potential	V
δ	Penetrating depth	meter
β	Phase constant	rad/m
λ	Wavelength	meter
ε	Dielectric constant	F/m

δ	Surface current density	A/m^2
μ	Permittivity	H/m
υ	Velocity of electromagnetic wave	m^2 s^{-1}
$\boldsymbol{\omega}$	Angular frequency	rad/second
σ	Surface charge density	C/m^2
t	Time	second
ρ	Resistivity	$\Omega \cdot \mathrm{m}$

Chapter 1

Introduction

1.1 Background

High-rise buildings are gradually becoming a land mark of modern metropolises like Hong Kong. Because of the increasing cost of lands in modern metropolises, a large number of people live and work in high-rise buildings. The safety of occupants and equipment should be guaranteed under various dangerous situations. The lightning strokes to a high-rise building are a serious hazard, which not only damage the building itself, but also threaten the safety of occupants and equipment inside.

Since Franklin invented the lightning conductors in the 19th century, the damage of lightning strokes to buildings has been reduced significantly. With the development of lightning protection system (LPS) installed in high-rise buildings, the probability of breakage on building due to lightning strokes has decreased to a very low level. However, the application of LPS imports another hazard to the electronic sensitive equipment in the high-rise buildings, i.e. lightning-induced impulse magnetic field (LIMF). This is because the working principle of LPS is to attract lightning at their air terminals. An extremely large lightning current will flow through the downconductors of LPS into the earth. This current will generate an intense transient magnetic field around the downconductors inside the building. This transient magnetic field will bring serious electromagnetic interference to sensitive equipment inside the buildings, such as the malfunction or even destruction of sensitive electronic equipment, the over-voltage inside power and communication cables, the pace voltage and touching voltage to threaten human lives and so on. This kind of hazard from a lightning stroke has been ignored by public for a long time. With the increasing application of electronic equipment and network inside high-rise buildings in the past decade, such as computers network and telecommunication equipment, the hazard of LIMF becomes an important problem for construction engineers and stimulates the research interest of researchers.

1.2 Significance of this Thesis

To study protection concepts and provide mitigation methods against lightning electromagnetic interference (LEMI) in high-rise buildings, LIMF inside buildings should be investigated in advance.

The study of LIMF in buildings has been conducted for many years. The studies in the past years mainly focused on the building with the conventional LPS, which used the internal metal building structure as its downconductors. In modern high-rise buildings a new type of LPS, namely early streamer emission (ESE) LPS, is widely found. Unlike the conventional LPS, it uses isolated downconductors (e.g. coaxial cables) instead of the building structure to lead the lightning current into the earth. Unlike the conventional LPS, large lightning currents are introduced into the buildings directly by the isolated downconductors. Then harsher lightning-induced electromagnetic environment (LIEE) will be induced around the buildings and greater threat will be imposed on inside properties and occupants. The study on LIMF inside the building protected by the ESE LPS has been little addressed before.

In this thesis, a modeling approach with the corresponding solution procedure is provided for evaluating the current distribution and magnetic fields in the building with the ESE LPS. From the characterization of LIMF in a typical building, recommendations are provided for practical engineers for the protection of sensitive equipment against LEMI. The empirical formulas for evaluating the shielding effect of a wire-grid structure against LIMF are also derived in this thesis, which can help practicing engineers to access the threat of LIMF to sensitive equipment efficiently.

In the previous studies, the internal building structure was considered as a wire-grid structure made from reinforcing concrete (RC) bars inside such components as columns, beams, walls and so on. With the development of the construction technology in modern high-rise buildings, large metal plates, e.g. metal decking, are widely applied. The modeling approaches, the solution procedure and the characterization results in those studies are not applicable for a building with a wire-plate structure any more. The study on LIMF in such buildings has been little addressed until present. In this thesis, a modeling approach with the corresponding solution procedure is developed for the metal plates in buildings. Based on this modeling approach, a special modeling technique is proposed for a wire-plate structure under a direct lightning stroke. From the characterization of LIMF inside a scaled wire-plate structure, recommends for protection of sensitive equipment are provided.

1.3 Objectives and Outcomes of this Thesis

Although the studies on lightning-induced electromagnetic environments in buildings have been conducted for years, those studies are not available for modern high-rise buildings due to the introduction of new LPS, e.g. the ESE LPS, and the introduction of metal plates, e.g. decking, in modern buildings. In order to seek proper and reliable protection for sensitive equipment against lightning electromagnetic interference in modern buildings, a study on LIEE in high-rise buildings is conducted in this thesis. The objectives of this thesis are identified, as follows:

- To propose a modeling approach for the wire-grid structure of a building with the ESE LPS, and develop the corresponding solution procedure for evaluating the current distribution as well as the magnetic fields.

- To characterize LIMF inside a typical building in Hong Kong.

- To provide empirical formulas for evaluating the shielding effect of a wire-grid building structure.

- To propose a modeling approach for a building structure with large metal plates, and develop the corresponding solution procedure for evaluating the current distribution as well as the magnetic fields.

- To characterize LIMF in a scaled model of the building structure with metal plates.

- To validate the proposed modeling approach by experiments in laboratories.

To propose a modeling approach for the wire-grid structure of a building with the ESE LPS is the first objective of this thesis. Although the equivalent circuit approach proposed in literatures is applicable for modeling the building structure, the model of the high voltage coaxial cable which is used as the isolated downconductor in the ESE LPS is built and integrated with the model of building structure. In order to increase the solution efficiency, a solution procedure in the time domain is required to be developed.

In order to provide recommendations for practicing engineers to protect sensitive electronic equipment against LIMF, characterization of LIMF distribution inside a reinforcing steel building installed with different types of LPS is conducted in this thesis. The empirical formulas for evaluating the shielding effect of a wire-grid structure against LIMF are derived in this thesis.

In order to study LIMF in buildings with large metal plates, a modeling approach for metal plates is developed in this thesis. This modeling approach can be integrated with the modeling approach of RC bars to study LIMF in the building. For a direct lightning stroke at the wire-plate structure, a special modeling technique is provided.

The proposed modeling approaches of the wire-grid structure and the wire-plate structure are validated experimentally in the laboratories. Four validation experiments are introduced in this thesis.

1.4 Outlines of this Thesis

Chapter 1 introduces the background of the research conducted in this thesis, and presents the objectives of this thesis.

Chapter 2 describes briefly the metal structures in modern buildings, and lightning protection systems installed in the local buildings. The hazard of lightning electromagnetic interference is addressed. A critical review on the approaches for modeling building structures in literature is provided. The results in the prevail studies on modeling high-voltage coaxial cables, metal plates as well as on modeling lightning stroke are addressed.

Chapter 3 addresses the approaches for modeling a wire-grid building structure and the high voltage coaxial cable used as an isolated downconductor in the ESE LPS. Then a solution procedure in the time domain is developed by adopting Electromagnetic Transient Program (EMTP) with some modifications.

Chapter 4 addresses a characterization of LIMF in a reinforcing concrete building in Hong Kong. The results in the building with the convention LPS and the ESE LPS are compared. Recommendations are provided for practical engaging for the protection of sensitive equipment against LEMI.

Chapter 5 presents a preliminary study on the relationships between the parameters of the metal structure and the shielding effect of the wire-grid structure in a building. Using the curve fitting technique and the induction procedure, a series of empirical formulas for evaluating the shielding effect are provided.

Chapter 6 describes an approach for modeling non-ferromagnetic plates as part of the building structure. A method for generating hybrid and orthogonal cells in the plates is proposed. A double exponential function is adopted to approximate the current distribution inside the plates. Finally the corresponding solution procedure is introduced.

Chapter 7 starts with the discussion on the integration of the modeling approaches of plates and RC bars for addressing LIMF in a building structure with metal plates. According to the observations from the preliminary study on the structure under a direct lightning stroke, a special modeling technique, named as the hybrid analytical-numerical equivalent circuit (HANEC) technique, is developed from the integrated modeling approach.

Chapter 8 addresses the characterization of LIMF inside a scaled building with the wire-plate structure using the HANEC modeling technique. The configuration of the wire-plate structure is introduced firstly. The magnetic field in the wire-plate structure is evaluated and compared with that from an independent downconductor.

The shielding effect of the wire-plate structure is revealed. Finally, the shielding effect of the wire-plate structure is compared with that of a wire-grid structure.

Chapter 9 presents a series of experiments for validating the proposed modeling approaches developed in this thesis. The equipment and measurement apparatuses which are used in these experiments are introduced firstly. The experiments for validating the modeling approaches of wire-grid structures, independent plates and wire-plate structures are described, respectively.

Chapter 10 summarizes the conclusions of the research works in this thesis and outlines the works to be carried out in the future.

Chapter 2

Review

2.1 High-rise Buildings and Lightning Protection Systems in Hong Kong

High-rise buildings are the landmark of Hong Kong, one of the biggest metropolises in the world. The International Finance Center II in the Center District of Hong Kong Island is the 6th tallest building in the world. The Center Plaza also located in the Center District is the tallest reinforcing concrete buildings in the world. These high-rise buildings are a natural response to fast-growing population, scarcity of land and high land costs in the metropolis as Hong Kong. With the advance of construction technology in building construction, two types of building structures are developed and widely applied. One is the reinforced concrete structure and the other is the steel skeleton structure [Wolfgang, 1995].

2.1.1 Meal Structures in High-rise Buildings

The metal structure is the skeleton of a modern building. It is used to enhance the mechanical strength of building components or directly support the load of the building itself and the other objects inside it, e.g. people and occupants. But it also plays an important role in the protection against lightning. The following is the brief review of the metal structure in buildings.

2.1.1.1 The Reinforced Concrete Structure

The reinforced concrete structure was originally applied to low buildings and was treated merely as a substitute for steel. In the later 20th century, this type structure was also widely developed in high-rise buildings. This type of building structure contains columns, beams, floors, load-bearing walls and precast slabs. Some of them are presented in the following photos which were taken by the author of this thesis.

Figure 2.1 Column structure

Figure 2.1 shows the metal structure of a column which is made from a vertical bundle of reinforcing concrete (RC) bars. The steels bars are bonded to a rectangle steel coil at a fixed vertical interval.

Figure 2.2 Beam structure

Figure 2.2 illustrates the metal structure of beams, which is also made from a horizontal bundle of RC bars. These RC bars are also bonded with a rectangle coil at a fixed horizontal interval.

Figure 2.3 Floor structure

Figure 2.3 shows the metal structure at a floor. This structure looks like a horizontal mesh made of orthogonal RC bars. At each crossing position, two orthogonal RC bars are bonded with thin iron wires.

Figure 2.4 Wall structure

In reinforcing concrete buildings, there are load-bearing walls which carry the load of beams and floors. Figure 2.4 shows the metal structure at a load-bearing wall. It looks like a vertical mesh made of orthogonal RC bars, which will be bonded by thin iron wire at the crossing position.

Figure 2.5 Precast slab

In addition to above components, the precast slabs shows in Figure 2.5 are widely applied in buildings to enhance the construction efficiency. In these precast slabs, RC bars are buried inside slabs to enhance the mechanical strength.

Figure 2.6 Center Plaza with reinforced concrete structure

So in reinforcing concrete buildings, it is known that RC bars play an important role in constructing the building component to increase their mechanical strength. As mentioned above, the 374m-high, 78-story Central Plaza in Hong Kong Island, as Figure 2.6 shows, is one of the examples with reinforced concrete building structure.

2.1.1.2 The Steel Skeleton Structure

The steel skeleton structure is adopted in most of high-rise buildings in Hong Kong. With this structure, the skeleton carries most of the weight of the building, and the wall only serve to keep out the heat, cold, wind and rain. Then walls can be made thin, and can be made of quite light materials.

The main metalwork in this type of structure mainly includes steel columns, beams and girders, which are presented in the following photos which were taken by Raymond [Raymond, 1998 and Raymond, 2003].

Figure 2.7 Steel column

Figure 2.7 shows a vertical column in the steel skeleton structure of a high-rise building. It is observed that the steel columns are large in size because they bear the most load of the high-rise building.

Figure 2.8 Steel beams

Figure 2.8 shows the horizontal beams in the steel skeleton structure of a high-rise building. The H-shape beams are connected with steel columns steel and bear the load coming from the above floors.

Figure 2.9 Steel girders

Figure 2.9 illustrates steel girders of the steel skeleton structure of a high-rise building. The girders are used to support the load of upper floors together with the main columns.

Figure 2.10 Decking

In recently year, large metal plates are increasingly applied in high-rising building for construction, such as decking shown in Figure 2.10. The decking is supported on beams and used for constructing concrete floors.

Figure 2.11 IFC II with steel skeleton structure

It is noted that all the steel components in this type of building structure are interconnected with each other and form a gridlike metal structure or a grid plus plate metal structure if decking is applied. As mentioned early, the International Finance

Center II which is 420m high with 88 stories, as Figure 2.11 shows, is a typical example of this type of metal structure applied in Hong Kong.

2.1.2 Lightning Protection in High-rise Buildings

Since Hong Kong is located in an area with frequent lightning activities, lightning is considered as a significant threat to the high-rise buildings in Hong Kong. So lightning protection system (LPS) is required to be installed in the high-rise buildings to protect the human lives and properties in the buildings, It should be mentioned that that LPS can prevent physical damage by direct lightning strokes, it may not be effective in protection against the damage arisen by lightning-induced impulse magnetic field (LIMF).

The LPS in Hong Kong can be divided into two categories according to the design principles: one is the conventional LPS based on BS 6651 [BS 6651, 1999] and the other is the early streamer emission (ESE) LPS based on NFC 17-102 [French Standard NFC 17-102, 1995].

2.1.2.1 Conventional LPS

The conventional LPS is mainly adopted in government buildings due to its advantage of low cost, reliable and low earth resistance solution. The main components of the conventional LPS include the air termination, the downconductors and the earth termination.

Figure 2.12 shows the air termination. It is installed on the roof of a high-rise building, and is used to intercept lightning and deliver the lightning energy via dedicated conductors down to the earth. An air termination network, which may be formed by a number of interconnected horizontal and vertical conductors, is normally installed on the roof surface of a building.

Figure 2.12 Air terminations of conventional LPS

Downconductors are for providing a low-impedance path from the air termination to the earth termination. With these downconductors, a lightning current can be safely delivered to the earth. In the engineering practice, the internal metal structure of a building is usually adopted as the downconductors for saving the construction cost and simplifying the installation work of LPS. For the reinforcing concrete buildings, the RC bars inside the building components are interconnected. For a column through stories, one RC bar inside the bundle of a column section at different stories is firmly connected by welding. The other RC bars may be bonded with this dedicated RC bar by thin iron wires. The same measures are applied to the RC bars in beams. The orthogonal RC bars in columns and beamed are again connected by welding. As to the RC bars in wall and floors, they are bonded with the columns and beams with thin iron wires. Since bonding with iron wires has much larger resistance than melting, most lightning current will follow through the building structure. Then the building structure used as downconductors can be simplified as a structure only containing the dedicated RC bars in columns and beams. In the building with steel skeleton structure, the interconnected metalwork by melting and riveting can be used as downconductors directly, providing they are appropriately connected to the air and earth termination with good electrical conductivity.

Earth termination allows the lightning surge energy to be dissipated into the general mass of earth. In most cases, the termination is formed by a network, which is made of a number of interconnected earth electrodes shown in Figure 2.13. One earth electrode should be connected to each downconductor. The earth termination network should have a combined resistance to earth not exceeding 10 ohms with taking into account any bonding to other services.

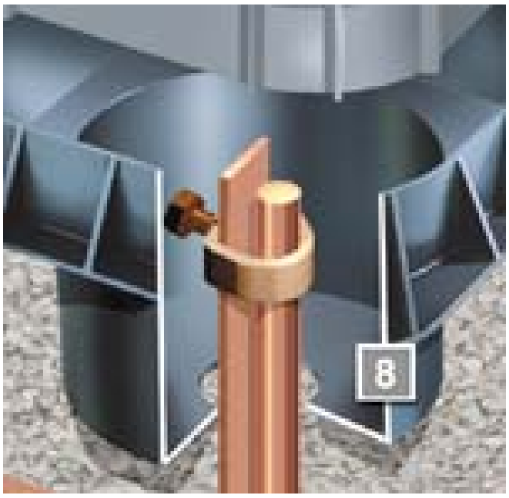

Figure 2.13 Earthing electrode of the conventional LPS

2.1.2.2 Early Streamer Emission LPS

In recent years, the ESE lightning protection system has been installed extensively in commercial buildings and other private sectors. According to the survey, almost 90% of private buildings in Hong Kong are equipped with the ESE LPS due to its low cost and easy installation.

Although the design of the ESE LPS varies from one brand name to another, the operating principles are more or less the same. The ESE LPS is characterized by their triggering advance, which is realized by using a special air termination shown in Figure 2.14. This type of air terminations can emit streamers before a lightning stroke happens and attract the stepped streamed from thundercloud to trigger a lightning stroke. As stated in the NFC 17-102 [French Standard NF C 17-102, 1995], the rod and the air termination tip should have a conductive cross-sectional area larger than 120mm^2 and be at least 2m higher than the objects to be protected.

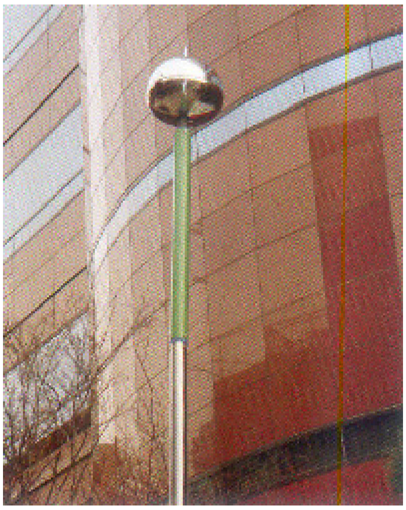

Figure 2.14 Air termination of the ESE LPS

The lightning conductor should be connected to the earth termination by at least one isolated downconductor such as high voltage coaxial cables and tri-axial cables shown in Figure 2.15. Two or more downconductors are required when the protected structure is higher than 28m or the horizontal projection of the conductor is large than its vertical projection. The downconductors are preferably installed outside the structure and their path should be as direct as possible.

Figure 2.15 High voltage coaxial cable used as a downconductor

One earth termination should be provided for each downconductor as Figure 2.16 shows. The resistance value of each earth termination should be 10 ohms or less. To minimize the back-electromotive force during the lightning discharge, single excessively long horizontal or vertical components should be avoided. Otherwise, the conductors of the earth termination should always be directed outward from the building.

Figure 2.16 Earth termination of the ESE LPS

2.2 Lightning Electromagnetic Interference in High-rise Buildings

The direct damage of lightning stroke to buildings is well known to people as a common sense. It can not only break the bodies of buildings, but also trigger a fire hazard to threaten the people and properties inside the buildings. With the protection of LPS, the direct damage of lightning stroke can be mostly avoided. But at the same time, LPS also leads in another kind of threat or even damage to the properties in buildings, which often lacks attention.

It has been mentioned in Section 1.2 that LPS is not to eliminate a lightning stroke but to attract a lightning stroke at its air terminals. So a large impulse current will flow from the thundercloud to LPS through the lightning channel in the space during a lightning stroke happens. Then this large current will be led into the earth through the downconductors of LPS. According to Faraday's Law, the large impulse current will generate intense impulse magnetic field and bring the lightning electromagnetic interference (LEMI) to sensitive equipment in buildings.

Large-area networks of computers and control systems are located in business and industry buildings. Electric apparatuses, such as the second-side equipment in power system, precise instruments, and family appliances, are widely distributed inside modern high-rise buildings. In the networks and apparatuses, large numbers of electronic components are applied. Since the electronic components generally have very weak signal levels, they are sensitive to LEMI and may be damaged in harsh electromagnetic environment as Figure 2.17 shows. Another study has also revealed that when the impulse magnetic field exceeded 2.9mT, the keyboard and the mouse port were damaged permanently [Shi et.al., 2003].

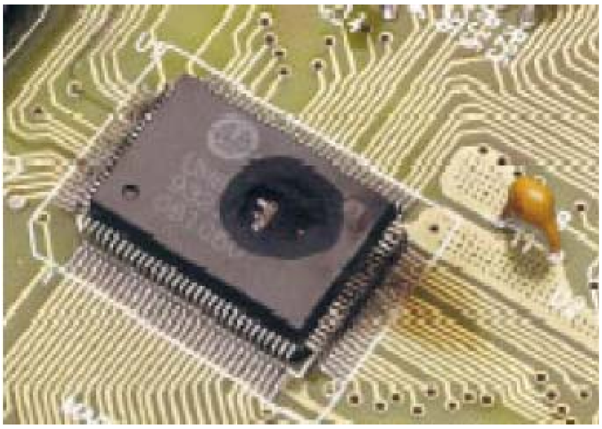

Figure 2.17 Damage of electronic component due to LEMI

In addition, the harsh LEMI can not only induce over-voltages in power cables which will endanger the cable insulation, but also induce abnormal signals in telecommunication cables which will disturb the normal operation of communication and even damage the equipment. What's more, the injected lightning current may generate a significant voltage between any two positions of feet or between the positions of hand and foot of a person. This voltage is a threat to personal safety.

2.3 Modeling Approach for Buildings Installed with the Conventiaonal LPS

The lightning electromagnetic field is a threat to sensitive equipment in high-rise buildings. It has been addressed for decades for the purpose of protection of sensitive equipment in buildings. In those studies, modeling buildings under a lightning stroke is the most critical issue. Almost all of the studies in literatures focused on the buildings with the reinforcing concrete structure. This building structure which was used as the downconductors was converted into a scaled and simple wire-grid model. Based on this wire-grid model, different numerical modeling approaches were proposed for evaluation and characterization of lightning-induced electromagnetic field inside the buildings.

The study of LIEE started in 1975 when Uman and his cooperators published a paper about evaluating the electromagnetic field radiated from finite antenna [Uman et.al., 1975]. They proposed a method and continuously developed it to evaluate the electromagnetic field due to the lightning channel knowing the current distribution along the channel [Uman and Rubinstein, 1988; Rubinstein and Uman, 1991]. In 1992, Uman's model was been adopted by S. Cristina to compute the electromagnetic field inside the buildings installed the conventional LPS [Cristina and Orlandi, 1992]. After that, the evolution of the voltage and current distribution in the building structure was conducted by various numerical modeling approaches. These approaches can be basically classified into three catalogs, i.e. the equivalent circuit approach, the field approach and the partial element equivalent circuit (PEEC) approach.

2.3.1 The Equivalent Circuit Approach

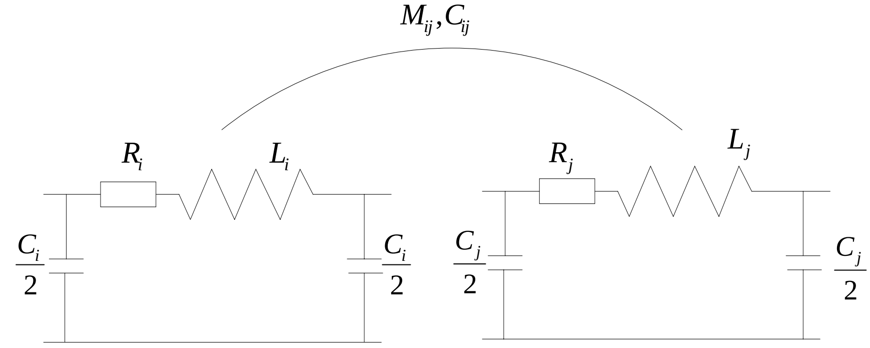

Figure 2.18 Coupled π-type circuit

The equivalent circuit approach is a simplified approach for modeling the building structures. With this modeling approach, each branch of the building structure and the 'victim' circuit are divided into a suitable number of elements to take account of propagation phenomena and all the branches are considered to be coupled together.

Each element is models as a π-type circuit with coupling to another element, as shows in Figure 2.18.

By interconnecting the π-type model of each element, the building structure and the 'victim' circuit are simply modeled as an equivalent electrical network which is analyzed in the time domain or the frequency domain [Cristina and Orlandi, 1992; Orlandi, Piparo and Mazzetti, 1995; Orlandi, Piparo and Mazzetti, 1995; Orlandi, Mazzetti and et.al., 1998; Cortina and Porrino, 1992]. Then direct evaluation of the node voltages and the branch currents in building structure and victim circuit [Satori et.al., 1998; Beierl and Steinbigler, 1989; Orlandi, Piparo and Mazzetti, 1995; Buccella, 2003] is achieved in the equivalent network. With the voltages and induced currents, the electric fields and magnetic fields can be calculated by electric potential formula and the Bio-savart Law, respectively.

The equivalent circuit network built by the equivalent circuit modeling approach is made from a large number of capacitance and impedance. It is very important to calculate these parameters accurately because they are critical for evaluating voltages and currents as well as the consequent electromagnetic fields. In those studies in literatures, different methods to calculating these parameters have been proposed.

2.3.1.1 Methods for Capacitance Calculation

Generally speaking, there are about three methods to calculate the capacitance of branch elements in literatures. The first method is by calculating the potential at parallel electrical field plane for the infinite long horizontal filament conductor such as the transmission line in power system [Clayton, 2004]. The second method is named as average potential method [Du, 2001]. This method assumes that the charges distribute on the surface of conductor surface evenly. Then the average potential coefficient of the object conductor to the source conductor is calculated. The average potential method is available for finite length conductor. The third method is a numerical method which adopts the moment method to calculate the charge distribution on a conductor [Harrington, 1968; Rao et.al., 1984]. This method can consider the fringing effect of conductors which makes the uneven distribution of charges. It is most accurate but too complicated to be applied in a large network. As to a metal structure, when the distance of two conductors is much larger than its radius, the fringing effect can be ignored and the average potential method is applicable.

2.3.1.2 Methods for Impedance Calculation

A. Internal impedance calculation

The internal impedance includes the internal inductance and internal resistance. In most textbooks on power system engineering, the internal inductance is calculated under d.c. or very low frequency. For example, the well known formula to calculate the internal inductance of a straight solid cylindrical conductor is give by

$$L_{in} = \frac{\mu_0}{8\pi} \quad (H/m) \tag{2.1}$$

Formula (2.1) is derived under d.c. condition and only acceptable in analyses of only the fundamental frequency. In analyzing a transient problem, e.g. the lightning stroke, the voltage and current in the conductors are rich in high frequency components. The skin and proximity effects become significant. Then the formula (2.1) is not applicable. However, in most studies in literatures, the internal inductance was neglected because it is very small comparing to the external inductance.

The internal resistance is another part of the internal impedance of the conductor. The internal resistance of a solid cylindrical conductor can be calculated by the formulas presented in textbooks [Clayton, 2004]. For a tubular conductor its internal resistance can be calculated by Xulin's formula [Xu et.al., 2004].

In most literatures, the internal reactance is also ignored. From these formulas, it is noted that the resistance of a conductor is increasing considerably quickly with increasing frequency due to the skin effect while the internal inductance will decrease with increasing frequency.

B. External impedance calculation

The external impedance of a conductor can be separated into two components: external self impedance and mutual impedance. The external self impedance is generated by the magnetic linkage of its self current on the conductor itself. The mutual impedance is the ratio of the voltage drop per unit length in one conductor to the current flowing in the other conductor and returning through the earth. Because of the symmetry of the circuit, the mutual inductance between two conductors is identical. In literatures, a lot of formulas for calculating the external impedance of circular solid conductors have been proposed.

If the conductor is placed in an infinite space where there is no earth or the earth effect can be neglected, the formula presented in [Frederick, 1946] can be adopted to calculate the external self impedance and mutual impedance between two filament conductors of finite length. If the earth effect should be considered and the earth is considered to be perfect conductive, the formulas in the book [Clayton, 2004] and the paper [Cristina and Porrino, 1992] are available for an infinite long filament conductor by applying the image method. If the filament conductor is not long enough, the formula in the paper [Roger and White, 1990] based on Neumann's integration formula is more accurate. When the earth is not perfectly conductive, the earth effect can not simply considered by the image method. Section 2.2.3 has presented the discussed of the earth return circuit. In Roger's paper, Deri's theory is adopted and a revised image method was applied by adopting a new conception of complex penetrating depth of the earth.

2.3.2 The Field Approach

Although the equivalent circuit approach is very simple for application, it does not consider the radiation field inside the building structure, which may bring some error to the evaluation results for a steep lightning current waveform. In order to take induction and radiation field into consideration, another full-wave approach based on the electric field integral equation (EFIE) were proposed [Buccella et.al., 1992]. Since this approach was derived from the electromagnetic field theory, it is named as the field approach.

Since the building structure with the conventional LPS is made of interconnected RC bars, it can be simplified to a wire-grid structure when the thin-wire hypothesis is adopted. In the hypothesis, the RC bar elements are assumed to be thin and with uniform radius. It length should be less than 0.01λ (λ as the minimum wavelength related to the maximum frequency to be considered). As a consequence, the current on each element can be represented by a filament placed on its axis. In order to obtain an integral equation for the longitudinal currents, the following statement on the surface S of the generic wire can be used as a boundary condition

$$\overline{u} \cdot \left(E^{inc} + E^{sc} \right) = z_s I_a \qquad (2.2)$$

where z_s is the per-unit-length surface impedance of the element and $\bar{u}$ is the unit vector tangential to S in the direction of the axis of the element. I_a is the current inside the wire.

The left-hand side of (2.2) represents the tangential component of the total electric field, parallel to the axis of the wire, and E^{inc} is the incident electric field, namely the electric field in the absence of the wires structure, which is due to the lightning channel. E^{sc} is the scattered electric field due to the presence of the wire-grid structure. E^{sc} can be expressed by means of the retarded scalar potential ϕ and the vector potentials A

$$E^{sc} = -(j\omega A + \Delta\phi) \tag{2.3}$$

When the current continuity law is taken into account, the free electric charge is represented as a function of the current I_a as follows

$$\rho_s(l') = -\frac{1}{j\omega}\frac{dI_a(l')}{dl'} \tag{2.4}$$

Then the vector potentials A, the retarded scalar potential ϕ as well as $\nabla\phi$ are given as the functions of current, respectively

$$A = u\int_{wire} I_a(l')\, g(r, r')\, dl' \tag{2.5}$$

$$\phi = -\frac{1}{j\omega\varepsilon}\int_{wire}\frac{dI_a(l')}{dl'} g(r, r')\, dl' \tag{2.6}$$

$$\nabla\phi = \frac{\partial}{\partial l}\left[-\frac{1}{j\omega 4\pi\varepsilon}\int_{wire}\frac{dI_a(l')}{dl'} g(r, r')\, dl'\right] \tag{2.7}$$

where u is the magnetic permeability, σ is the conductivity, $\dot{\varepsilon} = \varepsilon_r \varepsilon_0 + \sigma / (j\omega)$ is the complex permittivity of the medium. l' is along the axis of the wire.

By substituting (2.5-2.7) into (2.3), the classical EFIE is obtained.

$$\begin{aligned} z_s I_a(r) = E^{inc}(r) - j\omega\Big[u\int_\Omega I_a(l')g(r,r')dl'\Big] \\ +\frac{\partial}{\partial l}\left[\frac{-1}{j4\pi\omega\varepsilon}\int_L \frac{dI_a(l')}{dl'}g(r,r')dl'\right] \end{aligned} \tag{2.8}$$

where Ω is the domain of integration, i.e., the building structure arrangement and the related images); L is the length of the wire under consideration; r and r' are the position vectors of the observation point and of the source point, respectively. $g(r,r')$ is the Green's function for an unbounded region with $k = \sqrt{-\omega^2 u\varepsilon}$ as the wave number.

$$g(r,r') = \frac{e^{-\dot{k}|r-r'|}}{4\pi |r-r'|} \tag{2.9}$$

In this way, the third term on the right-hand side of (2.8) represents the difference between the scalar potential values calculated at the ends of the wire under consideration.

Equation (2.8) is a classical expression of EFIE in the frequency domain. The numerical solution in terms of the longitudinal current distribution along the wires of the structure is based on the direct method of moments by introducing an appropriate discretization. By subdividing each branch into a number of segments having the same length, a discrete formulation of (2.8) can be obtained.

By introducing triangular basis functions, the unknown longitudinal current along the branches are formally piecewise linear and the unknowns are the set of longitudinal currents at both ends of each segment. In such a way, also by imposing the current continuity equation (i.e., Kirchhoff's Current Law) at each node of the wire-grid structure, the resolving matrix equation in the frequency domain is obtained.

After having computed the unknown longitudinal currents, the electric and magnetic fields could be calculated in any interesting point inside the building structure. The time-domain profiles for the electromagnetic quantities are obtained by using the invert Fourier transform technique.

2.3.3 Partial Element Electrical Circuit Approach

Although the field approach is more rigorous than the circuit approach, it is complicated to be applied and the numerical solution is only possible for practical engineering problems. Some researchers tried to combine the advantages of the equivalent circuit approach and the field approach and proposed a hybrid approach, namely the partial element equivalent circuit (PEEC) approach.

The PEEC approach was originally proposed by Ruehli for modeling of three-dimensional multi-conductor systems in electronic systems, such as the integrated circuit packages and wires or conductors located on dielectric layers with remote ground planes [Ruehli, 1974]. This approach is based on an electric field integral equation (EFIE) that is interpreted in terms of circuit elements. The circuit elements including the partial inductances and partial capacitances can be found from computer solutions [Ruehli et.al., 1993]. A general purpose network analysis program is then used to obtain voltages and currents in the time domain or the frequency domain. Compared with the equivalent circuit approach and the field approach, the PEEC approach provides a more comprehensive interpretation of the relations between the circuit theory and the field theory and extends an integral equation solution to inductance computations including capacitance [Ruehli, 1972].

Due to the advantage of the PEEC approach, Antonini and his cooperators introduced it to model the building structure for the study on the LIEE in the building installed with the conventional LPS [Antonini et.al., 1998]. In this study, the building structure was considered as a wire-grid structure made of RC bars. The lightning channel was also models as a vertical straight antenna. The ground was simplified as a perfect conductive plane and the image method was applied. The equivalent circuit network of the building was interpreted to a matrix equation which was solved in the frequency domain by reducing its order. In addition, their study included the coupling between the building structure and communication cables by integrating the cables into the PEEC model of the building structure.

2.4 Modeling Approaches for Lightning Strokes

In the literatures associated with lightning-induced electromagnetic environment (LIEE) in buildings, the lightning stroke was always modeled as an ideal impulse current source connected at the upper terminal of a vertical conductor which was used to modeling the lightning channel.

The waveforms of impulse current from the source in literatures were mostly chosen as 1.2/50μs (time to peak value/time to half peak value). This waveform was usually used to describe the voltage of a lightning stroke instead of the current. In fact a natural lightning flash includes several strokes [Rakov and Uman, 2003]. The waveform of discharge current in each stroke is different so that it is difficult to use uniform waveform parameters to describe lightning discharge currents. According to the IEC standard [IEC 61312-1, 1995], two typical waveforms are defined for the first stroke and the subsequent stroke.

Figure 2.19 is the defined waveform of the first stroke. The wave front is 10μs and the wave tail is 350μs. Figure 2.20 shows the waveform of the subsequent stroke. The wave front is 0.25μs and the wave tail is 100μs. For the study of lightning-induced electromagnetic environment inside buildings, 8/20μs waveform is used to replace the 10/350μs waveform for the first stroke [IEC 61312-2, 1995].

In the study of the lightning-induced electromagnetic field, mathematical models of lightning current were built. Generally, there were two types of mathematical model to be applied.

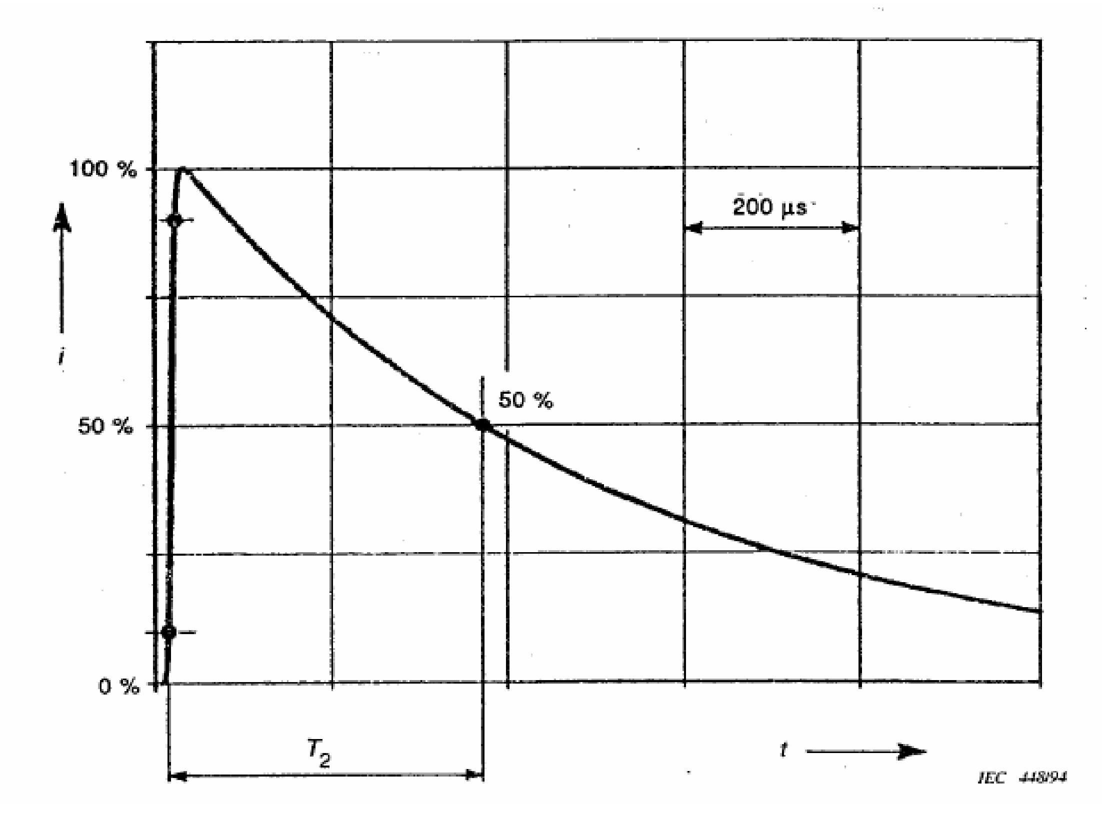

Figure 2.19 Waveform of the first stroke

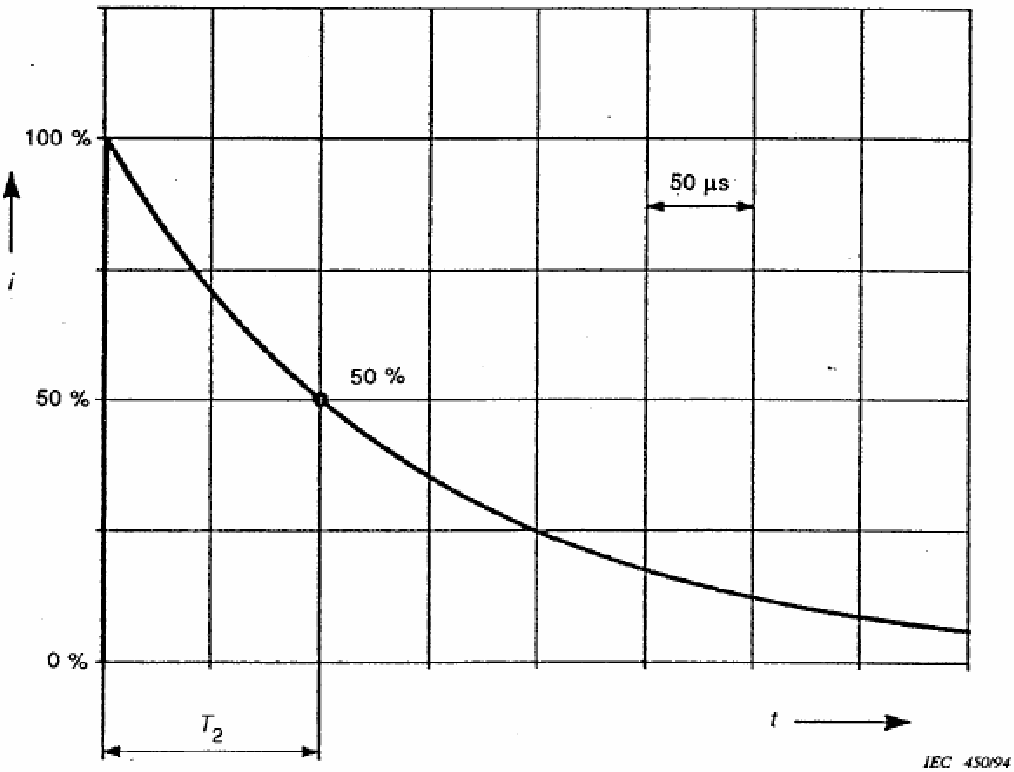

Figure 2.20 Waveform of the subsequent stroke

2.4.1.1 Double Exponential Model

In the early phase of lightning induced electromagnetic field study, the lightning discharge current is mostly modeled as a double exponential function. The function in the time domain is given by [Cristina, Amore and Orlandi, 1989-1]

$$i_s(t) = I_0(e^{-\alpha t} - e^{-\beta t}) \tag{2.10}$$

The function in the frequency domain is given by [Buccella et.al., 1992]

$$i_s(\omega) = \frac{(\beta - \alpha)}{(\alpha + j\omega)(\beta + j\omega)} I_0 \tag{2.11}$$

where I_0 is the peak value of the discharge current. $\alpha = 1/T_1$, $\beta = 1/T_2$, T_1 is defined as the wave front time. T_2 is defined as the wave tail time.

2.4.1.2 Heidler Model

In 1999, Heidler and his cooperators proposed a new model to describe the lightning discharge current [Heidler, Cvetic and Stanic, 1999]. This model is named as Heidler-type current source in EMTP to simulate lightning stroke. In this model, the shape of the lightning surge current is given described by

$$i(t) = \frac{I_m}{\eta} \frac{(t/\tau_1)^2}{1 + (t/\tau_1)^2} e^{-t/\tau} \tag{2.12}$$

where I_m is the peak value of the lightning current. τ_1 is the time taken from zero to the peak value. τ is the time from zero to the point on the tail where the current amplitude has fallen to 37% of its peak value.

This model is also adopted in the IEC Standard 61312-1 [IEC 61312-1, 1995].

2.5 Modeling Approaches for High Voltage Coaxial Cables

The studies on high voltage coaxial cables were mainly conducted in the power system. In those studies, the long and horizontal run of coaxial cables were transformer to a Bergeron model by the distributed transmission line modeling approach or a π -type circuit model by the lump transmission line modeling approach [Dommel, 1986].

For both the Bergeron model and the π -type circuit model, the inductance and capacitance per unit length should be calculated. Different methods were proposed to calculate these two parameters. Grove introduced an approach for calculating the inductance and capacitance of coaxial cables or the conductors with the coaxial structure [Grover, 1946]. This approach was adopted in EMPT subroutine [Dommel, 1986] to calculate cable. However, the formulas provided by Grove are not available for short run of coaxial cable in which the edge effect becomes obvious so that the inductance and capacitance are not even along the cable. The formulas to calculate the inductance of a coaxial cable with finite length was provided by Marcelo and this cooperator which was deriving from the Neumann's integral equation [Marcelo and Andre, 2001]. The method to calculate the capacitance of finite coaxial cable was proposed by Du and Zhou [Du and Zhou, 2005].

For the vertical run of a coaxial cable in the presence of earth, which serves a major part of the modern lightning protection system, those formulas or method presented in literature are not applicable.

2.6 Modeling Approaches for Metal Plates

The evaluation of the electromagnetic field in the presence of 3D non-ferromagnetic plate has been widely studied for many years. Since the geometry of 3D plates and configuration of incident field varies from case to case, it is hard to calculate electromagnetic field with a universal analytical method. Then all kinds of numerical methods are developed quickly, such as the finite element method (FEM), finite volume method (FVM) and boundary element method (BEM). These numerical methods can take into account all the geometrical parameters and material characteristic of the conductors. However, since FEM and FVM are based on differential formula of electromagnetic field in the concerned volume, it is not available to manage the far-field boundary conditions. BEM can handle the open field problem because it is based on the integral formulation on the conductor surface.

But all these three method require a large number of discretization in the volume or surface to solve a lot of variables. Then it requires large allocated memory and costs much computer time for obtaining accurate results.

For electromagnetic field with extremely low frequency (ELF), i.e. 50Hz power frequency, the plate is transformed to a mesh which can be considered as an electric circuit network. Then the electromagnetic field near the plate is calculated from the current distribution in the mesh. Since this method requires fewer grids than FEM and FVM and comprises fewer variables than BEM, it can provide accurate with high efficiency and limited resource. But this method is only available for uniform current density along the thickness under ELF. With increasing frequency, the current distribution along thickness becomes uneven significantly. At this time, the method is not available any more.

2.7 Study Results and Conclusions in Literatures

The characterization of LIEE inside the buildings protected by the conventional LPS and the evaluation of the induced voltage in cables has been conducted by various researchers.

In the study of Buccella and her cooperators by the field approach [Buccella et.al, 1992], they characterized LIEE inside a cubic building structure with the dimension of 24m. Three conclusions were drawn in their study. The first is that there is resonance appearing at the frequency of 150-200kHz and 5-7MHz; The second is that a stroke to the corner gives rise to the magnetic field a little greater than those resulting from a stroke to the center of the roof-grid; The third is the decreasing of electric and magnetic field when the number of the downconductors increases, which reveals the shielding effect of the LPS. Another study conducted by Cristina et al. on

LIEE inside buildings revealed that the number of downconductor was an important variable for the behavior of the electromagnetic field inside the building [Cristina et.al., 1989-2]. The spatial homogeneity of the field depends also on the frequency spectrum associated with the lightning current.

In IEC Standards 61312-2, empirical formulas are presented to evaluate the shielding effect of a wire-grid structure against the parallel-wave magnetic field from a nearby lightning stroke as Figure 2.21 shows.

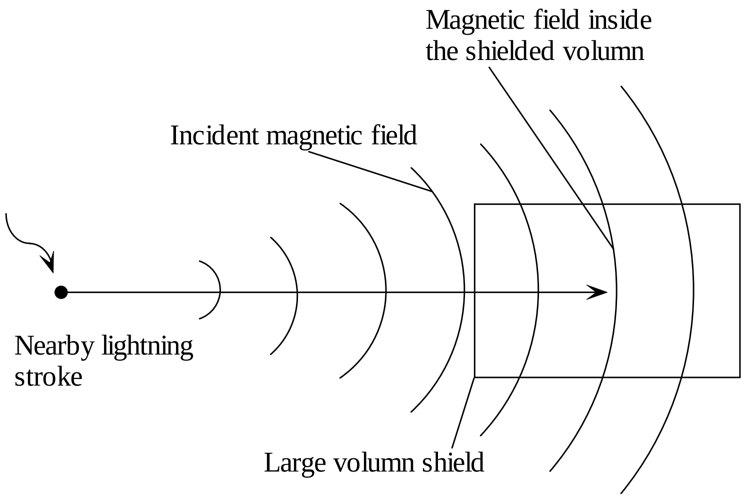

Figure 2.21 A nearby lightning stroke

As Figure 2.21 shows, a nearby lightning stroke happens near a large wire-grid structure. When the distance between the striking position and the structure is much larger than the equivalent wave length of a lightning stroke, e.g. 40 km for the first stroke and 300m for the subsequent stroke, the electromagnetic field generated from the lightning current is approximated as a parallel-plane wave inside the structure. Then the formulas to evaluate the shielding effect are presented in Table 2.1.

Table 2.1 Magnetic field attenuation of grid-like spatial shields in case of a plane wave caused by a nearby lightning stroke

Material	SF (dB)	
	25 kHz (see note 1)	1 MHz (see note 2)
Copper/Aluminum	$20\cdot\log\left(8.5/W\right)$	$20\cdot\log\left(8.5/W\right)$
Steel	$20\cdot\log\left[\left(8.5/W\right)/\sqrt{1+18\cdot10^{-6}/r^2}\right]$	$20\cdot\log\left(8.5/W\right)$
Note 1 Valid for the magnetic field of the first stroke Note 2 Valid for the magnetic field of the subsequent stroke Note 3 Permeability is 200 W is the mesh width of the grid-like structure where $W \le 5m$ r is the radius of a branch in the gridlike shielding (m)		

For the direct lightning stroke, a curve as Figure 2.22 shows was presented to reveal the magnetic field distribution inside a cubic wire-grid structure with dimension 10m. All the previous studied on LIEE characterization are very valuable because they reveal some principal characteristic of LIEE inside buildings. But since these studies are based on the scaled and simplified model of the building, their conclusions may be not enough for the high-rise buildings with special configurations. As to LIEE inside the building protected by the ESE LPS, no studies have been reported till now.

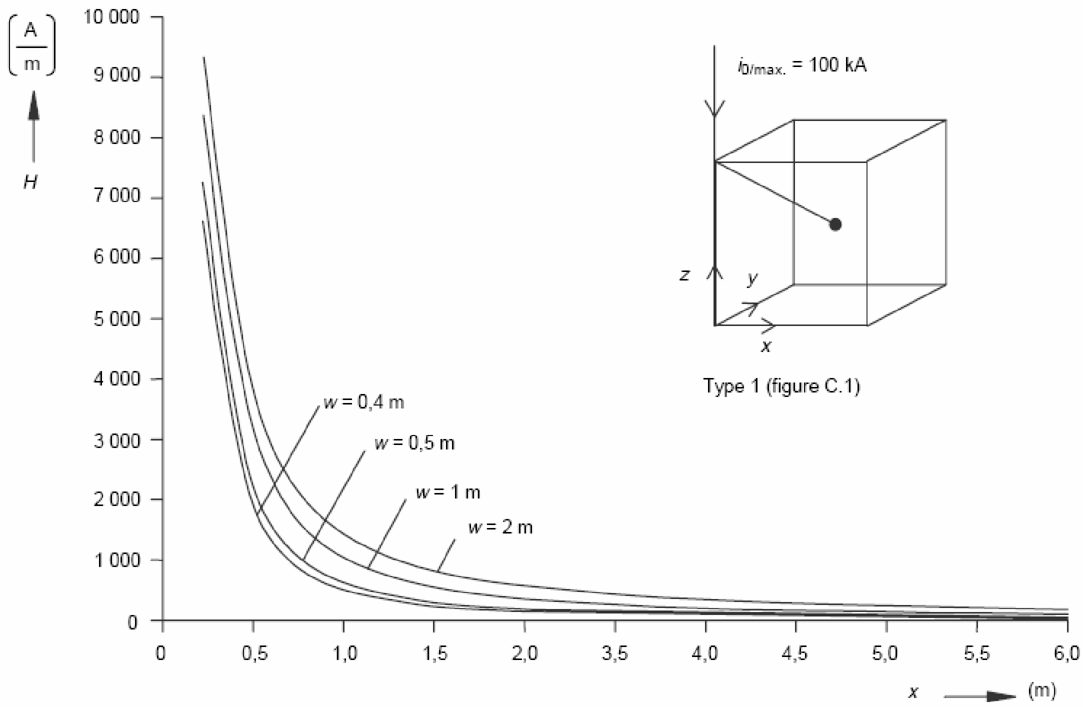

Figure 2.22 Magnetic field strength inside a wire-grid structure

As to the induced voltage in cables, Cristina and Orlandi have conducted a primary study [Cristina and Orlandi, 1992]. They applied the equivalent circuit approach to evaluate the induced voltage in coaxial cables within a simple and cubic building structure protected by the conventional LPS. They found that the voltage induced on simply-screened coaxial cables within the building may have a peak value of 1MV during a direct lightning stroke. This extremely high voltage will damage the insulation of cables and even threat the safety of the people around the cables. These conclusions are valuable to reveal the threat of LEMI on cables. But they are too generous to be applied to specified buildings whose configuration is much more complicated and larger than the model in their paper. In addition, the application of equivalent circuit approach neglects the response of cables in high frequency range. Another study conducted by Antonini et al. provided a full-wave approach, PEEC, to solve this problem [Antonini et.al., 1998]. With this approach, the resonances due to the cables' geometry, electric properties and spatial placement can be predicted.

2.8 Summary

The structure of high-rise buildings in Hong Kong can be classified into two types, the reinforcing concrete structure and the steel skeleton structure. RC bars inside the components of a reinforcing concrete structure or H-shape steel sections inside a steel skeleton structure form an internal metal structure which plays an important role in lightning protection against LIMF. Two types of LPS are used in high-rise buildings in Hong Kong, including the conventional LPS and the ESE LPS. Both of them will import serious lightning electromagnetic interference into high-rise buildings and threaten the sensitive electronic equipment.

In the previous studies on LIMF in buildings, three modeling approaches for metal building structure were developed, including the circuit approach, the field approach and the PEEC approach. Two mathematic models of lightning strokes, the double-exponential model and the Heidler model, were proposed in those studies. The modeling approaches of coaxial cable in the previous studies were mostly applied for extremely long and horizontal cables in the power transmission system. The modeling approaches for metal plates in the previous studies were not applicable for large plates at full-wave frequency. The characterization results and conclusions in literatures are not available for the high-rise building installed with the ESE LPS.

Chapter 3

Modeling Approach of Wire-grid Building Structures

3.1 Introduction

The lightning-induced impulse magnetic field (LIMF) inside buildings has been addressed for decades. Most of the research work focused on the LIMF in a building which was protected by the conventional lightning protection system (LPS) during a direct lightning stroke. Modeling of cylindrical conductors was a major issue in the studies.

In the modern lightning protection systems (e.g. the ESE LPS), coaxial cables are widely adopted as downconductors in buildings, for their favorable conducting characteristic, easy installation and safety performance [ESET, 1998]. There have been few studies on modeling coaxial cables, especial when the cable is erected vertically on the ground. In addition, the solution procedures used by other researcher were mostly conducted in the frequency domain. Since the frequency band of lightning discharge current ranges from d.c. to several million Hz, the procedure requires significantly long time to calculate the field at each discrete frequency in a wide range.

In this chapter, the equivalent circuit (EC) modeling approach for a high voltage coaxial cable as the downconductor is proposed. With the EC model of the coaxial cable and the grid-like building structure, the building protected by the ESE LPS is converted into an equivalent circuit network. Impulse current is generated within the structure during a lightning stroke. In order to obtain the current distribution in the building structure efficiently, the Electromagnetic Transient Program (EMTP) is adopted and developed in this chapter for a solution procedure in the time domain.

This chapter starts with the discussion on converting a real building structure into a wire-grid model. The EC modeling approaches for the wire-grid structure and high voltage coaxial cables used as downconductors are, respectively, proposed in Section 3.2. The formulas to calculate the equivalent circuit parameters for the wire-grid structure and coaxial cables are derived in Section 3.3. The solution procedure for calculating the current distributions by EMTP as well as the magnetic fields by Bio-savart Law are introduced in Section 3.4

3.2 Wire-grid Model of a Building Structure

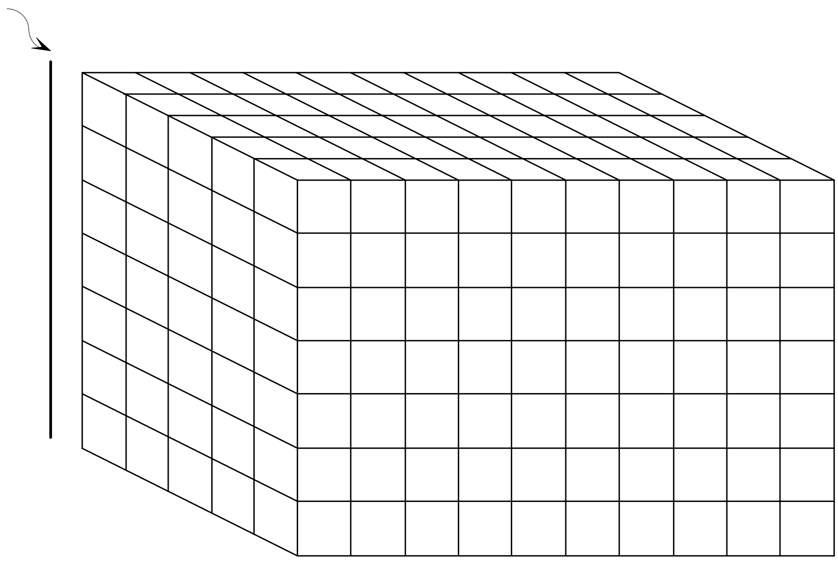

Figure 3.1 Wire-grid model of building structure installed with an isolated downconductor

As reviewed in Chapter 2, inside the internal metal structure of a reinforcing concrete building, one RC bar inside columns and beams will be firmly connected by welting. Other RC bars are bonded with each other with thin iron wires. Since most of lightning discharge current flows through the melted-connection RC bars due to their low resistance, the building structure can be simply treated with a wire-grid structure model in the study of LIMF, as Figure 3.1 shows. As to the building with the steel skeleton structure, the steel sections in the structure can be also approximated as cylindrical conductors and then the building structure can be also considered as a wire-grid structure.

3.3 The Equivalent Circuit Modeling Approach

The wire-grid model of the building structure is still a natural model which can not be used to study the magnetic field during a lightning stroke. This natural model should be transformed into a physical model which can be described by mathematical equations. Since the wire-grid model is composed by cylindrical conductors and isolated coaxial cable downconductor, the physical models of these two objects are built as follows.

3.3.1 Cylindrical Conductors

The simplified wire-grid building structure is made of a large number of cylindrical conductors. According to the study of Cristina and Orlandi [Cristina et.al., 1989-1; Cristina and Orlandi, 1992], these cylindrical conductors can be transformed to equivalent electric circuits. Thus the whole building structure is modeled as an equivalent circuit network. So this modeling approach is named as the equivalent circuit (EC) modeling approach.

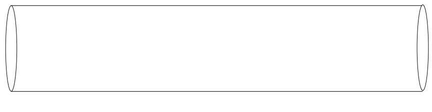

Figure 3.2 A section of cylindrical conductor

In the EC modeling approach, each cylindrical conductor inside the wire-grid structure is divided into short sections as Figure 3.2 shown. The length of each section should be much smaller than the equivalent wavelength at the maximum frequency of the lightning discharge current to be considered in order to take account of current propagation phenomena [Cristina and Orlandi, 1992].

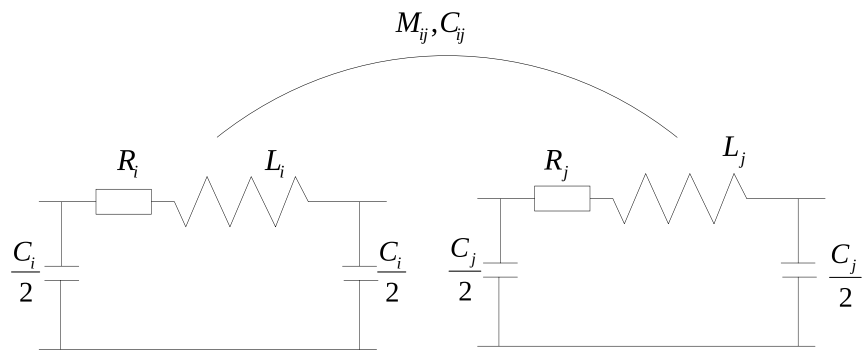

Figure 3.3 The coupled π-type circuit

Each section is modeled as a lumped π-type circuit, as shown in Figure 3.3. The π-type circuit consists of resistance R_i , and inductance L_i and capacitance C_i . In addition, there exists mutual coupling between two sections in the wire-grid structure. Such mutual coupling is represented by mutual inductance M_{ij} and mutual capacitance C_{ij} . By applying the π-type circuit to all sections, a highly-coupled lumped electrical network is used to represent the wire-grid building structure for electromagnetic analysis during a lightning stroke.

Both impedance and susceptance of the conductive branches are determined by geometric parameters and material properties of the conductors. The formulas to calculate these parameters are presented in Section 3.4.

3.3.2 High Voltage Coaxial Cable used as Downconductors

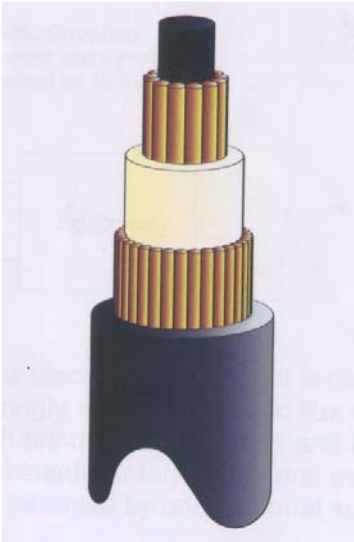

Figure 3.4 3D diagram of a HV coaxial cable

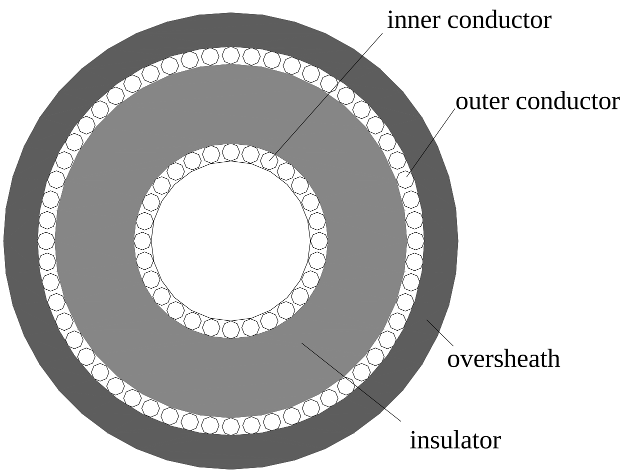

Figure 3.5 Sectional view of a HV coaxial cable

Illustrated in Figure 3.4 and Figure 3.5 are, respectively, the 3D diagram and section view of a high voltage (HV) coaxial cable used as downconductors. This downconductor consists of two concentric cylindrical shells, each of which is made by a layer of small copper wires. Unlike in power cables, these copper wires are laid straightly along the cable axis. The inner conductor (core) is dedicated to deliver the lightning current from an air terminal down to ground. The outer conductor (screening) is isolated from the core with dielectric material. It is connected to the core on the ground only.

Traditionally a coaxial cable is modeled as a transmission line in transient analysis. The transmission line model [Dommel, 1986], however, is not applicable to such concentric conductors installed in a building. It is known that electromagnetic fields in the building, which result from a lightning stroke, are not in the TEM pattern. The π-type circuit model, thus, is adopted to represent these concentric conductors.

To take account of the propagation phenomena of a lightning discharge current over a long conductor, the coaxial cable is subdivided into a number of short sections similar to the cylindrical conductor. The length of each section is usually less than one tenth of the wavelength corresponding to the maximum frequency of the lightning discharge current [Cristina and Orlandi, 1992]. Each section has two concentric conductive elements, that is, core and screening. It is modeled as an equivalent π-type circuit, as shown in Figure 3.6(a).

In addition, there is mutual impedance and admittance between four tubular conductors in every two segments as Figure 3.6(b) shows. As to the conductivity of the air, it is ignored in the π-type circuit.

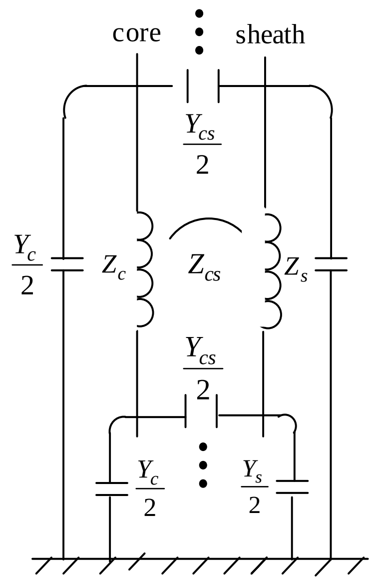

(a)

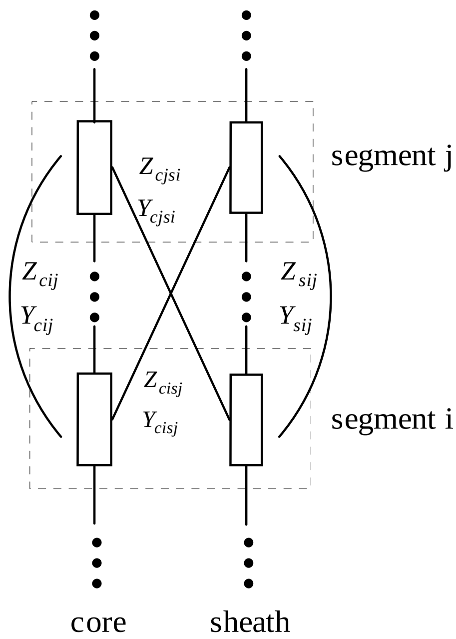

(b)

(a) single section (b) coupling between two sections

Figure 3.6 π -type circuit of vertical coaxial cable

In Figure 3.6(a), Y_c and Y_s are respectively the self admittance of the cable core and screening. Y_{cs} is the mutual admittance between these two conductors. Z_c and Z_s are respectively the self impedance of the cable core and screening. Z_{cs} is the mutual impedance between these two conductors. In Figure 3.6(b), Z_{cicj} and Y_{cicj} are respectively the mutual impedance and admittance between the cores in two sections. Z_{sisj} and Y_{sisj} are respectively the mutual impedance and admittance between the screenings in two sections. Z_{cisj} and Y_{cisj} are respectively the mutual impedance and admittance between the core of section i and the screening of section j. Z_{sicj} and Y_{sicj} are respectively the mutual impedance and admittance between the screening of section i and the core of section j.

Combining the Figure 3.6(a) and Figure 3.6(b), the relationship between the two sections can be presented by two symmetrical matrixes, $Z=[Z_{ij}]$ for impedance and $Y=[Y_{ij}]$ for admittance.

$$Z=\begin{bmatrix} Z_{ci} & Z_{cisi} & Z_{cicj} & Z_{cisj} \\ Z_{sici} & Z_{si} & Z_{sicj} & Z_{sisj} \\ Z_{cjci} & Z_{cjsi} & Z_{cj} & Z_{cjsj} \\ Z_{sjci} & Z_{sjsi} & Z_{sjcj} & Z_{sj} \end{bmatrix} \tag{3.1}$$

$$Y=\begin{bmatrix} Y_{ci} & Y_{cisi} & Y_{cicj} & Y_{cisj} \\ Y_{sici} & Y_{si} & Y_{sicj} & Y_{sisj} \\ Y_{cjci} & Y_{cjsi} & Y_{cj} & Y_{cjsj} \\ Y_{sjci} & Y_{sjsi} & Y_{sjcj} & Y_{sj} \end{bmatrix} \tag{3.2}$$

Similarly, if a coaxial cable is divided into n sections, it can be presented by $Z=[Z_{ij}]_{n\times n}$ and $Y=[Y_{ij}]_{n\times n}$.

It is worth to be mentioned that for horizontal coaxial cables, the π-type EC model is also available. A horizontal cable is divided into short sections evenly and each section is modeled by a π-type circuit. The parameters in each π-type circuit are identical because the influence of the earth imposes uniformly on the cable.

3.3.3 Coupling between an Isolated Downconductor and a Wire-grid Building Structure

The coupling between the isolated downconductor and the building structure is represented by the mutual inductance and capacitance as Figure 3.7 shows

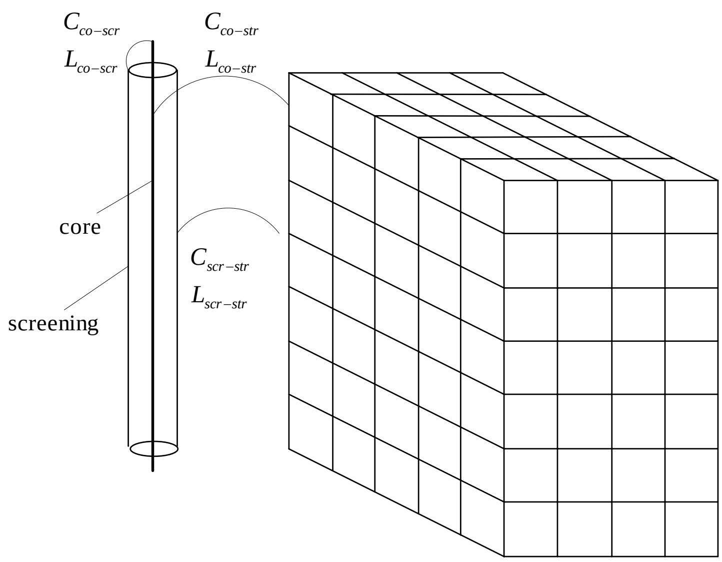

Figure 3.7 Coupling between an isolated downconductor and a wire-grid building structure

Figure 3.7 shows the coupling relationship between a coaxial cable which is used as the downconductor and the building structure. In Figure 3.7, C_{co-str} and L_{co-str} represent, respectively, the mutual capacitance and mutual inductance between the core of the coaxial cable and the building structure. $C_{scr-str}$ and $L_{scr-str}$ represent, respectively, the mutual capacitance and mutual inductance between the screening of the coaxial cable and the building structure. C_{co-scr} and L_{co-scr} represent, respectively, the mutual capacitance and mutual inductance between the core and the screening of the coaxial cable.

3.3.4 Earth Termination, Earth Influence and Lightning Stroke Model

1. Earth Termination

Both the downconductor and the building structure are earthed on the ground via dedicated earth electrodes. It has been confirmed experimentally and analytically [Liew and Darveniza, 1974; Darveniza et.al, 1979] that earth soil is ionized during a lightning stroke. The soil ionization increases the equivalent contact area of an electrode, subsequently reduces the earth resistance. According to the literature [Chisholm and Janischewskyj, 1988], earth resistance R_g of an electrode is calculated with the formula as follows

$$R_g = 0.2613\rho^{0.692}L^{-0.384}\left(\frac{I}{241\rho^{0.215}}\right)^{-0.384} \tag{3.3}$$

where I is the stroke current through the electrode (kA), and L is the length of the electrode (m). ρ is the earth resistivity ($\Omega \cdot m$) .

2. Earth Influence

In the equivalent circuit model for both the downconductor and the wire-grid building structure the influence of the earth is included by using the method of image, i.e. replacing the earth with a set of conductor images. As illustrated in Figure 3.9, the image of a conductor is located at the equivalent height of l' below the ground. Height l' is expressed as

$$l' = l + d_p \tag{3.4}$$

where l is the height of the conductor and d_p is the skin depth of the earth.

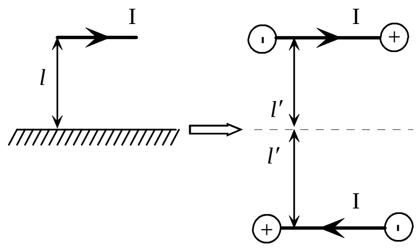

(a) Horizontal configuration

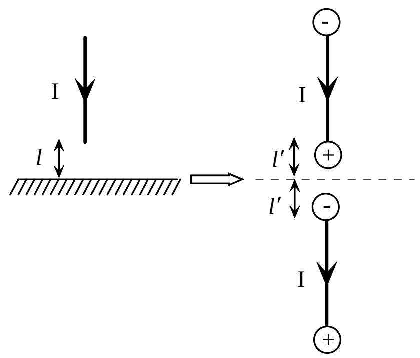

(b) Vertical configuration

Figure 3.8 Downconductor section and its image

To satisfy with the boundary conditions on the ground, the horizontal conductor and its image have to carry the equal currents with the opposite direction as Figure 3.8 (a) shows [Paul, 1994]. But the vertical conductor and its image have to carry the equal current with the same direction as shown in Figure 3.8 (b) [Jose et.al., 2001; Takahashi and Komada, 2002]. This corrects the traditional view that similar to a horizontal conductor, the current in a vertical conductor has opposite direction to the current in its image.

In the electrostatic field analysis for determining conductor capacitance the earth is treated as a perfectly conducting plane. Skin depth d_p, therefore, is identical to zero. While in calculation of conductor impedance the earth is modeled as a lossy and homogeneous medium characterized by permeability μ_0 and conductivity σ [Deri et.al., 1981]. Its skin depth is given by

$$d_p = 1\Big/\sqrt{j\omega\mu_0\sigma} \tag{3.5}$$

3. Lightning Stroke

From the studies of the lightning stroke conducted by other researchers, it is revealed that when the stepper leader propagates downward and approaches the ground surface, there is a streamer propagating upward to match the stepper leader. This phase is called the lightning preliminary phase. When the stepped leader encounters the streamer, a lightning discharge happens and an extremely large impulse current will flow through a channel into the earth. This phase is called the main discharge phase. Since the theorem of lightning discharge is very complicated, assumptions are adopted in this thesis in order to simplify the model and focus on the main aspects of the issue.

- The influence of the stepped leader and streamed is neglected in the lightning preliminary phase. Only the lightning discharge current in the main discharge phase is considered.

- The lightning discharge channel is simply considered as a straight wire carrying discharge current vertical to the ground surface. The corona phenomenon around the lightning channel is not included into consideration.

- The waveform of lightning discharge current flowing along the lightning channel is kept unchanged.

- When lightning strikes at a building structure, the influence of the building structure on the lightning discharge current is not considered.

The air terminal of the LPS is intended to intercept lightning. A lightning stroke to the building, therefore, is modeled as a unidirectional current source applied to the air terminal. According to the reference [Heidler et.al., 1999] the waveform of the lightning source current is expressed by

$$i(t) = \frac{I_m}{\eta} \frac{(t/\tau_1)^n}{1+(t/\tau_1)^n} e^{-t/\tau_2} \tag{3.6}$$

where I_m is the peak value of the lightning current. n is a current steepness factor. τ_1 and τ_2 are respectively the front and tail time constants. η is the correction factor of the current peak, and is given by

$$\eta = e^{[-(\tau_1/\tau_2)(n\tau_1/\tau_2)^{1/n}]} \tag{3.7}$$

3.4 Calculation of Circuit Parameters

3.4.1 Circuit Parameters of Cylindrical Conductors

A. Internal Impedance

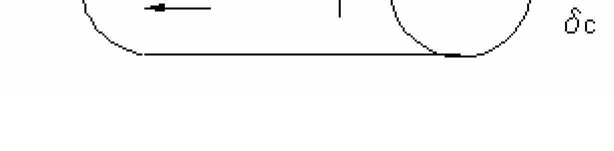

Figure 3.9 Sketch of the internal impedance definition of a cylindrical conductor

Figure 3.9 illustrate a cylindrical conductor with the radius r . The formula to calculate the internal impedance of the cylindrical conductor can be found in many classical textbooks [Woodruff, 1938; Stevenson, 1962]. It can be represented by the first kind Bessel Function, the modified first kind Bessel Function or the Kelvin Function. The formula with the Kelvin Function to calculate the internal impedance is given by [Woodruff, 1938]

$$Z_i = R_i + j\omega L_i = \frac{jmp}{2\pi r} \cdot \frac{ber(mr) + jbei(mr)}{ber'(mr) + jbei'(mr)} \tag{3.8}$$

$$m = \sqrt{\omega u / \rho} \tag{3.9}$$

$$\omega = 2\pi f \tag{3.10}$$

where f is the frequency. u is the permittivity of the conductor. ρ is the resistivity and r is the radius of the cylindrical conductor.

From (3.8), the ratio between the internal resistance and the d.c. resistance is given by

$$\frac{R_i}{R_{dc}} = \frac{mr}{2} \frac{ber(mr)bei'(mr) - bei(mr)ber'(mr)}{ber'^2(mr) + bei'^2(mr)} \tag{3.11}$$

$$R_{dc} = \frac{\rho}{\pi r^2} \tag{3.12}$$

The ratio between the internal inductance and the d.c. internal inductance is given by

$$\frac{L_i}{L_{dci}} = \frac{4}{mr} \frac{ber(mr)ber'(mr) + bei(mr)bei'(mr)}{ber'^2(mr) + bei'^2(mr)} \tag{3.13}$$

$$L_{dci} = \frac{u}{8\pi} \tag{3.14}$$

B. External Impedance

The external impedance of cylindrical conductors can be calculated with the Neuman's integrating formula [Marcelo, 2001]. It is known that the mutual impedance between two orthogonal conductors is zero. Then only the parallel conductors in the wire-grid structure are considered for calculating the mutual impedance.

The effect of the earth is taken into consideration by using the method of images. In this method, the earth is replaced with the images of these conductors distributed symmetrically with respect to a boundary. The boundary is the earth surface itself if the earth is perfectly conductive. When the earth is imperfectly conductive, the boundary is located below the earth surface by a complex distance, as illustrated in Figure 3.11. The complex distance d is equal to the penetration depth of earth, and given by

$$d = \frac{1}{\sqrt{j\omega\mu_0 / \rho}} \tag{3.15}$$

where ω is an angular frequency, μ_0 is the space permeability, and ρ is the earth resistivity. It should be mentioned that (3.15) is valid for the uniform soil model. When the multi-layer soil model is considered, the formula in literature [Deri, Tevean and Semlyen, 1981] should be adopted.

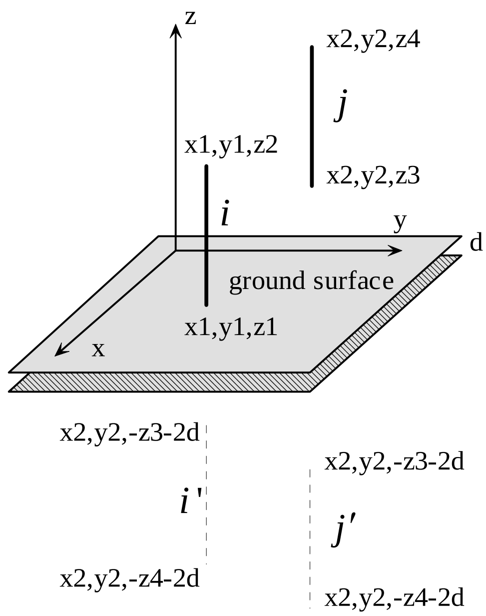

Figure 3.10 Two parallel cylindrical conductors erected vertically on the ground

Figure 3.10 shows two parallel cylindrical conductors i and j erected vertically on the ground, as well as their images i' and j' for impedance calculation. By using the Neumann's integral formula, the self-impedance of a RC conductor is obtained, as follows

$$Z_{ii} = \frac{j\omega\mu_0}{4\pi}\left[\int_{z_1}^{z_2}\int_{z_1}^{z_2}\frac{dz_j dz_i}{\sqrt{\left(z_j - z_i\right)^2 + r^2}} + \int_{z_1}^{z_2}\int_{-z_1-2d}^{-z_2-2d}\frac{dz_j dz_i}{\sqrt{\left(z_v - z_i\right)^2 + r^2}}\right] \tag{3.16}$$

where r is the radius of the cylindrical conductor .

By using the Neumann's integral formula, the mutual impendence Z_{ij} between conductor i and j can be obtained, as follows

$$Z_{ij} = \frac{j\omega\mu_0}{4\pi}\int_{z_1}^{z_2}\int_{z_4}^{z_4}\frac{dz_j dz_i}{\sqrt{\left(z_j - z_i\right)^2 + \left(x_2 - x_1\right)^2 + \left(y_2 - y_1\right)^2}}$$
$$+\frac{j\omega\mu_0}{4\pi}\int_{z_1}^{z_2}\int_{-z_4-2d}^{-z_3-2d}\frac{dz_j dz_i}{\sqrt{\left(z_v - z_i\right)^2 + \left(x_2 - x_1\right)^2 + \left(y_2 - y_1\right)^2}} \tag{3.17}$$

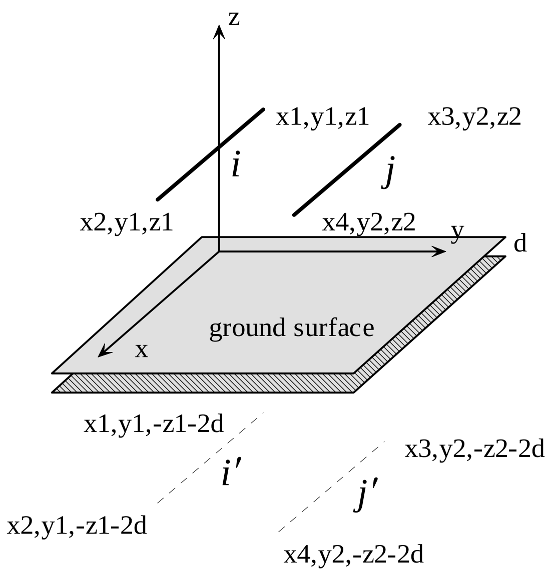

Figure 3.11 Two cylindrical conductors parallel to the ground

Figure 3.11 shows two parallel horizontal cylindrical conductor i and j parallel to the ground surface along the x coordinate axis, as well as their images i' and j'. By using the Neumann's integral formula, the self-impedance of a RC conductor is obtained as follows

$$Z_{ii} = \frac{j\omega\mu_0}{4\pi}\left[\int_{x_1}^{x_2}\int_{x_1}^{x_2}\frac{dx_j dx_i}{\sqrt{\left(x_j - x_i\right)^2 + r^2}} - \int_{x_1}^{x_2}\int_{x_1}^{x_2}\frac{dx_j dx_i}{\sqrt{\left(x_j - x_i\right)^2 + \left(-2z_1 - 2d\right)^2}}\right] \tag{3.18}$$

By using the Neumann's integral formula, the mutual impendence Z_{ij} between conductor i and j can be obtained again, as follows

$$Z_{ij} = \frac{j\omega\mu_0}{4\pi}\int_{x_1}^{x_2}\int_{x_3}^{x_4}\frac{dx_j dx_i}{\sqrt{\left(z_2 - z_1\right)^2 + \left(x_j - x_i\right)^2 + \left(y_2 - y_1\right)^2}}$$
$$-\frac{j\omega\mu_0}{4\pi}\int_{x_1}^{x_2}\int_{x_3}^{x_4}\frac{dx_j dx_i}{\sqrt{\left(-z_2 - 2d - z_1\right)^2 + \left(x_j - x_i\right)^2 + \left(y_2 - y_1\right)^2}} \qquad (3.19)$$

The impedance of the cylindrical conductors along the y coordinate axis can be calculated by (3.19) by interchanging the variables x and y in (3.19).

The explicit expressions of (3.19) are achieved by applying following integrated result

$$\begin{aligned} A &= \int_{t_1}^{t_2}\int_{t_3}^{t_4}\frac{dt_j dt_i}{\sqrt{\left(t_j - t_i\right)^2 + s^2}} \\ &= -t_{42}\ln(t_{42} + \sqrt{t_{42}{}^2 + s^2}) + \sqrt{t_{42}{}^2 + s^2} \\ &\quad + t_{32}\ln(t_{32} + \sqrt{t_{32}{}^2 + s^2}) - \sqrt{t_{32}{}^2 + s^2} \\ &\quad + t_{41}\ln(t_{41} + \sqrt{t_{41}{}^2 + s^2}) - \sqrt{t_{41}{}^2 + s^2} \\ &\quad - t_{31}\ln(t_{31} + \sqrt{t_{31}{}^2 + s^2}) + \sqrt{t_{31}{}^2 + s^2} \end{aligned} \qquad (3.20)$$

where $t_{42} = t_4 - t_2$, $t_{32} = t_3 - t_2$, $t_{41} = t_4 - t_1$, $t_{31} = t_3 - t_1$ and s is a constant.

By applying (3.20) to (3.19) with corresponding data to replace t and s, an explicit expression to calculate the impedance can be obtained.

B. Capacitance

The capacitance of the cylindrical conductors can be calculated by the average potential method [Du, 2001]. Unlike the impedance, both parallel and orthogonal bars have mutual capacitance.

The effect of the earth is taken into consideration also by using the method of images. The earth is replaced with the images of these conductors distributed symmetrically with respect to a boundary. Since charges are distributed on the conductor surface in the frequency range of the lightning, the boundary is the earth surface itself whether the earth is perfectly conductive or imperfectly conductive.

(1) Parallel Cylindrical Conductor

Thus for two cylindrical conductor in Figure 3.11 or in Figure 3.12, the distance d is always equal to zero for capacitance calculation.

Let τ_i and τ_j be the linear charge density of the cylindrical conductor i and j respectively. The self average potential coefficient of the conductor i which is generated by the charges on itself and its image i', is given by

$$P_{ii} = \frac{1}{4\pi\varepsilon_0 \left(z_2 - z_1\right)^2} \left[\int_{z_1}^{z_2} \int_{z_1}^{z_2} \frac{dz_j dz_i}{\sqrt{\left(z_j - z_i\right)^2 + r^2}} - \int_{z_1}^{z_2} \int_{-z_1}^{-z_2} \frac{dz_j dz_i}{\sqrt{\left(z_v - z_i\right)^2 + r^2}} \right] \tag{3.21}$$

The mutual average potential coefficient between conductor i and j which is generated by the charges on conductor j and its image j', is similarly given by

$$\begin{aligned} P_{ij} = {} & \frac{1}{4\pi\varepsilon_0 \left(z_2 - z_1\right)\left(z_4 - z_3\right)} \int_{z_1}^{z_2} \int_{z_4}^{z_4} \frac{dz_j dz_i}{\sqrt{\left(z_j - z_i\right)^2 + \left(x_2 - x_1\right)^2 + \left(y_2 - y_1\right)^2}} \\ & + \frac{1}{4\pi\varepsilon_0 \left(z_2 - z_1\right)\left(z_4 - z_3\right)} \int_{z_1}^{z_2} \int_{-z_4}^{-z_3} \frac{dz_j dz_i}{\sqrt{\left(z_v - z_i\right)^2 + \left(x_2 - x_1\right)^2 + \left(y_2 - y_1\right)^2}} \end{aligned} \tag{3.22}$$

For two parallel conductors arranged vertically shown in Figure 3.11, the self average potential of conductor i is given by

$$P_{ii}=\frac{1}{4\pi\varepsilon_0\left(x_2-x_1\right)^2}\left[\int_{x_1}^{x_2}\int_{x_1}^{x_2}\frac{dx_j dx_i}{\sqrt{\left(x_j-x_i\right)^2+r^2}}-\int_{x_1}^{x_2}\int_{x_1}^{x_2}\frac{dx_j dx_i}{\sqrt{\left(x_j-x_i\right)^2+\left(-2z_1-2d\right)^2}}\right]$$

(3.23)

The mutual average potential between conductor bars i and j is given by

$$\begin{aligned}P_{ij}=&\frac{1}{4\pi\varepsilon_0\left(x_2-x_1\right)\left(x_4-x_3\right)}\int_{x_1}^{x_2}\int_{x_3}^{x_4}\frac{dx_j dx_i}{\sqrt{\left(z_2-z_1\right)^2+\left(x_j-x_i\right)^2+\left(y_2-y_1\right)^2}}\\&-\frac{1}{4\pi\varepsilon_0\left(x_2-x_1\right)\left(x_4-x_3\right)}\int_{x_1}^{x_2}\int_{x_3}^{x_4}\frac{dx_j dx_i}{\sqrt{\left(-z_2-2d-z_1\right)^2+\left(x_j-x_i\right)^2+\left(y_2-y_1\right)^2}}\end{aligned} \qquad (3.24)$$

The impedance of the cylindrical conductors along the y coordinate axis can be calculated by (3.24) by interchanging the variables x and y in (3.24).

The explicit expressions of (3.24) are also achieved by applying the integrated result A into these equations.

With the calculated self and mutual potential coefficients of the cylindrical conductor in the wire-grid structure, a potential coefficient matrix P is constructed, where P=$\left[P_{ij}\right]_{n\times n}$ (n is the total number of conductors in the structure). Assuming V and Q are the potential vector and charge vector respectively, the following equation holds

Q=BV (3.25)

where B=P^{-1}. Self-capacitance c_{ii} and mutual capacitance c_{ij} are then obtained as follows

$$c_{ii} = \sum_{i=1}^{n} b_{ik} \quad i = 1, 2, \ldots, n$$
$$c_{ij} = -b_{ik} \quad i = 1, 2, \ldots, n,\ i \neq j \tag{3.26}$$

where b_{ik} and b_{ik} are the elements of matrix B. The capacitance matrix C is defined by

$$\mathrm{C} = \left[c_{ij} \right]_{n \times n} \tag{3.27}$$

(2) Orthogonal Cylindrical Conductor

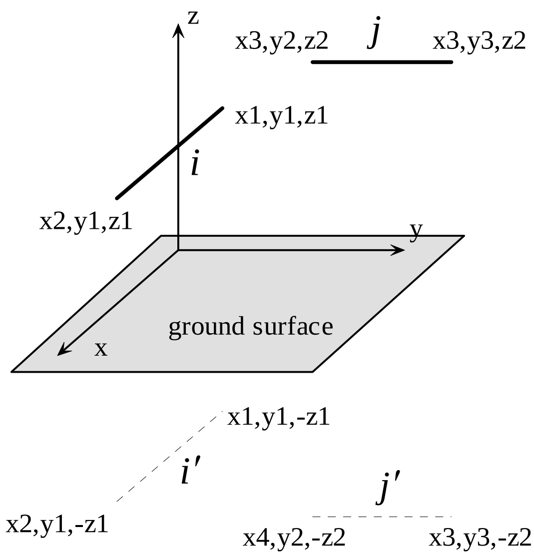

Figure 3.12 Two orthogonal cylindrical conductors in parallel with the ground

For two orthogonal cylindrical conductors shown in Figure 3.12, the mutual average potential coefficient is given by

$$\begin{aligned} P_{ij} = & \frac{1}{4\pi\varepsilon_0 (x_2 - x_1)(y_3 - y_2)} \int_{x_1}^{x_2} \int_{y_2}^{y_3} \frac{dy_j dx_i}{\sqrt{(z_2 - z_1)^2 + (x_3 - x_i)^2 + (y_j - y_1)^2}} \\ & - \frac{1}{4\pi\varepsilon_0 (x_2 - x_1)(y_3 - y_2)} \int_{x_1}^{x_2} \int_{y_2}^{y_3} \frac{dy_j dx_i}{\sqrt{(-z_2 - z_1)^2 + (x_3 - x_i)^2 + (y_j - y_1)^2}} \end{aligned} \tag{3.28}$$

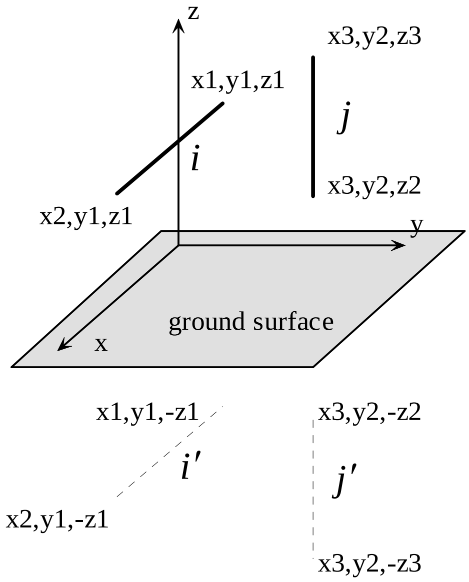

Figure 3.13 Two orthogonal cylindrical conductors unparallel to the ground

For two orthogonal cylindrical conductors shown in Figure 3.13, the mutual average potential is given by

$$
\begin{aligned}
P_{ij} = & \frac{1}{4\pi\varepsilon_0 (x_2 - x_1)(z_3 - z_2)} \int_{x_1}^{x_2} \int_{z_2}^{z_3} \frac{dz_j dx_i}{\sqrt{(z_j - z_1)^2 + (x_3 - x_i)^2 + (y_2 - y_1)^2}} \\
& - \frac{1}{4\pi\varepsilon_0 (x_2 - x_1)(z_3 - z_2)} \int_{x_1}^{x_2} \int_{-z_3}^{-z_2} \frac{dz_j dx_i}{\sqrt{(z_j - z_1)^2 + (x_3 - x_i)^2 + (y_2 - y_1)^2}}
\end{aligned}
\tag{3.29}
$$

The impedance of cylindrical conductor along the y coordinate axis can be calculated by (3.29) by interchanging the variables x and y in this equation.

The explicit expressions of (3.29) are achieved by applying following integrated result

$$
\begin{aligned}
B &= \int_{t_1}^{t_2}\int_{s_1}^{s_2} \frac{dt_i ds_j}{\sqrt{(t_i - t)^2 + (s_j - s)^2 + h^2}} \\
&= (t-t_1)\ln\frac{s_2 - s + \sqrt{(t-t_1)^2 + a^2}}{s_1 - s + \sqrt{(t-t_1)^2 + b^2}} - (t-t_2)\ln\frac{s_2 - s + \sqrt{(t-t_2)^2 + a^2}}{s_1 - s + \sqrt{(t-t_2)^2 + b^2}} \\
&+ (s_2 - s)\ln\frac{t - t_1 + \sqrt{(t-t_1)^2 + a^2}}{t - t_2 + \sqrt{(t-t_2)^2 + a^2}} - (s_1 - s)\ln\frac{t - t_1 + \sqrt{(t-t_1)^2 + b^2}}{t - t_2 + \sqrt{(t-t_2)^2 + b^2}} \\
&+ 2\sqrt{a^2 - (s_2 - s)^2}\, arctg\left[\frac{(t-t_1)\sqrt{a^2 - (s_2 - s)^2}}{\left(a + (s_2 - s)\right)\left(a + \sqrt{a^2 + (t-t_1)^2}\right)}\right] \\
&- 2\sqrt{a^2 - (s_2 - s)^2}\, arctg\left[\frac{(t-t_2)\sqrt{a^2 - (s_2 - s)^2}}{\left(a + (s_2 - s)\right)\left(a + \sqrt{a^2 + (t-t_2)^2}\right)}\right] \\
&- 2\sqrt{b^2 - (s_1 - s)^2}\, arctg\left[\frac{(t-t_1)\sqrt{b^2 - (s_1 - s)^2}}{\left(b + (s_1 - s)\right)\left(b + \sqrt{b^2 + (t-t_1)^2}\right)}\right] \\
&+ 2\sqrt{b^2 - (s_1 - s)^2}\, arctg\left[\frac{(t-t_2)\sqrt{b^2 - (t_2 - t)^2}}{\left(b + (s_1 - s)\right)\left(b + \sqrt{b^2 + (t-t_2)^2}\right)}\right]
\end{aligned}
\tag{3.30}
$$

where $a = \sqrt{(s_2 - s)^2 + h^2}$ and $b = \sqrt{(s_1 - s)^2 + h^2}$. h is a constant.

By applying (3.30) to (3.29) with corresponding data to replace t and s, an explicit expression to calculate the impedance can be obtained.

3.4.2 Circuit Parameters of High Voltage Coaxial Cables

As seen in Figure 3.4, an isolated downconductor consists of two concentric cylindrical conductors isolated by dielectric material. Such a downconductor is modeled as two thin conductive cylindrical shells separated by a layer of dielectric material characterized by the permittivity of ε_1. Figure 3.14 illustrates a section of the downconductor running vertically above the ground and it image. It contains two concentric conductive cylindrical elements, which are labeled by 1 and 2. These elements have the radii of R_a and R_b, respectively, and have the axial length of $L_n = l_{n+1} - l_n$. As the downconductor is rotationally symmetric with respect to its axis, both surface charges and axial currents are uniformly distributed along the circumferential direction.

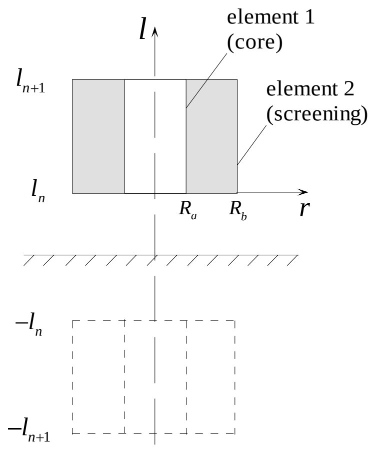

Figure 3.14 Cylindrical element of the downconductor and its image

A. Impedance

In calculating mutual impedance, the axial current in an element is treated as a surface current. The Neumann's surface integral formula [Bueno, 2001], then, is applied. For the case of the elements situated above the ground, mutual impedance $Z_{im,jn}$ between element *i* (*i* =1 or 2) in section *m* and element *j* (*j* =1 or 2) in section *n* becomes

$$Z_{im,jn} = \frac{j\omega\mu_0}{16\pi^3}\left[S_{im,jn} + S_{im,j'n'}\right] \tag{3.31}$$

where $S_{im,jn}$ and $S_{im,j'n'}$ are the coupling coefficients associated with element *i* and its image, respectively. Both $S_{im,jn}$ and $S_{im,j'n'}$ are expressed by

$$S_{im,jn} = 2\pi \int_0^{2\pi} \left[d_{m,n+1} H\left(\frac{d_{m,n+1}}{A}\right) + d_{m+1,n} H\left(\frac{d_{m+1,n}}{A}\right) - d_{m,n} H\left(\frac{d_{m,n}}{A}\right) - d_{m+1,n+1} H\left(\frac{d_{m+1,n+1}}{A}\right) \right] d\theta \tag{3.32}$$

$$S_{im,j'n'} = 2\pi \int_0^{2\pi} \left[d'_{m,n+1} H\left(\frac{d'_{m,n+1}}{A}\right) + d'_{m+1,n} H\left(\frac{d'_{m+1,n}}{A}\right) - d'_{m,n} H\left(\frac{d'_{m,n}}{A}\right) - d'_{m+1,n+1} H\left(\frac{d'_{m+1,n+1}}{A}\right) \right] d\theta \tag{3.33}$$

and

$$H(x) = \sinh^{-1}(x) + \sqrt{1+x^2} \tag{3.34}$$

where $A^2 = R_i^2 + R_j^2 - 2R_i R_j \cos\theta$. Axial distances $d_{m,n} = \left|l_m - l_n\right|$ and $d'_{m,n} = \left|l_m + l_n\right|$.

Self impedance of a cylindrical element is comprised of internal impedance and external impedance. The external impedance can be calculated with (3.33), in which both two elements coincide in space. The internal impedance of the element, however, is determined by the current distribution over its cross section area. For a cylindrical element with inner radius R_i and outer radius R_o, its internal impedance $Z_{in,in,i}$ was derived in [Xu, 2004], and expressed by

$$Z_{in,in,\mathrm{i}} = -\frac{j\omega\mu}{2\pi R_i} \cdot \frac{I_0(X_o)K_1(X_i) + I_1(X_i)K_0(X_o)}{I_1(X_i)K_1(X_o) - I_1(X_o)K_1(X_i)} \cdot L_n \tag{3.35}$$

where $I_n(X)$ and $K_n(X)$ are the first and second modified Bessel functions of order n with argument $X = R\sqrt{j\omega\mu\sigma}$, respectively. Both μ and σ are the permeability and conductivity of the element.

B. Susceptance

An electrostatic field analysis is performed to determine susceptance of an isolated downconductor. Because of the dielectric material bound charges appear on its dielectric surfaces when the downconductor is energized. Each section of the downconductor, therefore, is modeled as four charge-carrying concentric cylindrical elements with zero thickness. These elements include the conductive surfaces S_1 and S_2 of the conductors at $r = R_a$ and R_b , the dielectric surfaces S_3 and S_4 of the insulator at $r = R_a$ and R_b as well, as illustrated in Figure 3.15.

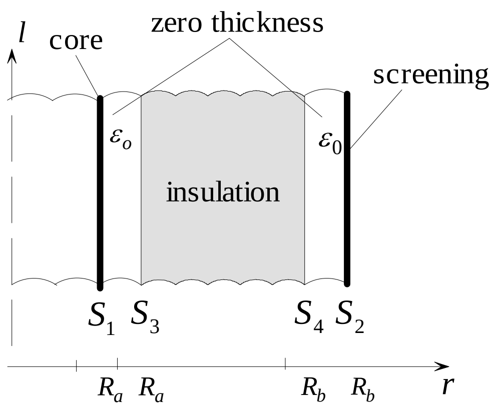

Figure 3.15 Boundary conditions on dielectric-space interfaces

Assume that the charge density is constant over an element. The potential at a point can be expressed in terms of charge density using a free-space potential formula. The average potential on a conductive element in a system of N sections, therefore, is given by

$$\bar{V}_{1,m} = \frac{1}{16\pi^3\varepsilon_0}\sum_{j=1}^{4}\sum_{n=1}^{N}\frac{1}{L_m L_n}\left(S_{1m,jn} - S_{1m,j'n'}\right)Q_{jn} \quad \text{on surface } S_1 \tag{3.36}$$

$$\bar{V}_{2,m} = \frac{1}{16\pi^3\varepsilon_0}\sum_{j=1}^{4}\sum_{n=1}^{N}\frac{1}{L_m L_n}\left(S_{2m,jn} - S_{2m,j'n'}\right)Q_{jn} \quad \text{on surface } S_2 \tag{3.37}$$

where $\bar{V}_{i,m}$ is the average potential on an inner ($i=1$) or outer ($i=2$)conductive element in section m ($m = 1 \cdots N$). Q_{jn} is the free charge (j =1 or 2), or the bound charge (j = 3 or 4). Both $S_{im,jn}$ and $S_{im,j'n'}$ are given in (3.32) and (3.33).

The boundary condition of electric field on a dielectric surface is applied to eliminate those bound charges in [Rao, 1984]. The electric field in the radial direction (r) is given by $-\partial V/\partial r$, in which V is the potential at the point of interest. The average radial field components on both positive and negative sides of element i (i = 3 or 4) are obtained by integrating over its surface. The equations, which arise from the boundary condition on elements i= 3 and i = 4 in section m, are given by

$$\begin{aligned} 0 = &\frac{1}{4\pi\varepsilon_0}\sum_{j=1}^{4}\sum_{n=1}^{N}\left(T_{im,jn} - T_{im,j'n'}\right)\frac{Q_{jn}}{L_n} \\ &+ \frac{Q_{1m}}{2\varepsilon_0 L_m} - \left(\frac{\varepsilon_0+\varepsilon_1}{\varepsilon_0-\varepsilon_1}\right)\frac{Q_{3m}}{2\varepsilon_0 L_m} \end{aligned} \quad \text{on surface } S_3 \tag{3.38}$$

$$\begin{aligned} 0 = &\frac{1}{4\pi\varepsilon_0}\sum_{j=1}^{4}\sum_{n=1}^{N}\left(T_{im,jn} - T_{im,j'n'}\right)\frac{Q_{jn}}{L_n} \\ &- \frac{Q_{2m}}{2\varepsilon_0 L_m} + \left(\frac{\varepsilon_0+\varepsilon_1}{\varepsilon_0-\varepsilon_1}\right)\frac{Q_{4m}}{2\varepsilon_0 L_m} \end{aligned} \quad \text{on surface } S_4 \tag{3.39}$$

where $T_{im,jn}$ and $T_{im,j'n'}$ are the coupling coefficients of the electric field associated with element i in section n and its image. Both $T_{im,jn}$ and $T_{im,j'n'}$ are given by

$$T_{im,jn} = \int_0^{2\pi} \frac{R_i - R_j \cos\theta}{A} \left[H'\left(\frac{d_{m,n+1}}{A}\right) + H'\left(\frac{d_{m+1,n}}{A}\right) - H'\left(\frac{d_{m,n}}{A}\right) - H'\left(\frac{d_{m+1,n+1}}{A}\right) \right] d\theta$$

(3.40)

$$T_{im,j'n'} = \int_0^{2\pi} \frac{R_i - R_j \cos\theta}{A} \left[H'\left(\frac{d'_{m+1,n}}{A}\right) + H'\left(\frac{d'_{m,n+1}}{A}\right) - H'\left(\frac{d'_{m,n}}{A}\right) - H'\left(\frac{d'_{m+1,n+1}}{A}\right) \right] d\theta$$

(3.41)

and

$$H'(x) = \sqrt{x^2 + 1} \tag{3.42}$$

Parameters A, d_{ij} and d'_{ij} in (3.40-3.42) are defined previously in (3.32-3.34). The second or third item of (3.39) and (3.40) results from a singular integral in which both the source and observation elements coincide in space.

Similar to the calculation of cylindrical conductor capacitance, a matrix equation for both free and bound charges is assembled from (3.36-3.37) and (3.38-3.39), as follows

$$\mathbf{V} = \mathbf{PQ} \tag{3.43}$$

or in expanded form

$$\begin{bmatrix} \mathbf{V}_1 \\ \mathbf{V}_2 \\ \mathbf{0} \\ \mathbf{0} \end{bmatrix} = \begin{bmatrix} \mathbf{P}_{11} & \mathbf{P}_{12} & \mathbf{P}_{13} & \mathbf{P}_{14} \\ \mathbf{P}_{21} & \mathbf{P}_{22} & \mathbf{P}_{23} & \mathbf{P}_{24} \\ \mathbf{P}_{31} & \mathbf{P}_{32} & \mathbf{P}_{33} & \mathbf{P}_{34} \\ \mathbf{P}_{41} & \mathbf{P}_{42} & \mathbf{P}_{43} & \mathbf{P}_{44} \end{bmatrix} \begin{bmatrix} \mathbf{Q}_1 \\ \mathbf{Q}_2 \\ \mathbf{Q}_3 \\ \mathbf{Q}_4 \end{bmatrix} \tag{3.44}$$

where both $\mathbf{V_n}$ and $\mathbf{Q_n}$ are the potential and charge vectors on the elements in section *n*. Sub-matrix $\mathbf{P_{nm}}$ is formulated using the formulas given in (3.36-3.37) and

(3.38-3.39). Equation (3.43) may be expanded if other conductors are presented in the vicinity of the downconductor, such as the wire-grid structure of a building.

Inverting (3.44) as well as collecting the equations for the free charge vectors yield

$$\begin{bmatrix} \mathbf{Q_1} \\ \mathbf{Q_2} \end{bmatrix} = \begin{bmatrix} \mathbf{K_{11}} & \mathbf{K_{12}} \\ \mathbf{K_{21}} & \mathbf{K_{22}} \end{bmatrix} \begin{bmatrix} \mathbf{V_1} \\ \mathbf{V_2} \end{bmatrix} \tag{3.45}$$

where $\mathbf{K_{ij}}$ is an $N \times N$ sub-matrix of $\mathbf{P}^{-1}$. Susceptance matrix $\mathbf{Y}$ for N sections or 2N elements of the downconductor, then, is expressed by

$$\mathbf{Y} = \mathbf{j\omega} \begin{bmatrix} \mathbf{K_{11}} & \mathbf{K_{12}} \\ \mathbf{K_{21}} & \mathbf{K_{22}} \end{bmatrix} \tag{3.46}$$

3.5 Solution Procedure

In most studies on modeling building structure under a lightning stroke, the calculation of current distribution in a building structure was conducted in the frequency domain [Buccella et.al., 1992]. With this solution procedure, the transient lightning discharge current in the time domain is transformed to discrete components at discrete frequencies by the Fourier transform technique. Then the nodal equations and loop equations are built for each discrete frequency according to Kirchhoff's Law. By solving these equations, the nodal voltages and branch currents can be obtained at each discrete frequency. Finally, the transient currents within the building structure are obtained by the inverse Fourier transform technique. This solution procedure takes into account of the frequency-dependent characteristic of circuit parameters. Since the frequency band of a lightning discharge current is from d.c. to several million Hz, the complete solution procedure will cost very long time. In order to improve the solution efficiency, a solution procedure running by the

Electromagnetic Transient Program (EMTP) in the time domain is proposed in this thesis.

EMTP is a universal program for numerical simulation of transient phenomena of electromagnetic as well as electromechanical nature. It can handle lumped circuit problems by π -circuit model professionally. However, as EMTP was originally designed for transmission line problems, the parameters of only a few mutual coupling branches can be calculated (less than 10 branches). So people usually think it is hard or impossible for EMTP to handle a network with a large numbers of coupled branches [Li and Zheng, 1998]. In fact, EMTP can handle a system including numerous coupled branches by adopting some modifications.

3.5.1 The Formation of EMTP Cards

In EMTP, the electrical circuit network of building structure is represented by 'cards' in an input file. A format of these cards in a general input file is shown in Figure 3.16. In this input file, there are different types of cards, including /BRANCH cards, /SWITCH cards, /SOURCE cards and /OUTPUT cards. /BRANCH cards are used to list the parameters of π -type circuits such the resistance matrix [R], inductance matrix [L[and the capacitance matrix [C] ./SWITCH cards are used to output the current value in each branch. /SOURCE cards are used to locate the current source. The meaning of those parameters in the input file in Figure 3.16 can be found in the rulebook of EMTP [Dommel, 1986].

```
BEGIN NEW DATA CASE
C ----------------------------------------------
C Generated by Zhou QB at 20-May-2004 12:46:11
C ----------------------------------------------
C  dT  >< Tmax >< Xopt >< Copt >
1.0e-0080.000020
      50       1       1       1       1       0       0       1       0
C        1         2         3         4         5         6         7         8
C 345678901234567890123456789012345678901234567890123456789012345678901234567890
/BRANCH
C < n 1>< n 2><ref1><ref2>< R  >< L  >< C  >
C < n 1>< n 2><ref1><ref2>< R  >< A  >< B  ><Leng><><>0
$UNITS,      0,      0
$VINTAGE, 1
$UNITS,      0,   0
$LISTOFF
$INSERT, data.dat
$VINTAGE, -1,
$UNITS, -1., -1., { Restore values that existed b4 preceding $UNITS
$UNITS, -1, -1
/SWITCH
C < n 1>< n 2>< Tclose ><Top/Tde ><   Ie   ><Vf/CLOP ><  type  >
     .
     .
  XX0005XX0001                                        MEASURING              1
     .
     .
$LISTON
/SOURCE
C < n 1><>< Ampl.  >< Freq.  ><Phase/T0><   A1   ><   T1   >< TSTART >< TSTOP  >
15XX00012-11.000e+0052.000e-0072.600e-007       2.                            1.
/INITIAL
/OUTPUT
BLANK BRANCH
BLANK SWITCH
BLANK SOURCE
BLANK INITIAL
BLANK OUTPUT
BEGIN NEW DATA CASE
BLANK
```

Figure 3.16 Format of cards in the EMTP Input file

```
1XX0031XX0022            2.4673165e-002  2.2787326e-003  3.0632922e-005
2XX0033XX0023            0.0000000e+000  3.3023967e-004 -1.2837748e-007
                         2.4673165e-002  2.2787326e-003  2.6881710e-005
3XX0035XX0024            0.0000000e+000  1.8686377e-004 -1.7417986e-008
                         0.0000000e+000  3.3023967e-004 -1.8313553e-007
                         2.4673165e-002  2.2787326e-003  2.6642528e-005
4XX0039XX0025            0.0000000e+000  3.3023967e-004 -1.2837759e-007
                         0.0000000e+000  2.5143060e-004 -8.1846708e-008
                         0.0000000e+000  1.6910099e-004 -7.7583498e-009
                         2.4673165e-002  2.2787326e-003  2.6881710e-005
5XX0041XX0026            0.0000000e+000  2.5143060e-004 -6.5205281e-008
                         0.0000000e+000  3.3023967e-004 -1.5530221e-007
                         0.0000000e+000  2.5143060e-004 -8.2629622e-008
                         0.0000000e+000  3.3023967e-004 -1.5530197e-007
                         2.4673165e-002  2.2787326e-003  2.7078066e-005
```

Figure 3.17 Example of branch cards inside data.dat

In the modern version of EMTP, matrices [R], [L] and [C] of a horizontal transmission line network in a π-circuit model are calculated by using the LCC subroutine in EMTP. The subroutine, however, cannot computer the π-circuit parameters of a three-dimensional grid-like structure including lots of vertical and horizontal branches. Therefore, the parameter matrices need to be calculated separately with the methods given in Section 3.3, and inserted into the EMTP data file 'data.dat' in a defined format. Figure 3.17 shows the format of a data file for five branches. The number in the first list is the branch number. Following characters like 'XX0031' is the code of a node in the circuit network. Then three lists of data are respectively the low triangle matrix of [R], [L] and [C] in the unit ohm, mH and uF.

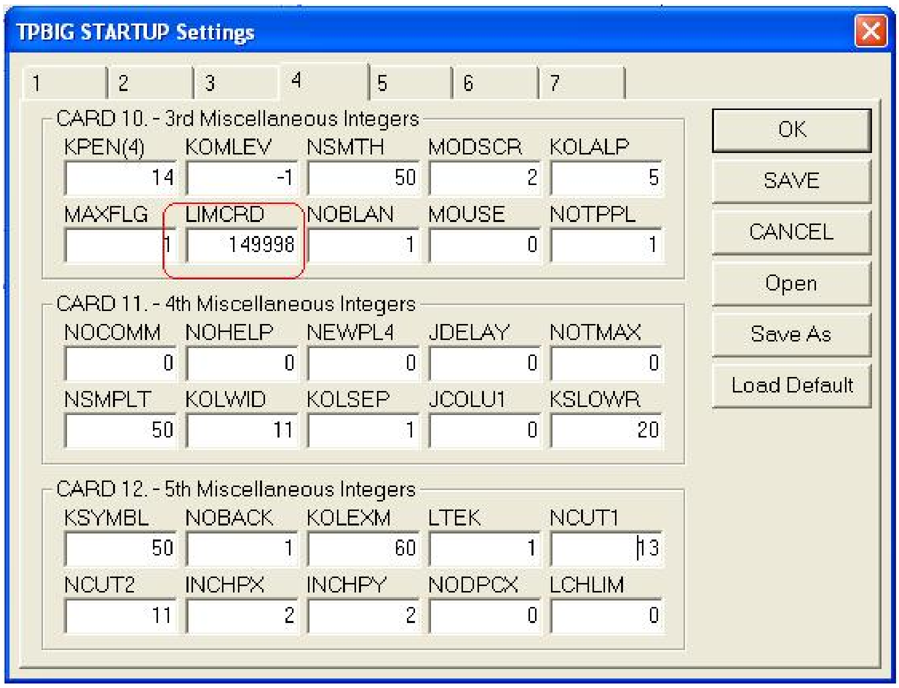

Figure 3.18 Setting parameters inside STARTUP file

For a metal structure with N coupled branches, the number of $BRANCH cards will be N× (N+1)/2. When the branch number is great, the number of the cards inside the EMTP input file will exceed the upper limit of the card number specified by the parameter LIMCRD in the STARTUP file shown in Figure 3.18 (e.g., 149998 in the current version of EMTP). The way to raise the upper limit of card number is to save the $BRANCH cards in a separate data file, and to link the data file by inserting a $INSERT card in the EMTP input file. The total number of the cards in the input file will not exceed the maximum limit as the cards in the separate data file are not counted.

3.5.2 The Expansion of EMTP Calculation Capability

Before executing EMTP machine-related constants inside Figure 3.19 need to be defined. These constants are used to allocate memory in a computer for saving different components of the electrical network, such as LBUS for the bus number, LBRNCH for the branch number, LSWTCH for the switch number and so on. The executable EMTP file ‘tpbig.exe’, which is compiled from the default file LISTSIZE.BPA, can only handle a multiphase system with less than 400-coupled branches. In reality, the metal structure of a building may consists of thousands of coupled branches. So it is necessary to generate a new executable file ‘tpbig.exe’ by recompiling the EMTP files with the appropriate values of LBUS, LBRNCH, LSWTCH and others in LISTSIZE.BIG.

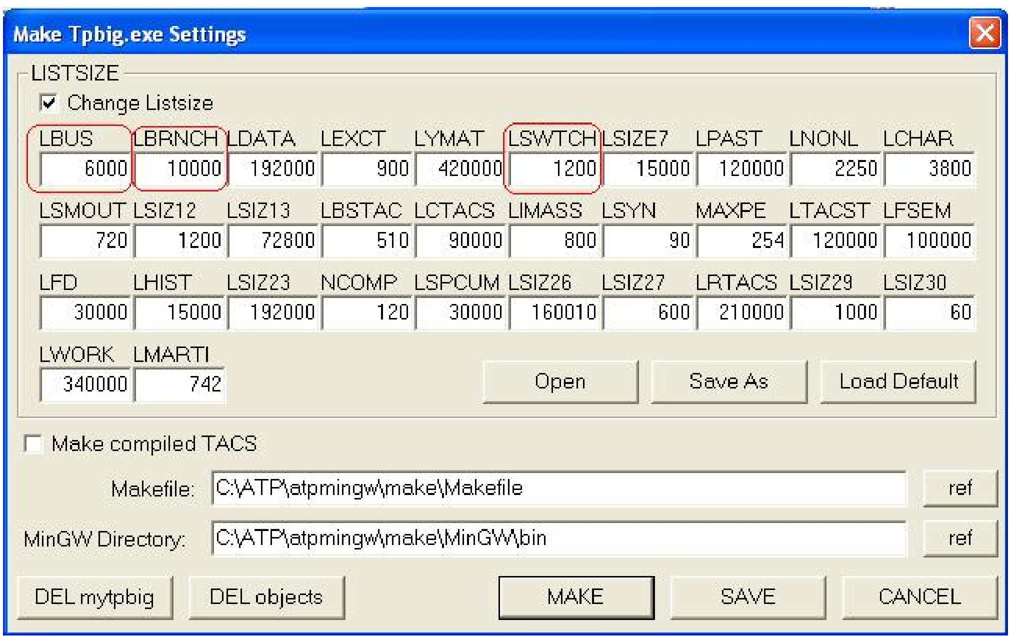

Figure 3.19 Setting of the LISTSIZE file

At present, an integrated EMTP package including ATP Launcher is available on EMTP-ATP user group websites. It allows users to increase the calculation capability of the executable file ‘tpbig.exe’. This, however, does not mean the capability of EMTP is infinite. Actually it is restricted by the computing power of the computer, especially its memory.

3.5.3 Calculation in the Frequency Domain and the Time Domain

In general, the branch impedance is frequency-dependent as discussed in Section 1.3. The time-domain solution provided by EMTP may not be accurate, as EMTP cannot transfer the impedance parameters at different frequencies into one input files. It is, therefore, necessary to obtain the frequency spectrum of the lightning current source by using the Fourier transform, and to find the solution in the frequency domain with EMTP. The time-domain currents in conducting branches are then obtained by applying the inverse Fourier transform. It is noted that this method requires significant computing power as it is necessary to calculate impedance parameters and run ‘tpbig.exe’ at each discrete frequency in a large range.

Since amplitudes of the frequency spectrum of the lightning current source are far from negligible for the frequencies less than 7 to 8 MHz [Cristina and Orlandi, 1992], the structure inductance plays a dominant role in determining the branch currents. If the earth resistivity is small, the inductance does not vary significantly in the frequency range of interest. Thus the problem can be tackled in the time domain by a single run of ‘tpbig.exe’. The impedance parameters at the significant frequency $1/4t_f$ (t_f is the time taken from zero to the peak value) is adopted, and included in the input file. When the resonance phenomena in the network become significant, the impedance parameters at the resonant frequency should be adopted as these parameters, especially the resistances are critical in determining the resonance amplitudes.

3.5.4 Calculation of Magnetic Field

With the calculated current in each conductors of the wire-grid structure by EMTP, the magnetic fields inside the building structure can be evaluated directly by the Bio-savart Law.

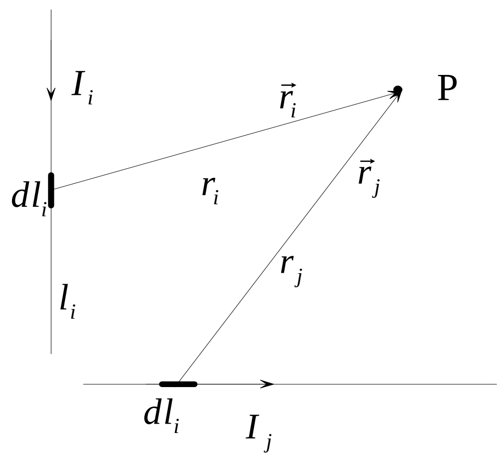

Figure 3.20 Superposition of magnetic field generated from two straight conductors

As seen in Figure 3.20, two straight conductors carry current I_i and I_j, respectively. The formula for computing the magnetic field at the observation point P generated by the current I_i is given by

$$\vec{B}_i = \frac{\mu_0}{4\pi}\int_{l_i} \frac{\vec{I}_i dl \times \vec{r}_i}{r_i^2} \tag{3.47}$$

where l_i is the integral route along the conductor. $\vec{r}_i$ is the unit vector from infinitesimal section dl_i to the observation point P and r_i is the distance between them.

Similarly the magnetic field at the same observation point P generate by current I_j is given by (3.47) by replacing the subscript i with j. Then the totally magnetic field at the observation point P is the sum of two vector magnetic fields. For a building structure with a large number of conductors, above superposition procedure can be applied for the magnetic field generated from each conductor.

3.6 Summary

In this chapter, the equivalent circuit (EC) modeling approach was proposed for the building equipped with an isolated downconductor. With this modeling approach, a wire-grid building structure was transformed into an equivalent circuit network. The nodal voltage and branch current in the network can be described by Kirchhoff's voltage equations and current equations. The formulas for determining the equivalent circuit parameters including impedance and susceptance were derived for both cylindrical conductors and coaxial cables. In order to increase the solution efficiency, a powerful program EMTP was adopted and extended to handle the solution of current distribution in the building structure. Consequently, the magnetic fields in the structure can be obtained from the current distribution by the Bio-savart Law.

Chapter 4

Characterization of Magnetic Field Distribution inside a Wire-grid Building Structure

4.1 Introduction

Chapter 3 provides the equivalent circuit (EC) modeling approach for a building protected with an early streamer emission (ESE) lightning protection system (LPS). With this modeling approach, the wire-grid building structure is transformed to an equivalent circuit network consisting of a large number of π-type circuits. The current distribution in the network is evaluated by solving the Kirchhoff's equations through the Electromagnetic Transient Program (EMTP) in the time domain. Given by the current distribution, the lightning-induced impulse magnetic field (LIMF) inside a wire-grid structure is calculated by the Bio-savart Law.

In the past decades the characterization of LIMF inside the buildings protected by a conventional LPS has been carried out extensively [Geri, 1991; Mattos, 1992; Orlandi, Mazzetti and Flisowsk, 1998]. It was found that intense impulse magnetic fields appear in the adjacent area under the lightning stroke position. However, LIMF associated with the isolated downconductors has not been addressed significantly.

This chapter presents an analysis of LIMF inside a modern laboratory building by the EC modeling approach proposed in Chapter 3. The building of concern is protected by the ESE LPS with an isolated downconductor. In this chapter a system model for a metal structure of a full-scale building is set up firstly. With this model LIMF distribution in the building installed with ESE LPS are characterized, and compared with LIMF generated by a single downconductor without the building structure. The mitigation measures of the impulse magnetic field are addressed. Finally, recommendations for protecting critical equipment against LIMF are provided.

4.2 Wird-grid Model of the Laboratory Buliding

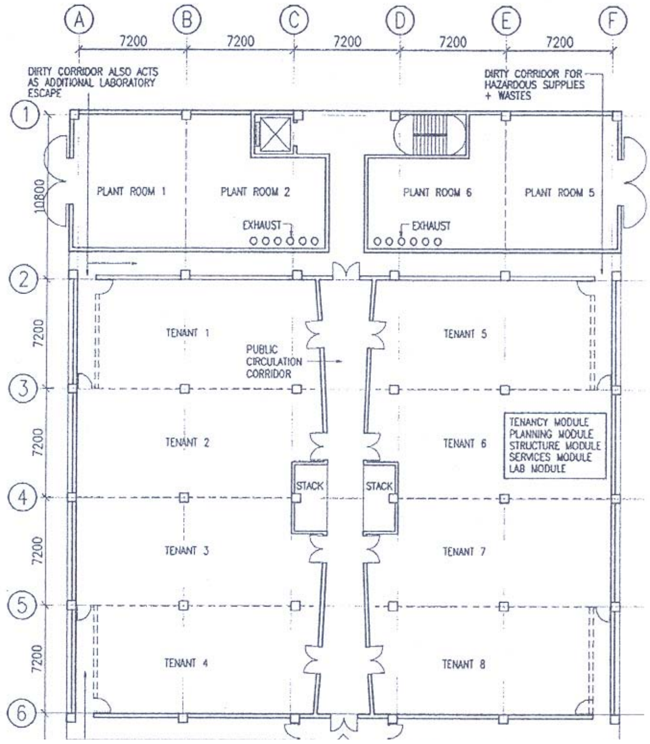

Figure 4.1 Floor plane of the laboratory building

The building to be studied in this chapter is a laboratory building under construction. The project is commissioned by the local government to develop an effective working environment for technology-based enterprises to carry out research and development works. This laboratory building includes two symmetrical parts. The left part is for biotechnology laboratories and the right part is for electronic and precision laboratories. For protecting sensitive electronic equipment installed inside the building, it is required that the magnetic field should be kept below 1mT in some critical areas. Since the two parts are identical in their structure, the floor plane of only one part is illustrated in Figure 4.1.

The geometric information of the laboratory building is given in Figure 4.1. It is 72m long, and 36m wide. There are 11×6 reinforcing concrete columns equally spaced with the separation distance of 7.2m. These columns are numbered by numerical number 1, 2, 3,… along a list and English letter A, B, C, … along a row.

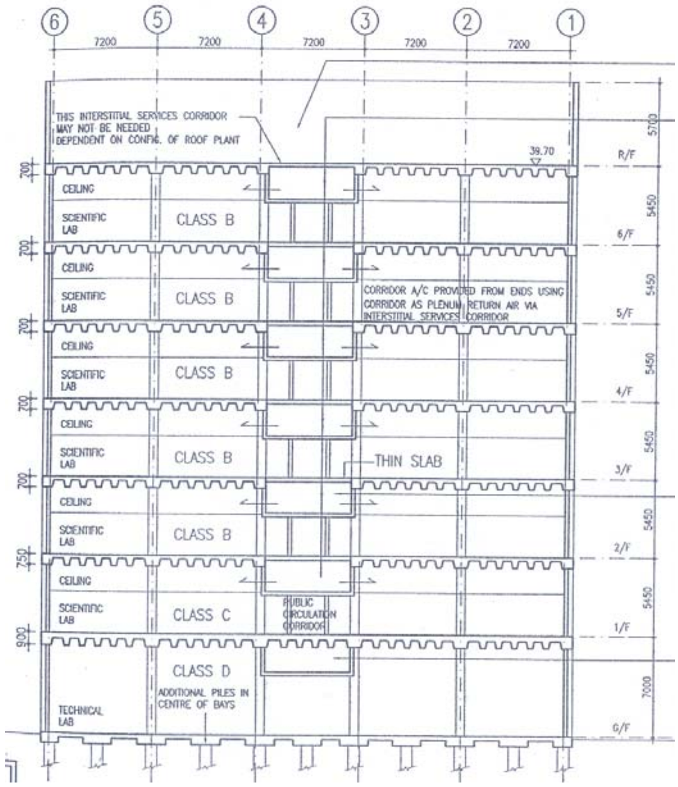

Figure 4.2 Cross section view of the laboratory building

Figure 4.2 illustrates the cross section view of the laboratory building. This building is 45.4m high. It has seven stories whose heights vary from 5.45m to 7m. With the information given in Figure 4.1 and Figure 4.2, it is known that the metal structure of the laboratory building is mainly made from the RC bars bundles embedded inside the columns and beams. By simplifying a RC bars bundle in columns and beams into a cylindrical conductor shown in Chapter 3, the metal structure of the building was transformed to a wire-grid structure as seen in Figure 4.3. Some assumptions are adopted in the transformation:

- The influence of the reinforcing concrete wall and floors on LIMF distribution is not considered because they has little function in shielding electromagnetic field [Casinovi et.al., 1989].

- The earth resistance is considered as 100ohm.

- The lightning channel is simply considered as a cylindrical conductor with height 100m. This assumption is also adopted in the IEC Standard [IEC 61312-2, 1995]

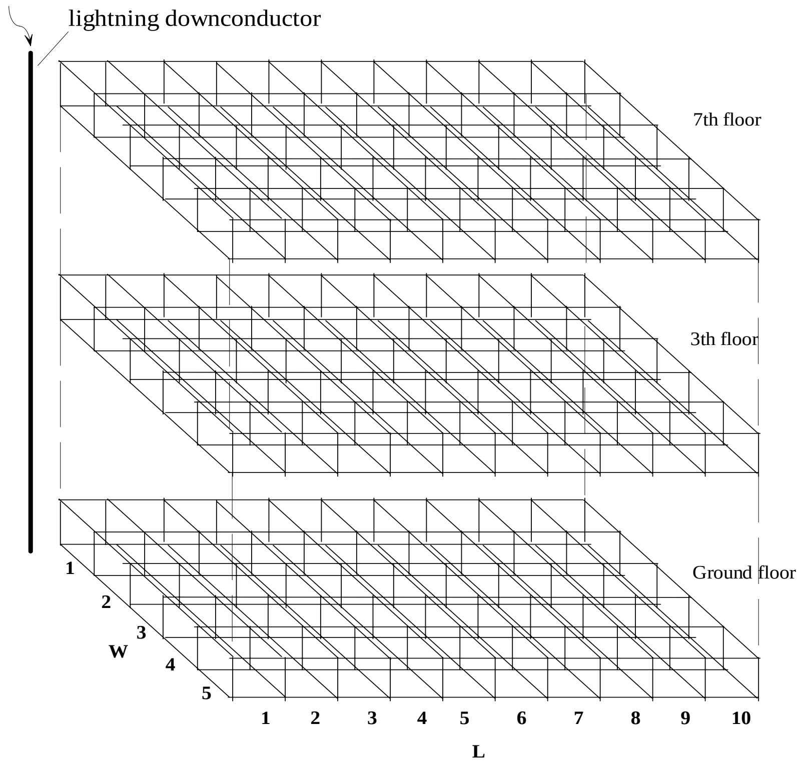

Figure 4.3 Wire-grid structure of the lab building

This laboratory building is protected by the ESE LPS with an isolated downconductor. This downconductor is as high as the building, and has mean diameters of 12.3mm and 24.1mm for its core and screening, respectively. The downconductor is mounted on the walls and runs vertically. Its upper terminal is connected to the air terminal on the roof and the lower terminal is connected with the earthing electrode which is buried inside the earth. Both the air terminal and the downconductor are located either in the center or at the corner of the building.

4.3 Distrubtion of LIMF inside the Building

With the EC modeling approach and solution procedure proposed in Chapter 3, the wire-grid structure of the building was transformed to an equivalent circuit network comprising resistance, inductance and capacitance. The current distribution in the structure and the impulse magnetic field inside the building were evaluated. In order to present LIMF distribution clearly, an observation line in the building were selected and the impulse magnetic field along this line was calculated during a direct lightning striking at the air terminal. The observation line runs from one corner of the building (column a) to its opposite corner (column f) on 3/F, as seen in Figure 4.4.

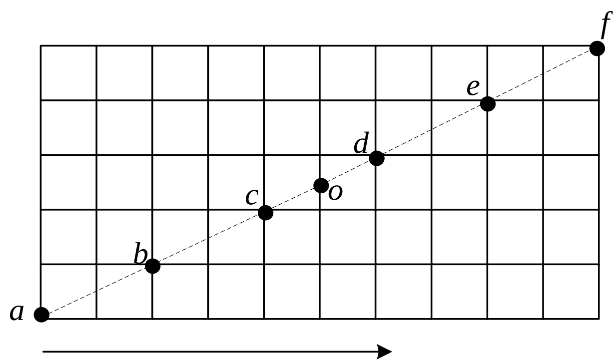

Figure 4.4 Top view of 3/F and the observation line for field calculation

In the evaluation of LIMF inside the building, the lightning stroke to the building was simulated to be a current source as stated in Chapter 3. The front-time and tail-time constants τ_1 and τ_2 in (3.8) were taken to 8μs and 10μs, respectively. The peak value of the current I_m was selected to be 160kA. With these parameters, the current has an effective peak value 100kA for $n = 2$, and a waveform of 8/20μs (time to peak value/time to half peak value).

4.3.1 Downconductor Mounted on a Wall

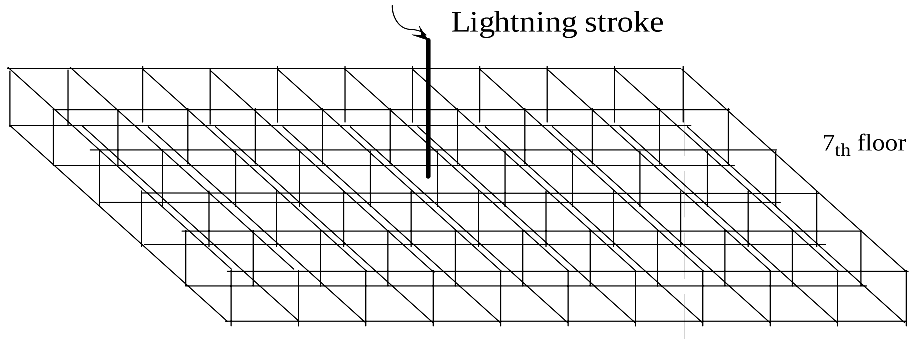

Figure 4.5 Downconductor installed in the building

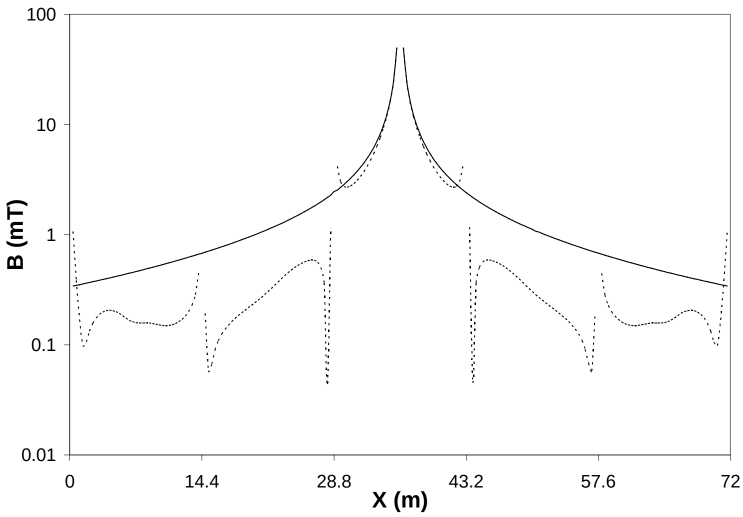

--- with the structure —— without the structure

Figure 4.6 Impulse magnetic fields in the case of Downconductor in the center

The isolated downconductor is usually mounted on the wall either in an electrical duct or on façade. When the downconductor is located inside the building structure at point *o* as Figure 4.5 shows, the peak values of impulse magnetic fields over the observation line are illustrated in Figure 4.6. In order to reveal the shielding effect of the wire grid, the impulse magnetic fields along the observation line without the wire grid are also calculated. It is noted that the impulse magnetic fields are significantly high in the area between columns *c* and *d* (critical area). The peak value of the field reaches 49.5mT at the point 0.36m away from the downconductor. The field, however, is generally less than 1mT outside this area.

For comparison, the peak values of impulse magnetic fields in the absence of the wire grid were superimposed on these figures. The fields are solely determined by the discharge current in the downconductor. It is noted from the figures that the fields are generally less in the presence of the wire grid. Such field cancellation generally arises from the currents induced within the wire grid. The field cancellation becomes stronger on the middle floors (e.g., 3/F), as seen in the figures. As an induced current has a significant influence on the field near its carrier (e.g., column), local field enhancement around columns is also observed in the figures. The field can be even greater than that in the absence of the wire grid at certain locations.

When the LPS is installed at the corner of the building as Figure 4.7 shows, the peak values of the impulse magnetic fields along the observation line is shown in Figure 4.8. In general these impulse magnetic fields have a similar pattern as those in the previous case. The fields generated from the downconductor are partially cancelled by the induced current. In this case, such field cancellation in the critical area is even more significant. The peak value of the field reaches 5.7mT at the point 0.36m away from column *a*. As the induced currents in columns *a* and *b* flow in opposite directions, the field cancellation in this area is enhanced.

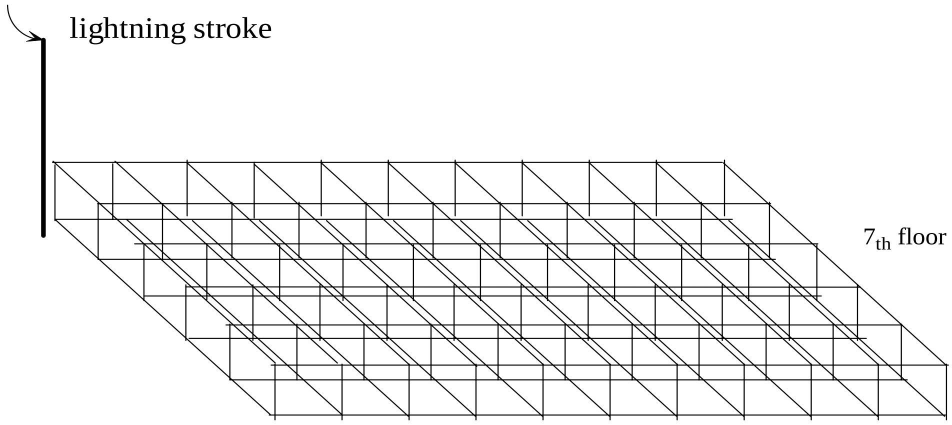

Figure 4.7 Downconductor installed at the corner

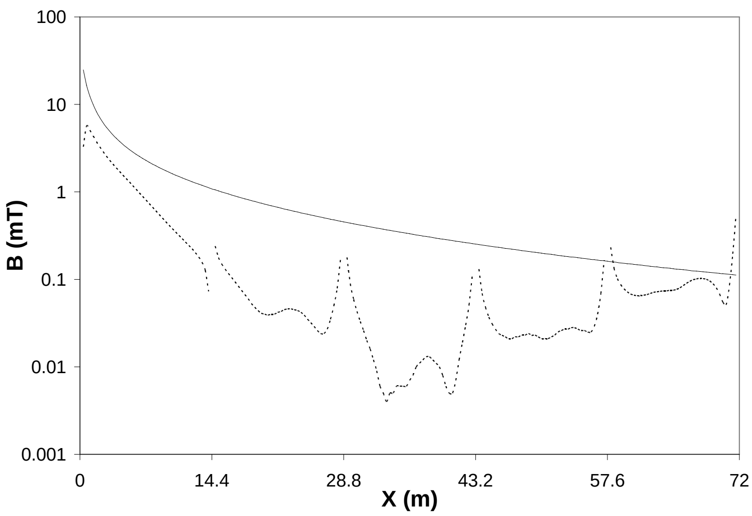

--- with the structure — without the structure

Figure 4.8 Impulse magnetic fields in the case of downconductor at the corner

4.3.2 Downconductor Enclosed in a Metal Pipe

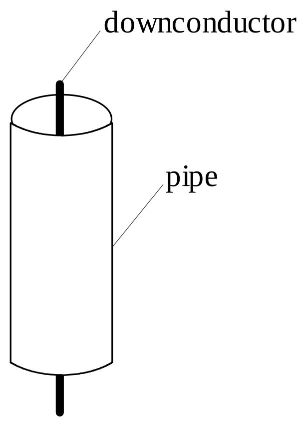

Figure 4.9 Configuration of a downconductor enclosed by a metal pipe

It is noted that impulse magnetic fields are significantly high in the area close to the downconductor. The situation can be improved if a conductive loop is constructed in this area to compensate the original field. In order to enhance field compensation it is necessary to use certain measures to increase the induced current in the loop. As seen in Figure 3.4, the downconductor has a conductive screening. When the screening is isolated from the wire grid, it has little effect on shielding the magnetic field. However, when the screening is bonded to the wire grid at its both ends, the induced current will be significantly increased. Unfortunately the screening is not designed to carry the lightning current. The connection to the wire grid is not recommended by the manufacturers in practice.

To achieve a similar performance, a separate metal pipe is introduced to house the downconductor, and to carry the induced current. This pipe has a diameter of 0.2m and a thickness of 10mm. It is bonded to the wire grid on the ground as well as on the roof. As the induced current in the pipe flows in the opposite direction of the downconductor current, significant reduction of the impulse magnetic field is expected in the critical area around the downconductor.

Figure 4.10 shows the peak values of impulse magnetic fields when the LPS are situated in the center of the building. Clearly the impulse magnetic fields become less in the critical area. The highest peak value is reduced to 2.75mT from 49.5mT on 3/F. However, this pipe does not have a significant impact on the field at a location away from the downconductor, as illustrated in the figure.

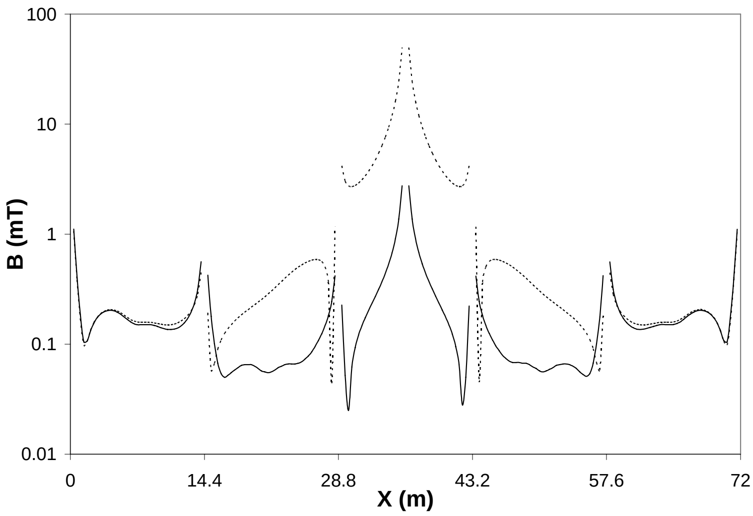

--- without the pipe —— with the pipe

Figure 4.10 Impulse magnetic fields in the case of downconductor enclosed by a pipe in the center

Figure 4.11 shows the peak values of impulse magnetic fields when the LPS is situated at the corner of the building. Similar to the previous case, the impulse magnetic fields are generally less in the critical area when the pipe is installed. On the 3/F the highest peak value is reduced to 3.80mT from 5.65mT.

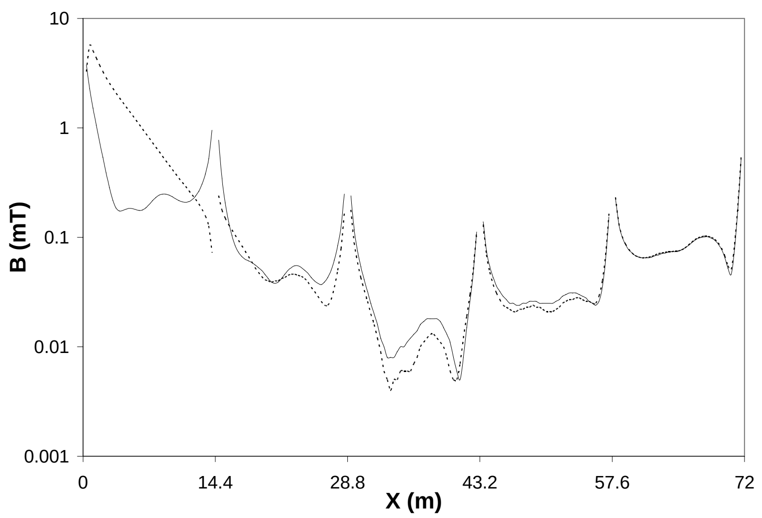

--- without the pipe —— with the pipe

Figure 4.11 Impulse magnetic fields in the case of downconductor enclosed by a pipe at the corner

4.4 Summary

This chapter investigated the impulse magnetic fields arising from the discharge current in an isolated downconductor installed in a real laboratory building in Hong Kong. The building structure as well as the isolated downconductor was transformed to an equivalent circuit network by using the equivalent circuit (EC) modeling approach. The current distribution and consequent LIMF inside the building structure in the building were evaluated during a direct lightning stroke at the LPS.

From the evaluation results, it is concluded that

- LIMF around an isolated downconductor is significantly high, and can be as high as that generated from a standalone downconductor. It is highly recommended not placing sensitive equipment in the area near the downconductor.

- Reinforcing bars of columns and beams in the building can attenuate the impulse magnetic field if they are interconnected each other. Because of the induced currents in these bars the impulse magnetic field is reduced. It is recommended placing the downconductor next to a column or outside the building in order to achieve significant field compensation in the area around the downconductor.

- To enhance the field compensation further it is recommended housing the downconductor with a metal pipe, and bonding both the metal pipe and metal structure of the building together. A large induced current will be generated in the pipe to compensate the field from the downconductor. The field can be reduced down to 10% of its value without the pipe in some cases. This pipe, however, does not have a significant impact on the field at the location away from the downconductor.

Chapter 5

Empirical Formulas for Evaluating Shielding Effect of a Wire-grid Building Structure

5.1 Introduction

With the equivalent circuit (EC) modeling approach developed in Chapter 3, the lightning-induced impulse magnetic field (LIMF) inside the wire-grid building structure can be evaluated numerically. It is known that the dimension and grid width of the building structure varies from one building to another. To avoid the time-consuming evaluation it would be necessary to have simple formulas, which can be applied to different types of wire-grid building structures. These formulas will help engineers to evaluate the shielding effect of the building structure and to assess the threat of LIMF qualitatively.

In IEC Standard 61312-2 [IEC 61312-2], a simple empirical formula for evaluating the shielding effect of the wire-grid building structure is presented. This formula, however, is only applicable for the building structure under parallel-plane incident magnetic field generated by a distant lightning stroke. When a lightning stoke is very close to the building of concern, e.g. striking at an outside isolated downconductor or at adjacent building structures, the incident magnetic field cannot be treated as a parallel-plane field, and then the formula in the IEC Standard is not applicable any more. In this chapter, more general formulas will be derived.

This chapter starts with a description of the wire-grid building structure of concern. A preliminary study on the relationship between the structure parameters and shielding effect is then conducted. General observations are obtained through numerical calculation. With these observations, the quantitative relationships between these parameters and shielding effect are built. By using the curve fitting technique and induction approach, these relationships are transformed to close-form formulas.

5.2 Configuration of the Wire-grid Building Structure

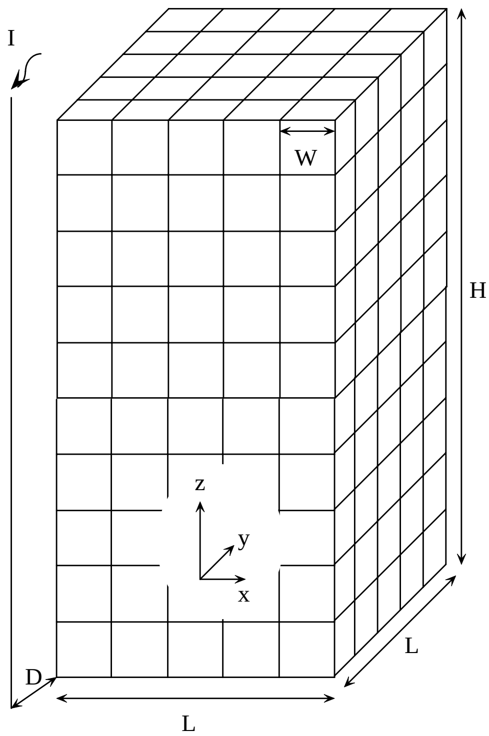

(a) 3D diagram of the concerned structure

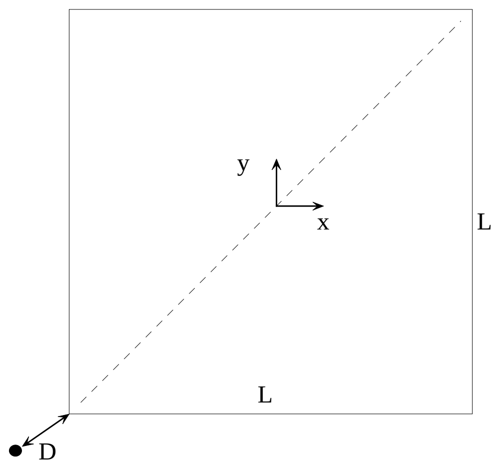

(b) Plan view of the concerned structure

Figure 5.1 Configuration of the wire-grid building structure

Figure 5.1(a) illustrates the 3D configuration of the wire-grid structure under discussion in this chapter. This structure is a Faraday's cage which is similar to that used in IEC standard 61312-2 [IEC 61312-2, 1995]. The nearby lightning stroke is modeled as a lightning stroke terminated at an isolated downconductor adjacent to a corner of the building. The structure has the dimensions of L (length) × L (width) × H (height), and has the square mesh with the grid width of W. For simplicity the structure length is set to be equal to its width. The distance between the isolated downconductor and the nearest structure corner is denoted by D.

5.3 Preliminary Study

With the EC modeling approach developed in Chapter 3, the wire-grid building structure together with the isolated downconductor can be transformed to an equivalent circuit network. The current distribution in the equivalent network is evaluated numerically. LIMF inside the building structure can then be calculated. In order to study the shielding effect of the wire-grid building structure, a parameter of Shielding Factor (SF) is introduced, and is give by

$$SF = \frac{B_1}{B_o} \times 100\% \tag{5.1}$$

where B_1 is the magnetic field in the presence of the building structure and B_0 is the magnetic field without the building structure.

SF varies with the parameters of building structure such as L, H, D and W. The following sections describe the relationship between SF and these parameters via numerical calculations.

5.3.1 Steady Region inside the Building Structure

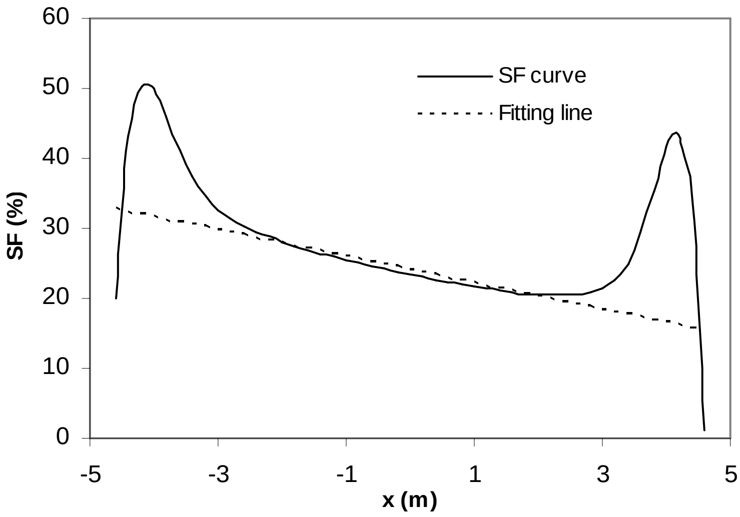

Figure 5.2 SF curve along the x coordinate

The preliminary study starts with an identification of SF distribution inside the wire-grid building structure along the dotted diagonal lines shown in Figure 5.1 (b) at different heights. Through the calculation with different building parameters, it is found that SF along the diagonal line of the structure has a similar distribution no matter what structure dimensions, grid dimensions, and height of the observation line are, as illustrated in Figure 5.2. For simplicity, the shielding factor on the diagonal line is expressed and/or plotted against the x coordinate.

Figure 5.2 illustrates the horizontal distribution of SF inside a building structure with dimensions of $\mathrm{L} = 10m$, $\mathrm{H} = 40m$ and grid width of $\mathrm{W} = 1m$. From Figure 5.2, it is noted that SF curve has a shape of saddle. In the middle region with the distance of

W to the two opposite structure edges, SF curve can be approximately represented with a straight line.

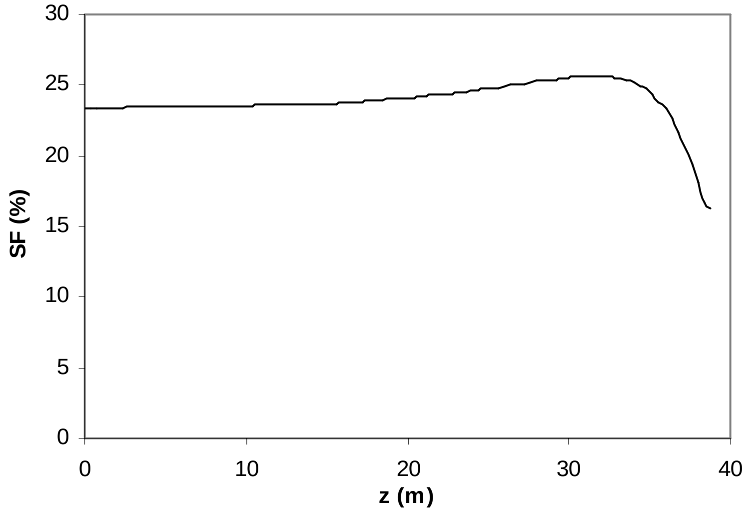

Figure 5.3 SF curve along the z coordinate

Figure 5.3 shows the vertical distribution of SF inside the building structure along the z direction when x and y are set to be zero. From Figure 5.3, it is found that in the region below the roof with a distance about 10m, SF remains constant nearly.

According to the observations obtained from Figure 5.2 and 5.3, a 3-D region inside the building is selected for discussion as most of sensitive equipment is often placed in this region. This region is called the steady region, and is limited by horizontal boundary of $\left[-\frac{L}{2}+W, \frac{L}{2}-W\right]$ and vertical boundary of $\left[0, H-10m\right]$.

From Figure 5.2, it is known that SF distribution inside the steady region can be approximated by a straight line. So empirical formulas are a linear function depending on the parameters of L, H, D and W. In order to disclose the relationship between SF and those parameters, SF is characterized against structure parameters via numerical calculations in the preliminary study.

5.3.2 Impact of Distance D while the Parameters of L, W and H are Fixed

A. Simulation Results

Firstly, the impact of the distance D on SF is studied. Figure 5.4 shows the SF curves against the distance D while L, W and H are chosen randomly as =10m, W=2m and H=40m. According to the pattern of SF curves, three groups of curves are presented in Figure 5.4.

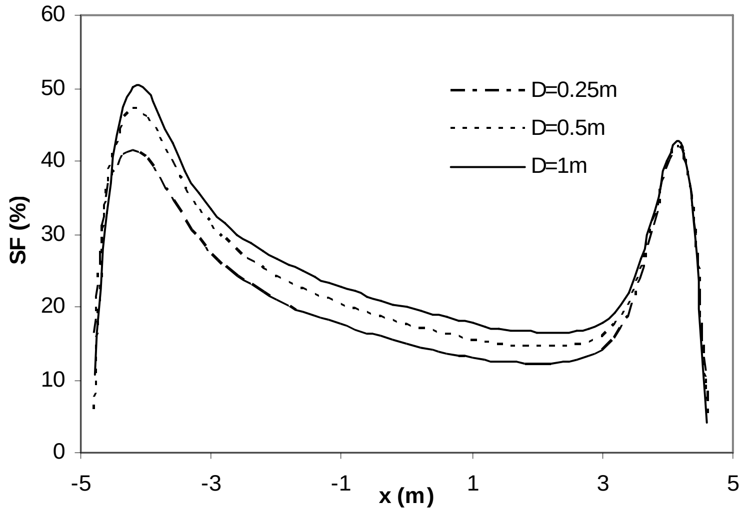

(a) D≤W

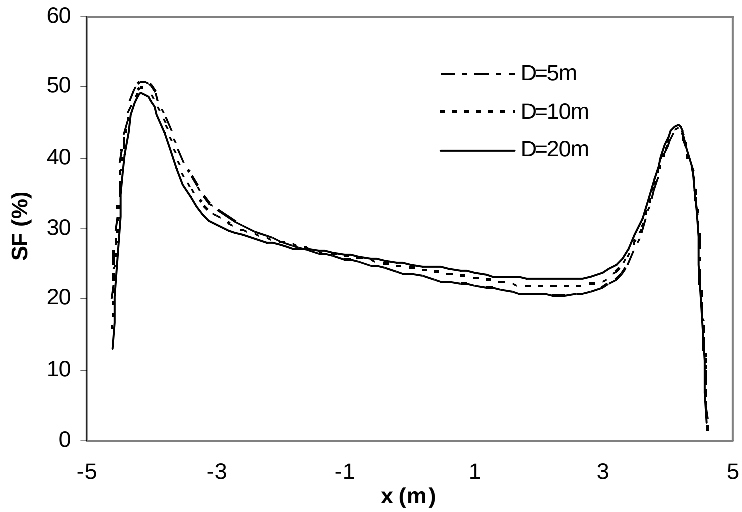

(b) W≤D≤10W

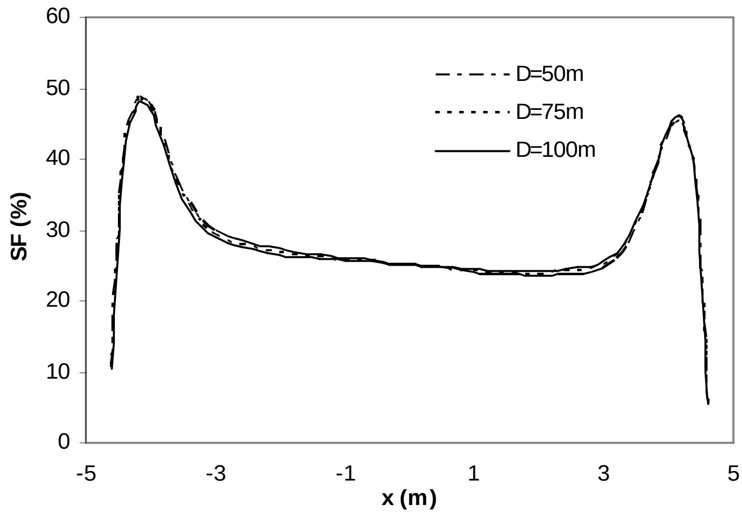

(c) 10W≤D

Figure 5.4 SF curves for different D

B. Observations

From Figure 5.4, some observations are found as follows

1) When D≤W, SF curves shifts upward with increasing D, and are approximately in parallel. These curves have the same gradient generally. It is inferred that the gradient of fitting lines is independent of D while the interception point is determined by the parameter D.

2) When W≤D≤10W, SF curves twists around a point at $x = -0.32L$ with increasing D. At this time, both gradient and interception point of fitting lines are depending on the parameter D.

3) When $10W \leq D$, SF curves will twist around the center point at x=0 with increasing D. Similarly both gradient and interception point of fitting lines are depending on the parameter D.

These phenomena are also observed for other values of parameters L, H and W.

5.3.3 Impact of Distance W while the Parameters of L, D and H are Fixed

A. Simulation Results

Secondly, the impact of W on SF is studied. By choosing L=6m, D=5m and H=40m optionally, SF curves under different W are plotted in Figure 5.5.

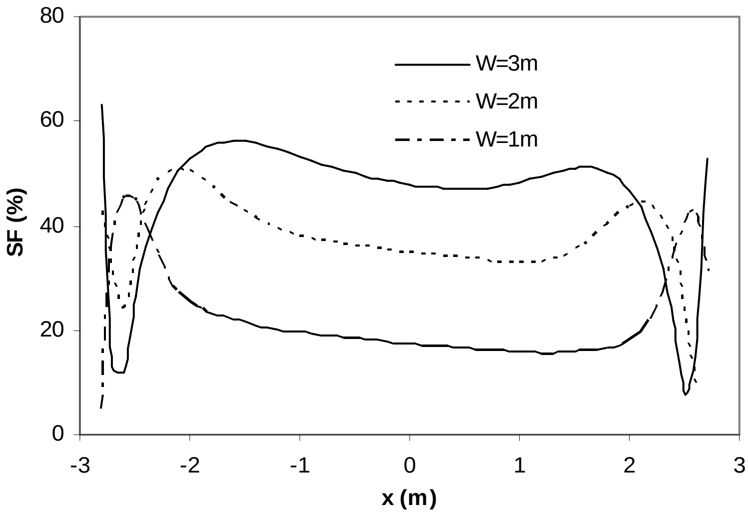

Figure 5.5 SF curves for different W

B. Observations

In Figure 5.5, three SF curves respectively for W=1m, 2m and 3m are illustrated. From Figure 5.5, it is found that when L and D are fixed, SF curves will shift downward with decreasing W. It means that the gradient of the fitted lines will keep constant and only intercepts will change. So it can be inferred that the gradient of fitting lines is independent to W while the interception point is depending on W. These phenomena are also observed for other values of parameters L, H and D.

5.3.4 Impact of Distance L while the Parameters of H, D and W are Fixed

A. Simulation Results

Thirdly, the impact of L on SF is studied. By choosing W=2m, D=5m and H=40m optionally, SF curves for different L are plotted in Figure 5.6.

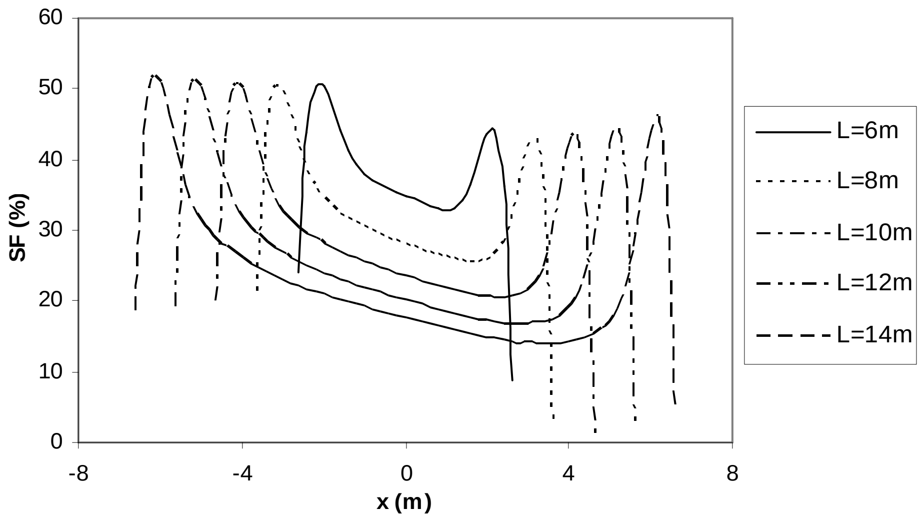

Figure 5.6 SF curves for different L

B. Observations

In Figure 5.6, there are five curves respectively for L=6m, 8m, 10m, 12m and 14m. From these curves, it is noted that when H, D and W are fixed values, SF curves will shift downward with increasing L. It means that the gradient of the fitted lines will keep constant and only intercepts will change with L. So it can be inferred that the gradient of fitting lines is independent to L while the intercept is determined by L. These phenomena are also observed for other values of parameters W, H and D.

5.3.5 Fitted Lines of SF Curves

From above observations, it is found that the gradient of the fitted line is only dependent on D. The gradient, therefore, is considered as a function of D only. In addition, it is found that the intercept of the fitted line is dependent on D, L and W. But as Figure 5.4 (b) and (c) show, the fitting lines of SF curves cross over at a point in the region of D>W. If this crossing point is chosen as origin point, the dependence of intercept of fitting lines on D can be eliminated.

From the above discussion, it is inferred that the fitting line has a representative function, as follows

$$SF(x) = k(D)(x - m) + b(W, L, D) \tag{5.2}$$

where $x \in [-L/2 + W, L/2 - W]$. The gradient $k(D)$ is different in three regions determined by D. When D≤W, m =0. When D>W, m is the crossing-point coordinate of fitting lines. At this time, the intercept item $b(W, L, D)$ can be simplified to be $b(W, L)$.

5.4 Derivation of the Empirical Formulas

From the preliminary study in Section 5.3, it is found that in the steady region of a wire-grid structure, a SF curve can be approximated by a linear fitting line with the expression given in (5.2). The gradient of fitting line k and the intercept b in (5.2) are derived for three regions, respectively.

5.4.1 Formulas of both k and b for D≤W

A. Relationship between the Gradient k and D

From Figure 5.4 (a), it shows that the fitting lines of SF curves against D are approximately in parallel with each other. So the gradient $k(D)$ is a constant, and is equal to - 0.024 from the simulation. Then the fitting line function becomes

$$SF\left(x\right) = -0.024x + b\left(W, L, D\right) \tag{5.3}$$

In (5.3), the intercept b is determined on W, L and D.

B. Relationship between Intercept b and the Parameters W, L and D

The relationship between W and D is studied first. L is always proportional to W with the ratio of K. Once the relationship between W and D is revealed, the relationship between L and D can be derived directly. For a fixed k and various W and D, the SF values at the center of the curves are just equal to the intercept b values, and listed in Table 5.1.

Table 5.1 Intercept b for various W and D when fixed K =3,4,5,6

$K=3$	W=1	W=2	W=3
D=0.25	0.232	0.242	0.242
D=0.5	0.263	0.283	0.286
D=0.75	0.276	0.302	0.308
D=1	0.284	0.313	0.322
D=2	0.296	0.334	0.348

$K = 4$	W=1	W=2	W=3
D=0.25	0.176	0.186	0.187
D=0.5	0.202	0.219	0.223
D=0.75	0.214	0.235	0.241
D=1	0.221	0.245	0.253
D=2	0.234	0.265	0.277

$K = 5$	W=1	W=2	W=3
D=0.25	0.139	0.148	0.150
D=0.5	0.161	0.175	0.180
D=0.75	0.172	0.189	0.196
D=1	0.179	0.199	0.207
D=2	0.192	0.217	0.229

$K = 6$	W=1	W=2	W=3
D=0.25	0.114	0.121	0.126
D=0.5	0.133	0.144	0.151
D=0.75	0.143	0.157	0.165
D=1	0.149	0.165	0.175
D=2	0.161	0.182	0.195

In Table 5.1, four sub-tables list the values of b against W and D when the ratio between L and W changes from 3 to 6. These values are plotted against D curves for different K and W in Figure 5.7. The curves in Figure 5.7 can be divided into 4 groups corresponding to K =3, 4, 5 and 6. Each group includes four curves corresponding to W=1, 1.5. 2 and 3.

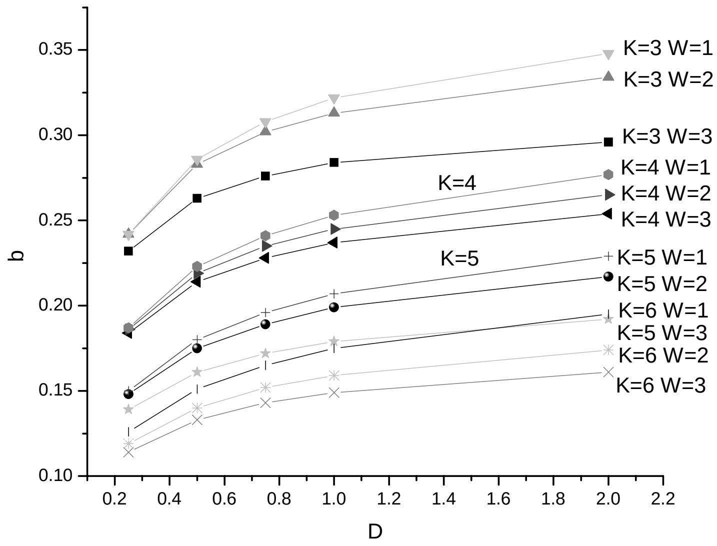

Figure 5.7 b -D curves

If the parameter of D in Figure 5.7 is transformed to $\frac{1}{\sqrt{D}}$, the b - $\frac{1}{\sqrt{D}}$ curves can be approximated by lines as Figure 5.8 shows. Then b can be represented by a line function as follows

$$b(W, D, K) = K_1(W, K)\frac{1}{\sqrt{D}} + K_2(W, K) \tag{5.4}$$

By reviewing the curves for different K, it is found that when W is fixed and K varies, b - $\frac{1}{\sqrt{D}}$ curves are almost in parallel, namely the fitting lines of b have the same gradient K_1. So the gradient K_1 is independent of K.

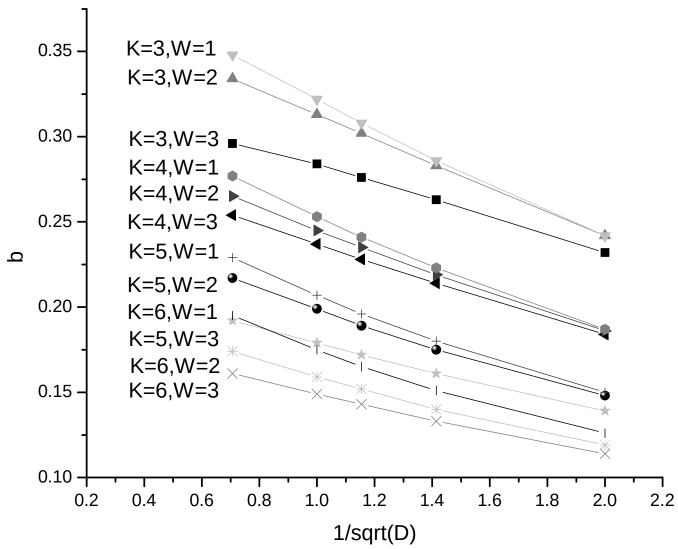

Figure 5.8, b - $\frac{1}{\sqrt{D}}$ curves

By setting the origin of the local coordinate system at the crossing point of a group of fitting lines in Figure 5.8, the influence of W on the intercept K_2 of b function is eliminated. Then the intercept K_2 is only determined by K. At this time, (5.4) is transformed to the following expression

$$b(W,D,L) = K_1'(W)\left(\frac{1}{\sqrt{D}} - m\right) + K_2'(K) \tag{5.5}$$

where m is the x coordinate of the crossing point.

1). Derivation of $K_1'(W)$

A series of b - $\frac{1}{\sqrt{D}}$ lines for various K and W are obtained from the numerical calculations. The expressions of these lines are listed in Table 5.2. In Table 5.2, $\frac{1}{\sqrt{D}}$ is denoted by D' for simplification.

Table 5.2 Expression of b - D' for various K and W

K =3

W=3	$b = 0.40385 - 0.06817D'$
W=2	$b = 0.38419 - 0.06121D'$
W=1.5	$b = 0.36458 - 0.05312D'$
W=1	$b = 0.33304 - 0.04406D'$

K =4

W=3	$b = 0.32272 - 0.06893D'$
W=2	$b = 0.30623 - 0.06073D'$
W=1.5	$b = 0.2911 - 0.05394D'$
W=1	$b = 0.26582 - 0.04495D'$

K =5

W=3	$b = 0.26819 - 0.06938D'$
W=2	$b = 0.25214 - 0.06001D'$
W=1.5	$b = 0.24483 - 0.05446D'$
W=1	$b = 0.21992 - 0.04489D'$

K =6

W=3	$b = 0.22843 - 0.06726D'$
W=2	$b = 0.21241 - 0.05969D'$
W=1.5	$b = 0.20177 - 0.05349D'$
W=1	$b = 0.18543 - 0.04401D'$

From four groups of lines for K =3, 4, 5 and 6, it is found that every group of lines approximately crosses at a point with coordinate of $D' = 2.6$, namely m =2.6 in (5.5). By moving the origin of the coordinate system to this point, the functions in Table 5.2 are modified with representation (5.5) listed in Table 5.3.

Table 5.3 Modified b - D' expressions

K =3

W=3	$b = 0.19912 - 0.06817(D' - 2.6)$
W=2	$b = 0.19903 - 0.06121(D' - 2.6)$
W=1.5	$b = 0.20306 - 0.05312(D' - 2.6)$
W=1	$b = 0.20288 - 0.04406(D' - 2.6)$

K =4

W=3	$b = 0.1435 - 0.06893(D' - 2.6)$
W=2	$b = 0.14833 - 0.06073(D' - 2.6)$
W=1.5	$b = 0.15087 - 0.05394(D' - 2.6)$
W=1	$b = 0.14895 - 0.04495(D' - 2.6)$

K =5

W=3	$b = 0.1112 - 0.06838(D' - 2.6)$
W=2	$b = 0.11431 - 0.06001(D' - 2.6)$
W=1.5	$b = 0.11883 - 0.05446(D' - 2.6)$
W=1	$b = 0.11361 - 0.04489(D' - 2.6)$

K =6

W=3	$b = 0.09166 - 0.06726(D' - 2.6)$
W=2	$b = 0.091 - 0.05969(D' - 2.6)$
W=1.5	$b = 0.09205 - 0.05349(D' - 2.6)$
W=1	$b = 0.09133 - 0.04401(D' - 2.6)$

From Table 5.3, it is found that the gradients of lines are almost equal for the same grid width. This observation is in accordance with (5.5) that K_1' is a function of W. With the average gradient for each W, a curve of K_1'-W is plotted in Figure 5.9.

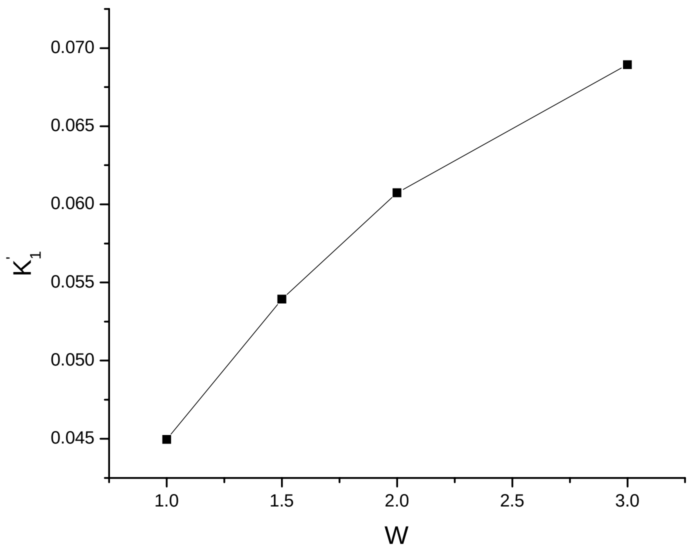

Figure 5.9 K_1'-W curve

The curve in Figure 5.9 is fitted by a function given by

$$K_1' = \frac{0.079}{W^{1/3}} - 0.123 \tag{5.6}$$

Thus, b function can be represented by

$$b = (\frac{0.079}{W^{1/3}} - 0.123)(\frac{1}{\sqrt{D}} - 2.6) + K_2'(K) \tag{5.7}$$

2). Derivation of K_2'

It has been found that the intercept of b is only determined by K. So a group of lines for the same grid width, e.g. W=1, in Table 5.3 is selected. The intercepts of these lines with respect to K are plotted in Figure 5.10.

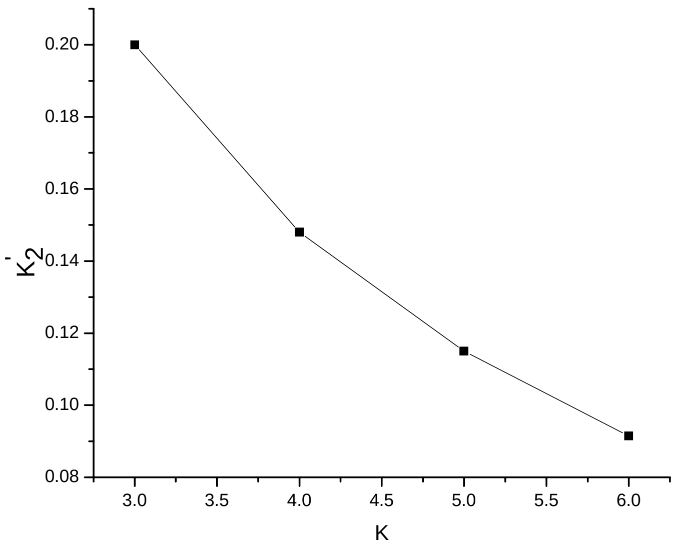

Figure5.10 K_2'-K curve

The K_2'-K curve in Figure 5.10 can be approximated by a function as follows

$$K_2' = -0.01539 + \frac{0.6485}{K} \tag{5.8}$$

By substituting (5.7) and (5.8) into (5.5), an empirical formula for evaluating SF when D≤W is obtained as follow

$$SF(x) = -0.024x + (\frac{0.079}{W^{1/3}} - 0.123)(\frac{1}{\sqrt{D}} - 2.6) + (\frac{0.6485}{K} - 0.01539) \quad (5.9)$$

where $x \in [-L/2+W, L/2-W]$.

5.4.2 Formulas of both k and b for W≤D≤10W

From the preliminary study, it is found that when D varies from W to 10W, the SF fitting lines will cross at the point with the coordinate x=0.32L. Then influence of the D to intercept can be eliminated by moving the coordinate origin to this point. At this time, the SF can be represented as

$$SF(x) = k(D)(x - 0.18L) + b(W, K) \quad (5.10)$$

where $x \in [-L/2+W, L/2-W]$.

A. The Relationship between D and k

From the numerical calculation, a curve between k and D is plotted in Figure 5.11.

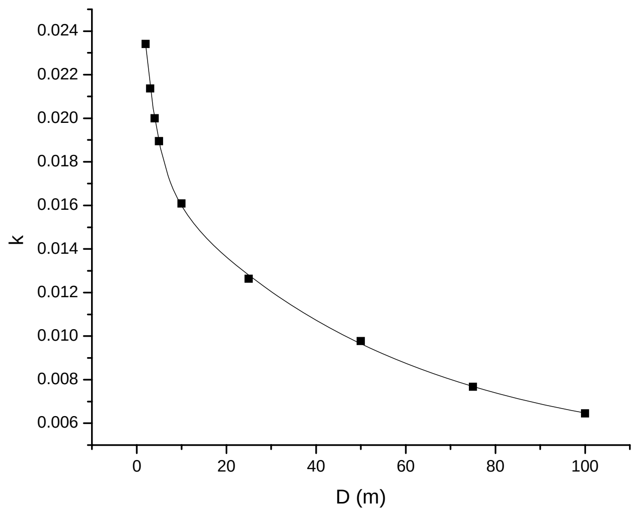

Figure 5.11 the curve between k and D

This curve can be fitted by a double exponential function with the expression:

$$k(D) = -0.0044 - 0.01339e^{\left(-\frac{D}{52.98}\right)} - 0.01142e^{\left(-\frac{D}{3.117}\right)} \tag{5.11}$$

B. The Relationship between W, L and b

By selecting D=5m and x=-0.18L， SF is equal to its intercept b. At this time, b values for various W and K are calculated and listed in Table 5.4

Table 5.4 b for various W and K

K	W=3	W=2	W=1.5	W=1
2	0.534	0.508	0.488	0.454
3	0.412	0.385	0.359	0.328
4	0.344	0.320	0.297	0.265
5	0.297	0.275	0.254	0.225
6	0.261	0.242	0.223	0.196
7	0.235	0.219	0.198	0.174
8	0.214	0.201	0.180	0.162

For each W, a curve between b and K is plotted Figure 5.12.

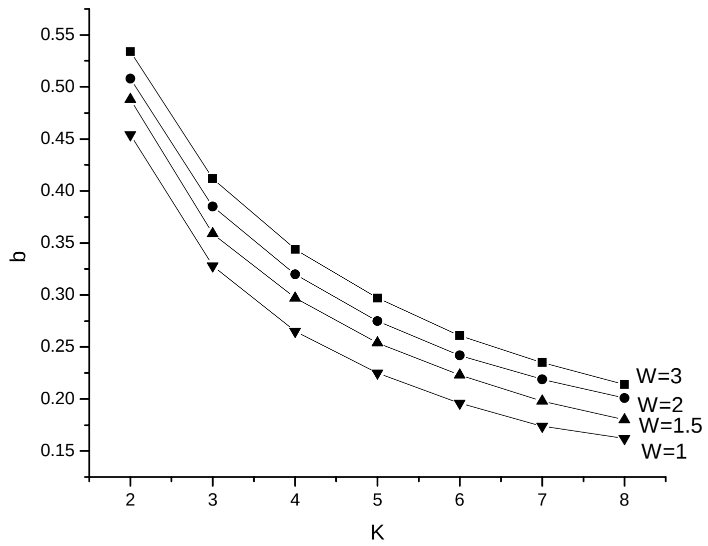

Figure 5.12 b-K curves

If K coordinate is transformed to $\frac{1}{\sqrt{K}}$, the b-K curves in Figure 5.12 can be approximated by lines shown in Figure 5.13.

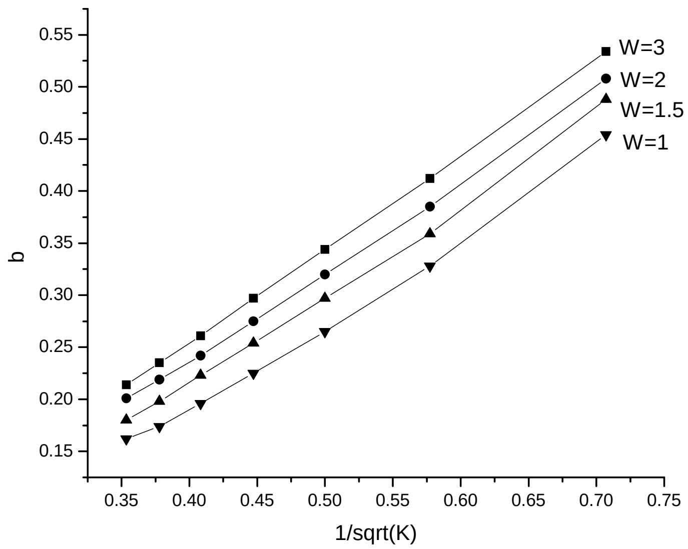

Figure 5.13 b-$\frac{1}{\sqrt{K}}$ curve

Then b can be represented by a line function as follows

$$b = K_1(W)\frac{1}{\sqrt{K}} + K_2(W,K) \tag{5.12}$$

In order to eliminate W in the intercept K_2, the origin of coordinate is moved to the crossing point of the lines for different W. Then (5.12) can be modified as

$$b = K_1'(W)\left(\frac{1}{\sqrt{K}} - m\right) + K_2'(K) \tag{5.13}$$

where m is the $\frac{1}{\sqrt{K}}$ coordinate of the crossing point.

C. Derivation of K_1'

Firstly a series of $b-k'$ $(k' = \frac{1}{\sqrt{K}})$ lines are obtained from the numerical calculation result for different W. The functions of these lines are listed in Table 5.5.

Table 5.5 $b-k'$ lines

W=3	$b = -0.10714 + 0.90377k'$
W=2	$b = -0.11067 + 0.87749k'$
W=1.5	$b = -0.1301 + 0.85385k'$
W=1	$b = -0.14021 + 0.82619k'$

From the functions of lines in Table 5.5, it is found that the crossing point of these lines is about located at $m = -0.4$. By moving the coordinate origin to this point, the line functions can be modified and listed in Table 5.6.

Table 5.6 Modified $b-k'$ Lines

W=3	$b=-0.47+0.9038(k'+0.4)$
W=2	$b=-0.47+0.87749(k'+0.4)$
W=1.5	$b=-0.47+0.85385(k'+0.4)$
W=1	$b=-0.47+0.82619(k'+0.4)$

With the gradients K_1' of fours lines in Table 5.5, a curve function of W to fit these gradients is obtained as follows

$$K_1' = \frac{-0.18446}{\sqrt{W}} + 1.0083 \tag{5.14}$$

So a complete function of b is derived by applying (5.14) and $m=-0.4$ into (5.13)

$$b = (\frac{-0.18446}{\sqrt{W}} + 1.0083)(\frac{1}{\sqrt{K}} + 0.4) - 0.47 \tag{5.15}$$

With the derived $k(D)$, the empirical formula for evaluating SF when W≤D≤10W is given by

$$\begin{aligned} SF(x) = & \left(-0.0044 - 0.01339 e^{(-\frac{D}{52.98})} - 0.01142 e^{(-\frac{D}{3.117})} \right)(x + 0.32L) \\ & + (\frac{-0.18446}{\sqrt{W}} + 1.0083)(\frac{1}{\sqrt{K}} + 0.4) - 0.47 \end{aligned} \tag{5.16}$$

where $x \in [-\frac{L}{2} + W, \frac{L}{2} - W]$.

5.4.3 Formulas of both k and b for 10W ≤D

From the curved in Figure 5.4(c), it is found that the fitting lines of SF curves cross at a point with coordinate x=0. At this time, the fitting lines can be represented by following equation.

$$SF(x) = k\left(D\right)x + b\left(W, L\right) \quad x \in [-\frac{L}{2} + W, \frac{L}{2} - W] \tag{5.17}$$

With the similar curve fitting procedure in Section 1.4.2, the expression of gradient k and intercept b of the fitting lines are given by

$$k\left(D\right) = -0.0044 - 0.01339e^{(-\frac{D}{52.98})} - 0.01142e^{(-\frac{D}{3.117})} \tag{5.18}$$

$$b\left(W, K\right) = (\frac{-0.1843}{W} + 0.9479)(\frac{1}{\sqrt{K}} - 0.1) - 0.06 \tag{5.19}$$

Applying (5.18) and (5.19) into (5.17), the empirical formula to evaluate SF when D≥10W is given by

$$\begin{aligned} SF(x) = &\left(-0.0044 - 0.01339e^{(-\frac{D}{52.98})} - 0.01142e^{(-\frac{D}{3.117})} \right)x \\ &+ (\frac{-0.1843}{W} + 0.9479)(\frac{1}{\sqrt{K}} - 0.1) - 0.06 \end{aligned} \tag{5.20}$$

where $\quad x \in [-\frac{L}{2} + W, \frac{L}{2} - W]$

5.5 Valiation of Emprical Formulas

In order to validate the derived empirical functions, SF from numerical calculation and SF from the derived empirical functions are compared for the wire-grid structure with fixed parameters of H=40m, L=10m and W=2m. Two different values of the distance D are selected in the discussion.

1. Validation of Empirical Formulas for D ≤ W

When D＝0.25m, by substituting the parameters into (5.9), the empirical formula for D≤W is given by

$$SF(x) = -0.024x + 0.1505 \qquad x \in [-3, 3] \tag{5.21}$$

The SE curves from the numerical calculation and from the formula (5.21) are shown in Figure 5.14. It is noted that two curves in the center region are matched very well. In the middle region of the structure, the error is less than 1%.

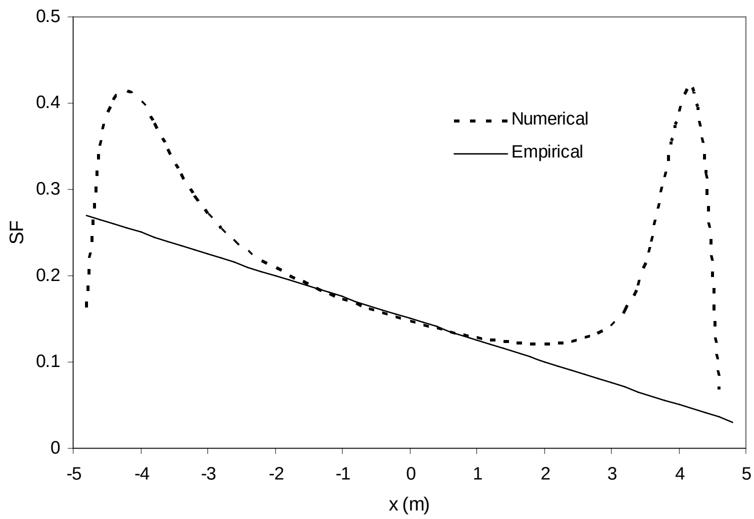

Figure 5.14 SF curves from the numerical calculation and the empirical formula

2. Validation of Empirical Formulas for W≤D≤10W

When D=5m, by applying the parameters value into the formula (5.16), the empirical formula for W≤D≤10W is given by

$$SF(x) = -0.0189(x+1.8)+0.2738 \qquad x \in [-3,3] \tag{5.22}$$

The SF curves from numerical calculation and from (5.22) are shown in Figure 5.15. It is noted that two curves in the center region are also matched very well. In the middle region of the structure, the error is less than 1%.

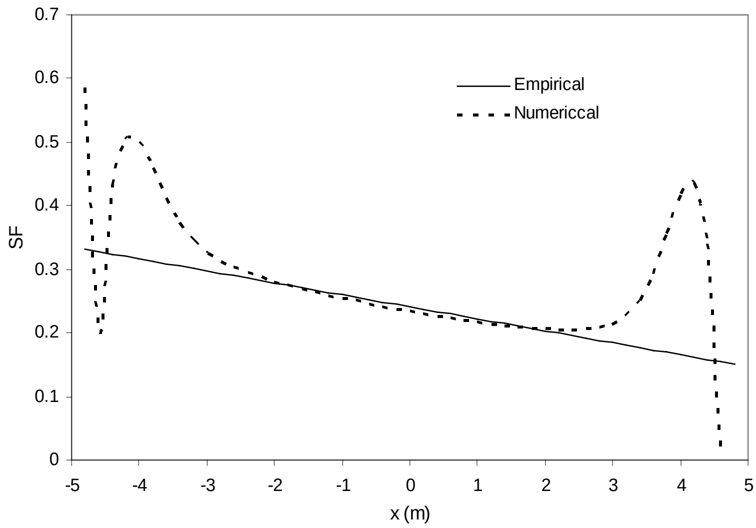

Figure 5.15 SF curves from the numerical calculation and the empirical formula

5.6 Summary

This chapter presented a series of empirical formulas, which could be used for evaluating the shielding effect of the wire-grid building structure against LIMF during a nearby lightning stroke. The preliminary study on the relationship between the structure parameters and shielding effect were conducted and general observations were obtained from the results of numerical calculation. Based on these observations, three empirical formulas were derived by the curve fitting technique according to the distance between the lightning stroke position and building structure. These formulas are summarized as follows:

$$SF(x) = -0.024x + (\frac{0.079}{W^{1/3}} - 0.123)(\frac{1}{\sqrt{D}} - 2.6) + (\frac{0.6485}{K} - 0.01539) \quad \text{for D} \le \text{W}$$

$$\begin{aligned} SF(x) = &\left(-0.0044 - 0.01339e^{(-\frac{D}{52.98})} - 0.01142e^{(-\frac{D}{3.117})} \right)(x + 0.32L) \\ &+ (\frac{-0.18446}{\sqrt{W}} + 1.0083)(\frac{1}{\sqrt{K}} + 0.4) - 0.47 \end{aligned} \quad \text{for W} \le \text{D} \le 10\text{W}$$

$$\begin{aligned} SF(x) = &\left(-0.0044 - 0.01339e^{(-\frac{D}{52.98})} - 0.01142e^{(-\frac{D}{3.117})} \right)x \\ &+ (\frac{-0.1843}{W} + 0.9479)(\frac{1}{\sqrt{K}} - 0.1) - 0.06 \end{aligned} \quad \text{for 10W} \le \text{D}$$

where $x \in [-\frac{L}{2} + W, \frac{L}{2} - W]$.

Chapter 6

Modeling Approach of Non-ferromagnetic Plates

6.1 Introduction

In previous chapters, lightning-induced impulse magnetic field (LIMF) inside a wire-grid building with isolated downconductors was extensively studied. The equivalent circuit (EC) modeling approach and corresponding solution procedure were developed. LIMF inside a real building was characterized. Empirical formulas for evaluating shielding effect were derived. These results can help researchers and engineers to evaluate the threat of LIMF to people and occupants inside the buildings.

In modern buildings large metal plates are widely applied for various purposes such as floor decking. Since a large metal plate can not be considered as a wire-like conductor, the EC modeling approach proposed in Chapter 3 is not applicable any more. In order to study LIMF inside the buildings with large metal plates, a new modeling approach is developed in this chapter.

This chapter starts with the derivation of electric field integral equation which is the foundation of the proposed modeling approach. Then, the partial element equivalent circuit (PEEC) approach for modeling non-ferromagnetic plates is developed. In this modeling approach, a hybrid cell generation method is firstly proposed which discretizes a plate into two types of cells. Among these cells, equivalent circuit equations with partial elements are built respectively for extremely low frequency situation and for full-wave frequency situation. In the full-wave situation, it is assumed that the current inside plates has a double exponential distribution. By interconnecting the equivalent circuits of all the cells, an equivalent circuit network consisting of partial elements is built for the whole plate. Finally a solution procedure in the frequency domain is presented for calculating the current distribution in the plate and subsequent magnetic fields around it. With the PEEC modeling approach, the shielding effect of non-ferromagnetic plates against either steady or transient magnetic field can be studied.

6.2 Modeling Approach of Non-ferromagentic Plates

6.2.1 Electric Field Integral Equation of Non-ferromagnetic Conductors

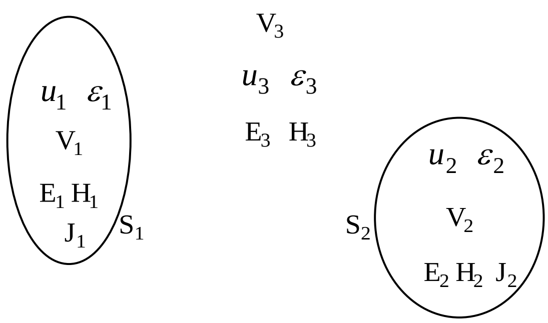

Figure 6.1 Three domains in space

Figure 6.1 shows two homogeneous and isotropic conductors in space. The space is divided into three domains which respectively have volume V_1, V_2, V_3 and surface S_1, S_2, S_3. It is easily noted that the surface S_3 is equal to the sum of S_1 and S_2. The permittivity μ and dielectric constant ε in each domain are denoted by subscripts 1, 2, 3. Inside three domains, electric field E and magnetic field H are also denoted by subscripts 1, 2, 3. Inside the conductor domain, current density J is denoted by subscripts 1 and 2 correspondingly. There is no current distributed in space because its conductivity is considered as zero. The Maxwell equations in the frequency domain in domain 1 are given by

$$\nabla \times E_1 = -j\omega u H_1 \tag{6.1.1}$$

$$\nabla \times H_1 = j\omega\varepsilon E_1 + J_1 \tag{6.1.2}$$

$$\nabla \cdot E_1 = 0 \tag{6.1.3}$$

$$\nabla \cdot H_1 = \rho_1 \tag{6.1.4}$$

By combining (6.1.1) and (6.1.2) , the following equation yields

$$\begin{aligned}\nabla \times \left(\nabla \times E_1\right) &= \nabla \times \left(-j\omega u_1 H_1\right)\\ &= -j\omega u_1\left(\nabla \times H_1\right)\\ &= -j\omega u_1\left(j\omega\varepsilon_1 E_1 + J_1\right)\end{aligned} \tag{6.2}$$

let $k_1^2 = \omega^2 u_1 \varepsilon_1$, then there is

$$\nabla \times \nabla \times E_1 - k_1^2 E_1 = -j\omega_1 u_1 J_1 \tag{6.3}$$

Given by the operator $L = \nabla \times \nabla \times -k^2$ and two functions F_1 and F_2, there is

$$F_2 \cdot L\left(F_1\right) - F_1 \cdot L\left(F_2\right) = \nabla \cdot \left[F_1 \times \nabla \times F_2 - F_2 \times \nabla \times F_1\right] \tag{6.4}$$

Integrating both sides of (6.4) over the plate volume and applying the Gauss Law, there is

$$\int_{V_1}\left(F_2 \cdot \nabla \times \nabla \times F_1 - F_1 \cdot \nabla \times \nabla \times F_2\right) dv = \int_{S_1}\left(F_1 \times \nabla \times F_2 - F_2 \times \nabla \times F_1\right) \cdot \hat{n} ds \tag{6.5}$$

where V_1 represents the volume of the domain 1 and S_1 represents the surface of the domain.

Choose F_2 as an arbitrary constant vector a times the Green function which fulfilling

$$\nabla^2 G + k_1{}^2 G = -\delta\left(r - r'\right) \tag{6.6}$$

Then there is

$$F_2 = aG_1\left(r, r'\right) \tag{6.7}$$

where $G_1\left(r, r'\right) = \dfrac{1}{4\pi}\dfrac{e^{-k_1|r-r'|}}{|r-r'|}$.

Upon use of the ∇ operation, there is

$$\nabla \times F_2 = \nabla G_1 \times a \tag{6.8}$$

Equation (6.8) is further transformed to

$$\begin{aligned} \nabla \times \nabla \times F_2 &= -a\nabla^2 G_1 + \left(a \cdot \nabla\right)\nabla G_1 \\ &= a\left(k_1{}^2 G_1 + \delta\left(r - r'\right)\right) + \nabla\left(a \cdot \nabla G_1\right) \end{aligned} \tag{6.9}$$

Choose $F_1 = E_1$ and use (6.1), (6.3), (6.7) and (6.9), equation (6.5) is transformed into

$$\begin{aligned} &\int_{V_1} \left\{aG_1 \cdot \left(-j\omega uJ\right) - E_1 \cdot a\delta\left(r - r'\right) - E_1 \cdot \nabla\left(a \cdot \nabla G_1\right)\right\} dV \\ &= \int_{S_1} \left\{E_1 \times \left(\nabla G_1 \times a\right) + j\omega_1 u_1 Ga \times H_1\right\} \cdot \hat{n} dS \end{aligned} \tag{6.10}$$

The last term on the left-hand side of (6.10) can be transformed into

$$\begin{aligned} \int_{V_1} E_1 \cdot \nabla\left(a \cdot \nabla G_1\right) dV &= \int_{V_1} \left\{\nabla \cdot \left(\left(a \cdot \nabla G_1\right) E_1\right) - \left(a \cdot \nabla G_1\right) \nabla \cdot E_1\right\} dV \\ &= a \cdot \int_{S_1} \nabla G_1 \left(E_1 \cdot \hat{n}\right) dS - a \cdot \int_{V_1} \frac{\rho_1}{\varepsilon_1} \nabla G_1 dV \end{aligned} \tag{6.11}$$

While the first term on the right-side hand of (6.10) can be transformed into

$$\begin{aligned}\int_{S_1} E_1 \times (\nabla G_1 \times a)\cdot \hat{n} dS &= \int_{S_1} (\nabla G_1 \times a)\cdot(\hat{n}\times E_1)\, dS \\ &= a\cdot\int_{S_1}(\hat{n}\times E_1)\times\nabla G_1 dS\end{aligned} \tag{6.12}$$

By substituting these results into (6.10) and collecting the volume integral terms on the left-hand side and the surface integral terms on the right-hand side, it is obtained that

$$\begin{aligned}&a\cdot\int_{V_1}\left\{-j\omega u_1 J_1 G_1 - E_1\delta(r-r') - \frac{\rho_1}{\varepsilon_1}\nabla G_1\right\}dV \\ &= a\cdot\int_{S_1}\left\{(\hat{n}\times E_1)\times\nabla G_1 + (\hat{n}\times E_1)\times\nabla G_1 + j\omega_1 u_1 G_1 H_1 \times \hat{n}\right\}dS\end{aligned} \tag{6.13}$$

Since a is an arbitrary vector, (6.13) without $(a\cdot)$ should hold too. Thus, interchanging r and r', and using the reciprocity property of Green's function, it is obtained that

$$\begin{aligned}&\int_{V_1}\left\{-j\omega u_1 J_1 G_1 - \frac{\rho_1}{\varepsilon}\nabla G_1'\right\}dV' \\ &+\int_{S_1}\left\{-(\hat{n}'\times E_1)\nabla' G_1 - (\hat{n}\times E_1)\times\nabla' G_1 + j\omega u_1 G_1(\hat{n}'\times H_1)\right\}dS' = \begin{cases} E_1 & (r\in V_1) \\ 0 & (r\notin V_1)\end{cases}\end{aligned} \tag{6.14}$$

In (6.14), the differential element dv' and ds' are located at r', and ∇' is the gradient operator ∇ with respect to the primed coordination. Furthermore, $\hat{n}$, J_1, ρ_1 and H_1 are functions of r' . On the left-hand side, E_1 is a function of r', but on the right-hand side E_1 is a function of r.

Equation (6.14) is a general integral representation that expresses the electric field E in terms of the sum of a volume integral over the actual plate, and a surface integral over fields that can be a represented by an equivalent source on the surface of the plate. Thus, it can be concluded that the field inside a plate is determined by the actual volume source and equivalent surface source inside this plate.

The electric field E_2 in the domain 2 and E_3 in the domain 3 can also be derived by using the similar approach. In the domain 2, E_2 is given by following equation

$$\begin{aligned}&\int_{V_2}\left\{-j\omega u_2 J_2 G_2-\frac{\rho_2}{\varepsilon_2}\nabla G_2'\right\}dV\\&+\int_{S_2}\left\{-\left(\hat{n}'\times E_2\right)\nabla' G_2-\left(\hat{n}'\times E_2\right)\times\nabla' G_2+j\omega u_2 G_2\left(\hat{n}'\times H_2\right)\right\}dS=\begin{cases}E_2 & \left(r\in V_2\right)\\0 & \left(r\notin V_2\right)\end{cases}\end{aligned} \tag{6.15}$$

Since there is no volume current in the domain 3 and there is two surfaces enclosing this domain, E_3 is given by following equation

$$\begin{aligned}&\int_{S_1}\left(j\omega u_3 G_3\left(\hat{n}'\times H_3\right)-\left(\hat{n}'\times E_3\right)\times\nabla' G_3-\left(\hat{n}'\cdot E_3\right)\nabla' G_3\right)dS+\\&\int_{S_2}\left(j\omega u_3 G_3\left(\hat{n}'\times H_3\right)-\left(\hat{n}'\times E_3\right)\times\nabla' G_3-\left(\hat{n}'\cdot E_3\right)\nabla' G_3\right)dS=\begin{cases}E_3 & \left(r\in V_3\right)\\0 & \left(r\notin V_3\right)\end{cases}\end{aligned} \tag{6.16}$$

On two surfaces S_1 and S_2 which partitions the space into three domains, the following boundary conditions exist

$$\begin{aligned}&\text{on } S_1:\hat{n}\times E_3=\hat{n}\times E_1 \quad \hat{n}\cdot\varepsilon_3 E_3=\hat{n}\cdot\varepsilon_1 E_1 \quad \hat{n}\times H_3=\hat{n}\times H_1 \quad \hat{n}\cdot u_3 H_3=\hat{n}\cdot u_1 H_1\\&\text{on } S_2:\hat{n}\times E_3=\hat{n}\times E_2 \quad \hat{n}\cdot\varepsilon_3 E_3=\hat{n}\cdot\varepsilon_2 E_2 \quad \hat{n}\times H_3=\hat{n}\times H_2 \quad \hat{n}\cdot u_3 H_3=\hat{n}\cdot u_2 H_2\end{aligned}$$

If both two conductors are non-ferromagnetic conductors, there is relationship, as follows

$\varepsilon_3=\varepsilon_2=\varepsilon_1=\varepsilon$, $u_3=u_2=u_1=u$ and $G_1=G_2=G_3=G$

Thus there is

$$\hat{n}\cdot E_3 = \hat{n}\cdot E_1 \quad \hat{n}\cdot H_3 = \hat{n}\cdot H_1 \quad \hat{n}\cdot E_3 = \hat{n}\cdot E_2 \quad \hat{n}\cdot H_3 = \hat{n}\cdot H_2$$

With these boundary conditions, it is obtained from (6.15) and (6.16) that

$$\begin{aligned}&\int_{S_1}\left(j\omega uG\left(\hat{n}'\times H_1\right)-\left(\hat{n}'\times E_1\right)\times\nabla'G-\left(\hat{n}'\cdot E_1\right)\nabla'G\right)dS\\&=\int_{S_1}\left(j\omega uG\left(\hat{n}'\times H_3\right)-\left(\hat{n}'\times E_3\right)\times\nabla'G-\left(\hat{n}'\cdot E_3\right)\nabla'G\right)dS\end{aligned} \quad \text{on two sides of } S_1 \tag{6.17}$$

$$\begin{aligned}&\int_{S_2}\left(j\omega uG\left(\hat{n}'\times H_2\right)-\left(\hat{n}'\times E_2\right)\times\nabla'G-\left(\hat{n}'\cdot E_2\right)\nabla'G\right)dS\\&=\int_{S_2}\left(j\omega uG\left(\hat{n}'\times H_3\right)-\left(\hat{n}'\times E_3\right)\times\nabla'G-\left(\hat{n}'\cdot E_3\right)\nabla'G\right)dS\end{aligned} \quad \text{on two sides of } S_2 \tag{6.18}$$

From (6.15) and (6.15), it is known that when the observation point is located in the domain 1, both (6.15) and (6.16) are zeros. This means that the contribution of the domain 2 and the domain 3 to the electric field in the domain 1 is zero. Then the following relationship between the parameters in the domain 2 and the domain 3 is obtained

$$\begin{aligned}&\int_{S_1}\left(j\omega uG\left(\hat{n}'\times H_3\right)-\left(\hat{n}'\times E_3\right)\times\nabla'G-\left(\hat{n}'\cdot E_3\right)\nabla'G\right)dS\\&=-\int_{S_2}\left(j\omega uG\left(\hat{n}'\times H_3\right)-\left(\hat{n}'\times E_3\right)\times\nabla'G-\left(\hat{n}'\cdot E_3\right)\nabla'G\right)dS\end{aligned} \tag{6.19}$$

$$\begin{aligned}&\int_{S_2}\left(j\omega uG\left(\hat{n}'\times H_2\right)-\left(\hat{n}'\times E_2\right)\times\nabla'G-\left(\hat{n}'\cdot E_2\right)\nabla'G\right)dS\\&=-\int_{V_2}\left(-j\omega uJ_2G-\frac{\rho_2}{\varepsilon}\nabla'G\right)dV\end{aligned} \tag{6.20}$$

By substituting (6.19) and (6.20) into (6.14), it is obtained that

$$E_1=\int_{V_1}\left(-j\omega uJ_1G-\frac{\rho_1}{\varepsilon}\nabla'G\right)dV+\int_{V_2}\left(j\omega uJ_2G-\frac{\rho_2}{\varepsilon}\nabla'G\right)dV \quad \left(r\in V_1\right) \tag{6.21}$$

If there are more than two conductors in space, e.g. the number is N, (6.21) can be revised to (6.22) by using the similar procedure.

$$E_1 = \sum_{i=1}^{N} \int_{V_i} \left(-j\omega u J_i G - \frac{\rho_i}{\varepsilon} \nabla' G \right) dV \qquad (r \in V_1) \tag{6.22}$$

From (6.22), it is revealed that for non-ferromagnetic conductors in space, the electric field inside one conductor is contributed by the currents in all conductors. This can be considered as the linear superposition effect of these conductors. Equation (6.22) is also named as the electric field integral equation (EFIE).

If the current J_j inside conductor j is the source current, then the electric field component contributed by J_j is considered as the incident field E^i , (6.22) can be modified as

$$E_1 = \sum_{i=1, i \neq j}^{N} \int_{V_i} \left(-j\omega u J_i G - \frac{\rho_i}{\varepsilon} \nabla' G \right) dV + E^i \qquad (r \in V_1) \tag{6.23}$$

According to the Ohm's Law, the electric field inside the conductor 1 is represented by $E_1 = \frac{J_1}{\sigma}$ where σ is the conductivity of the conductor 1. Then (6.23) is further modified as

$$E^i = \frac{J_1}{\sigma} + \sum_{i=1}^{N} \int_{V_i} \left(j\omega u J_i G + \frac{\rho_i}{\varepsilon} \nabla' G \right) dV \qquad (r \in V_1) \tag{6.24}$$

Thus EFIE (6.22) is transformer to a representation associated with the current J , the charge ρ and incident field E^i .

6.2.2 Partial Element Equivalent Circuit Model of Plates

If the conductor 1 in Figure 6.1 is a non-ferromagnetic plates and the conductor carries the source current, (6.24) is simplified as

$$E^i = \frac{J_1}{\sigma} + \int_{V_1}\left(j\omega u J_1 G + \frac{\rho_1}{\varepsilon}\nabla' G \right) dV \qquad \left(r \in V_1 \right) \tag{6.25}$$

(6.25) is a vector equation. If it is assumed that the normal component of electric field on a plate is negligible, (6.25) can be divided into two scalar equations along two orthogonal coordinate axis.

$$E_x^i = \frac{J_x}{\sigma} + \int_V \left[j\omega u J_x G + \frac{\rho}{\varepsilon}\frac{\partial G}{\partial x} \right] dV \tag{6.26}$$

$$E_y^i = \frac{J_y}{\sigma} + \int_V \left[j\omega u J_y G + \frac{\rho}{\varepsilon}\frac{\partial G}{\partial y} \right] dV \tag{6.27}$$

Where E_x^i and J_x are respectively the x-component of incident electric field and current density at a position inside the plate. E_y^i and J_y are respectively the y-component of incident electric field and current density at a position inside the plate.

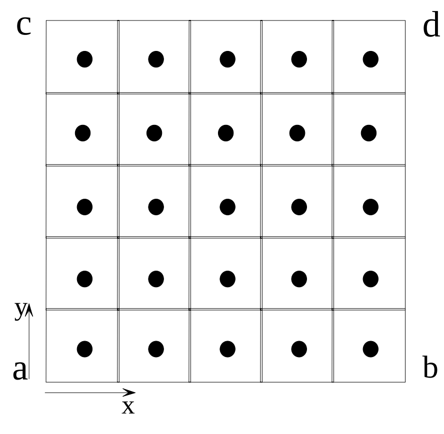

Figure 6.2 Voltage cells

Equation (6.27) and (6.28) describe the relationship between the incident electric field inside a plate and the volume current sources as well as the charge sources. To solve the fields numerically, this plate is divided into voltage cells along its length and width as Figure 6.2 shows. Between two adjacent voltage cells, a current cell is inserted. The current cell with x-direction current is named as an x-cell shown in Figure 6.3 (a), and the cell with y-direction current is named as a y-cell shown in Figure 6.3 (b). In order to take the radiation effect into account, the dimension of each cell should be much less than the wavelength of the incident field.

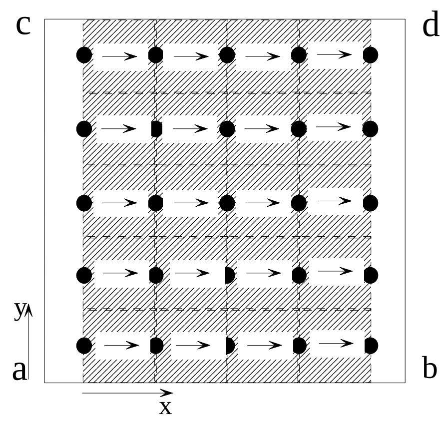

(a) Current x-cells

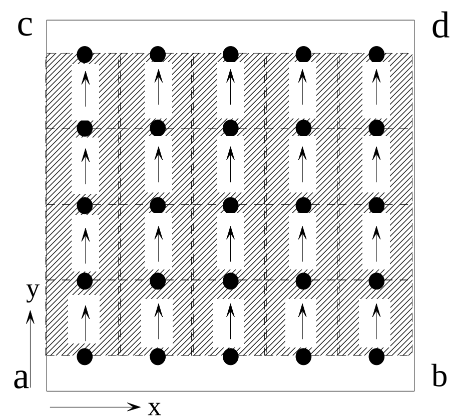

(b) Current y-cells

Figure 6.3 Two types of cells in the plate

It is assumed the charge density is uniform across each voltage cell and the current density is uniform across current x-cells and y-cells. The charges gather at the two end of a current cell. The partial differential ∇T is replaced by a difference expression $\left(T_i - T_j\right)/l$. Then for a combination of two voltage cells and a current cell (x-cell or y-cell) k as Figure 6.4 shows, (6.26) and (6.27) can be written as

$$E_k^i = \frac{J_k}{\sigma} + \frac{j\omega u}{4\pi}\sum_{n=1}^{N}\int_{V_n}\frac{J_n e^{-k_t|r_n - r_k|}}{|r_n - r_k|}dV + \frac{1}{4\pi\varepsilon l_{ij}}\left(\sum_{m=1}^{M}\int_{V_m}\frac{\rho_m e^{-k_t|r_n - r_k|}}{|r_m - r_i|}dV - \sum_{m=1}^{M}\int_{V_m}\frac{\rho_m e^{-k_t|r_n - r_k|}}{|r_m - r_j|}dV\right) \tag{6.28}$$

where $k = x$ or y and $k_t = \omega\sqrt{\mu\varepsilon}$.

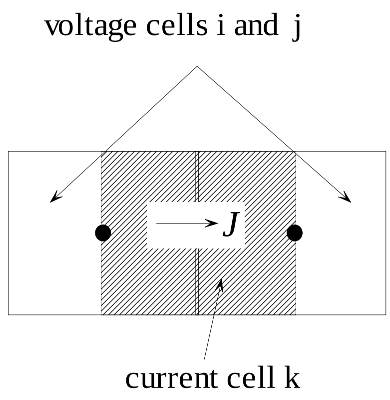

Figure 6.4 Combination of two voltage cells and one current cell

The size of the plate in a building is usually several tens meters, which is much smaller than the equivalent length about several hundreds meters of the maximum frequency to be considered in the lightning current spectrum. The radiation effect of the source can be neglected as $e^{-k_t|r-r'|} \approx 1$ in (6.28). Thus (6.28) can be simplified as

$$E_k^i = \frac{J_k}{\sigma} + \frac{j\omega u}{4\pi}\sum_{n=1}^{N}\int_{V_n}\frac{J_n}{|r_n - r_k|}dV + \frac{1}{4\pi\varepsilon l_{ij}}\left(\sum_{m=1}^{M}\int_{V_m}\frac{\rho_m}{|r_m - r_i|}dV - \sum_{m=1}^{M}\int_{V_m}\frac{\rho_m}{|r_m - r_j|}dV\right) \tag{6.29}$$

where l_{ij} is the distance between two voltage cells.

Integrating (6.29) on the a layer s_k inside the current cell, (6.29) is revised as

$$\frac{1}{w_k}\int_{S_k} E_k^i = \frac{1}{w_k}\int_{S_k} \frac{J_k(r,\omega)}{\sigma} + \frac{j\omega u}{4\pi w_k}\sum_{n=1}^{N}\int_{S_k}\int_{V_n} \frac{J_n(r',\omega)}{|r_n - r_k|} dSdV + \nabla U_k \tag{6.30}$$

where w_k is the width of the layer S_k.

∇U_k is defined as

$$\begin{aligned}\nabla U_k &= U_i - U_j \\ &= \frac{1}{4\pi\varepsilon S_i}\sum_{m=1}^{M}\int_{S_i}\int_{V_m} \frac{\rho_m}{|r_m - r_i|} dSdV - \frac{1}{4\pi\varepsilon S_j}\sum_{m=1}^{M}\int_{S_j}\int_{V_m} \frac{\rho_m}{|r_m - r_j|} dSdV\end{aligned} \tag{6.31}$$

where V_m is the volume of the voltage cell m. S_i and S_j are respectively the layer surface of the voltage cell i and j.

A. Extremely Low Frequency

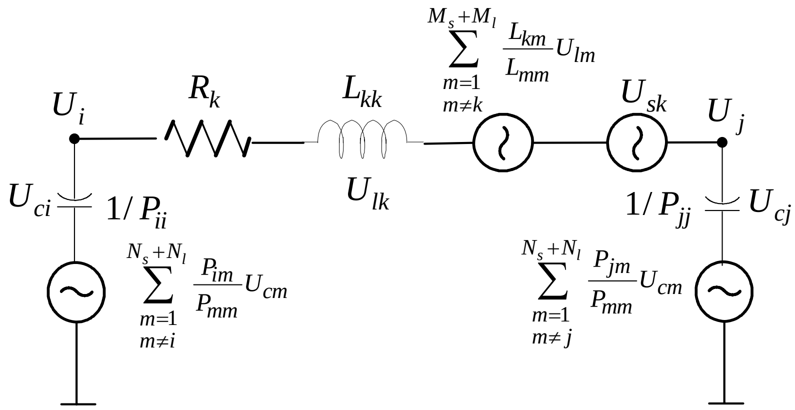

Figure 6.5 Partial element equivalent circuit of the combination

At extremely low frequency, the current density J and charge density ρ inside a plate can be considered to distribute uniformly along the plate thickness. Then they are both constant in each current cell and voltage cell. At this time, the current density J and charge density ρ can be extracted from integral signal in (6.31). Then (6.31) can be interpreted into the Kirchhoff's equation of partial element electric circuit (PEEC) as Figure 6.5 shows.

$$U_{sk} = R_k J_k + j\omega M_{kk} J_k + j\omega \sum_{n=1,k\neq n}^{N} M_{kn} J_n + U_i - U_j \tag{6.32}$$

and

$$U_i = U_{ci} + j\omega \sum_{j=1,j\neq i}^{M} \frac{P_{ji}}{P_{jj}} U_{cj} \tag{6.33}$$

$$U_{ci} = \frac{P_{ii}}{j\omega}\left(J_k - J_{k-1}\right) \tag{6.34}$$

where J_k is the volume current density inside cell k . U_i is the potential of the voltage cell i, i.e. one end of a current cell k . U_{sk} is the voltage imposed on the current cell k by the incident field. U_{ci} is the voltage of the partial capacitance connected at voltage cell i, as seen in Figure 6.5.

In (6.32) R_k is defined as the resistance of the current cell given by

$$R_k = \frac{l_k}{\sigma} \tag{6.35}$$

where l_k is the length of current cell k.

In (6.32) M_{kk} is defined as the self partial inductance and M_{kn} is the mutual partial inductance between current cells k and n. Since the item $e^{-k_t|r-r'|} \approx 1$ in extremely low frequency, a general formula for calculating partial inductance is given by

$$M_{kn} = \frac{u}{4\pi w_k} \int_{S_k} \int_{V_n} \frac{1}{|r_n - r_k|} dSdV \tag{6.36}$$

when n becomes k , (6.34) is for the self partial inductance.

In (6.33) and (6.34), P_{ii} is defined as the self partial potential coefficient and P_{ij} is the mutual partial potential coefficient between voltage cells i and j . A general formula for calculating potential coefficient is given by

$$P_{ij} = \frac{1}{4\pi\varepsilon S_i} \int_{S_i} \int_{V_j} \frac{1}{|r_j - r_i|} dSdV \tag{6.37}$$

when j becomes i , (6.37) is for calculating the self partial potential coefficient.

The explicit expressions of (6.36) and (6.37) are presented in Appendix A.

It is found that, the influence of the partial capacitance in the equivalent circuit is very small at the extremely low frequency. So it can be neglected in the calculation.

According to the current continuity law, the current flowing into a voltage cell is equal to the current flowing out. Since two x-cells and two y-cells are overlapped at a voltage cell, it is deemed that total current flowing inside is equal to the total current flowing outside. There is no normal current flowing in the plates and there is no displacement current either due to neglecting the partial capacitance. The continuity relation can be applied to the current density in the same level inside the plate.

$$\sum_{i=1}^{2} S_{xi} J_{xi} + \sum_{j=1}^{2} S_{yj} J_{yj} = 0 \tag{6.38}$$

Equation (6.29) can be interpreted into a circuit equation by defining the partial inductances and the partial potential coefficient, as shown in (6.31) and (6.32). Thus a current cell is transformed to a partial element equivalent circuit, as seen in Figure 6.5.

B. Full-wave Frequency

With increasing frequency, the distribution of current density J inside a plate becomes uneven due to the skin effect. At this time, it can not be considered as constant in each cell volume. It is reasonable to assume that the distribution along the thickness exhibits a double-exponent distribution characteristic given by

$$J\left(z\right)=J_1e^{-z/\tau}+J_2e^{-(d-z)/\tau} \tag{6.39}$$

where J_1 and J_2 are respectively the unknown current density on the two surface of a cell. d is the thickness of the plate. τ is the skin depth of the plate under the angular ω where $\tau=\sqrt{\omega u\sigma/2}$.

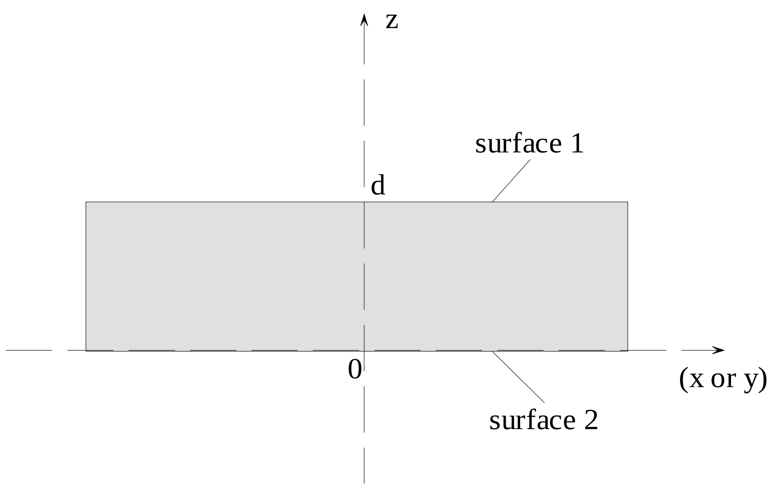

Figure 6.6 Two surfaces of a plate

Substituting (6.39) into (6.32), (6.32) is transformed into two Kirchhoff's circuit equations on two surfaces of a cell with the partial elements as seen in Figure 6.6.

$$U_{sk1} = R_k J_{k1} + j\omega M_{s1k} J_{k1} + j\omega M_{s2k} J_{k2} + j\omega \sum_{n=1,n\neq k}^{N} M_{s1n} J_{n1} + j\omega \sum_{n=1,n\neq k}^{N} M_{s2n} J_{n2} + U_i - U_j \quad \text{on surface 1} \tag{6.40}$$

$$U_{sk2} = R_k J_{k2} + j\omega M_{s2k} J_{k1} + j\omega M_{s1k} J_{k2} + j\omega \sum_{k=1,k\neq n}^{N} M_{s2n} J_{n1} + j\omega \sum_{n=1,n\neq k}^{N} M_{s1n} J_{n2} + U_i - U_j \quad \text{on surface 2} \tag{6.41}$$

where J_{k1} and J_{k2} are respectively the two parameters in (6.39) for the cell k. U_{sk1} and U_{sk2} are respectively the voltage induced by incident field on the surface 1 and the surface 2.

The partial inductance in (6.40) and (6.41) can be calculated by

$$M_{s1t} = \frac{u_0}{4\pi w_{s1}} \int_{S_1} \int_{V_t} \frac{e^{-z/\tau}}{|r_t - r_{s1}|} dSdV \tag{6.42}$$

$$M_{s2t} = \frac{u_0}{4\pi w_{s2}} \int_{S_2} \int_{V_t} \frac{e^{-(d-z)/\tau}}{|r_t - r_{s2}|} dSdV \tag{6.43}$$

where w is the width of two surfaces and $t = i \ or \ j$.

It is assumed that the charge distribution does not vary with frequency across the thickness of a plate in the lightning frequency spectrum. The partial capacitance in the equivalent circuit can be obtained by calculating the partial potential coefficient between voltage cells i and j with the following equation

$$P_{ij} = \frac{1}{4\pi\varepsilon_0 S_i} \int_{S_i} \int_{V_j} \frac{1}{|r_j - r_i|} dSdV \tag{6.44}$$

where S_i is the surface of the middle layer inside a voltage cell i.

The explicit expressions of (6.42), (6.43) and (6.44) are presented in Appendix B.

According to the current continuity law, the current flowing into a voltage cell is equal to the current flowing out as seen in Figure 6.4. Since two x-cells and two y-cells are overlapped at a voltage cell, it is considered that total current gathering at a voltage cell is equal to zero.

$$\sum_{i=1}^{2} I_{xi} + \sum_{j=1}^{2} I_{yj} = I_c \tag{6.45}$$

where I_{xi} is the current flowing in x-cell i and I_{yi} is the current flowing in y-cell i. I_c is the displacement current between voltage cells.

Both I_{xi} and I_{yi} can be represented by the integration of current density as follows

$$I_{ti} = w_{ti} \int_0^d J_{ti}(z,\omega) dz \tag{6.46}$$

where $t = x$ or y. w and d are receptively the width and thickness of the cell i.

6.2.3 Solution Procedure

In above section, the KVL equation (6.32) and KCL equation (6.38) are built at extremely low frequency. The KVL equation (6.40), (6.41) and KCL equation (6.45) of a plate are built for full-wave frequency. Applying the KVL and KCL equations to all current cells and voltage cells in this plate, a group of KVL equations and KCL equations are obtained, which can be written in the form of matrix equation in the frequency domain, as follows

$$\begin{bmatrix} A & Y \\ Z & G \end{bmatrix} \begin{bmatrix} \dot{I}_b \\ \dot{V}_s \end{bmatrix} = \begin{bmatrix} \dot{I}_s \\ 0 \end{bmatrix} \tag{6.47}$$

where A is the node relationship matrix; Y is the susceptance matrix; Z is the impedance matrix; G is the branch relationship matrix; I_b is the current density vector and V_s is the potential scalar. I_s is the source current vector.

By solving the matrix equation, the current density in each current cell is obtained. The current cell is further divided into small rectangles along the current direction, each of which is treated as a filament. The magnetic fields around the plate generated by each filament are calculated by (3.47) in Chapter 3 according to the Bio-savart Law. The total magnetic fields are obtained by superposing the magnetic fields generated from all these filaments.

If the source is a transient current, such as a lightning discharge current, the transient source current in the time domain firstly is transformed to a series of a.c harmonic source current by the Fourier transform technique. Then the solution procedure is applied to calculate the current distribution and magnetic field at each harmonic frequency. Finally, the results obtained from all discrete frequencies are transformed to the time domain by the inverse Fourier transform technique.

6.3 Summary

This chapter provided the partial element equivalent circuit (PEEC) approach for modeling non-ferromagnetic plates at both extremely low frequency and full-wave frequency. With this modeling approach, the current flowing in a plate was discomposed into two orthogonal components which exist at corresponding current cells. Then a numerical procedure was applicable to transform the plate into an equivalent circuit network. Meanwhile, uneven current distribution inside plates was taken into consideration. With the solution procedure in the frequency domain, the current distribution and magnetic fields are calculated both for an a.c. source or a transient source.

Chapter 7

Modeling Approach of Wire-plate Building Structures

7.1 Introduction

In Chapter 6, the partial element equivalent circuit (PEEC) approach was developed to model a large non-ferromagnetic plate. With this approach, the magnetic fields around a plate can be evaluated numerically under the excitation of an a.c. or transient current source.

In a modern building, large metal plates such as those used for floor decking are usually connected with columns and beams. Since the reinforcing concrete (RC) bar bundles can be modeled as cylindrical conductors as stated in Chapter 3, the plates and those cylindrical conductors form a building structure, which can be modeled as a wire-plate structure. The PEEC modeling approach can be applied to this type of building structures by integrating the PEEC model of plates and the equivalent circuit (EC) model of cylindrical conductors. This integrated model of the wire-plate building structure requires a large amount of memory and costs a long time for solution if the structure has a large dimension. Under the condition of a direct lightning stroke, a hybrid analytical-numerical equivalent circuit (HANEC) modeling technique is developed from the integration of the PEEC and the EC modeling approach.

In this chapter, a building structure with metal decking is introduced firstly. The PEEC model of plates and the EC model of cylindrical conductors are integrated to a model of the building structure with metal decking. A preliminary study is conducted on a scaled wire-plate structure under a direct lightning stoke. From the results of the preliminary study, some valuable observations are obtained. With these observations, a new modeling technique, the hybrid analytical-numerical equivalent circuit (HANEC) technique, is proposed finally.

7.2 Simplification of a Building Structure with Decking

In modern buildings, metal decking is increasingly applied for the construction of floors. The decking is usually bonded with the RC bars inside columns, beams the other structural components. Since the RC bars inside those components can be considered as wire-like cylindrical conductors as stated in Chapter 3, the building structure containing RC bars and decking can be simplified to a wire-plate structure, as shown in Figure 7.1.

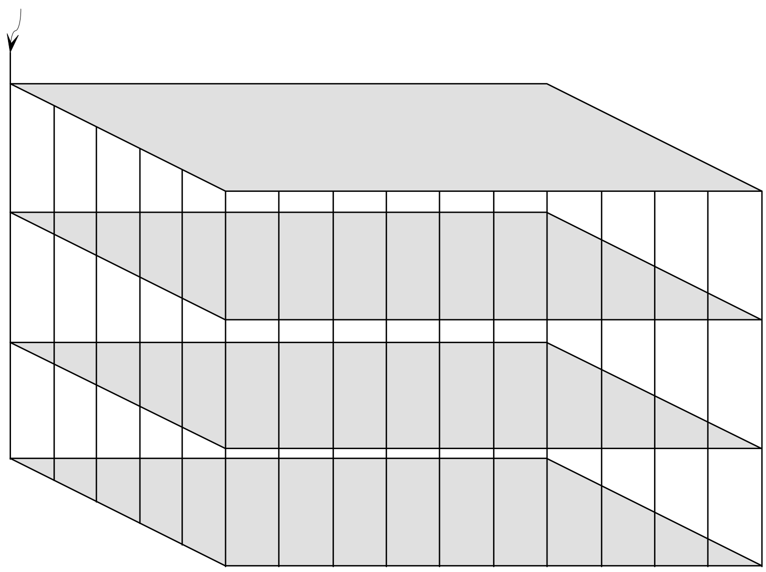

Figure 7.1 A wire-plate building structure under a direct lightning stroke

7.3 Integration of PEEC Model of Plates and EC Model of Cylinderical Conductors

The PEEC approach was proposed in Chapter 6 for modeling a plate, and the EC approach was proposed in Chapter 3 for modeling cylindrical conductors. Since two modeling approaches are both based on the electric circuit theory, they can be integrated by following procedure:

1) When generating cells in plates, the joint position of a wire and a plate is located at the center of a voltage cell. This joint also is a joint of x and y current cells in the plate, as shown in Figure 7.2.

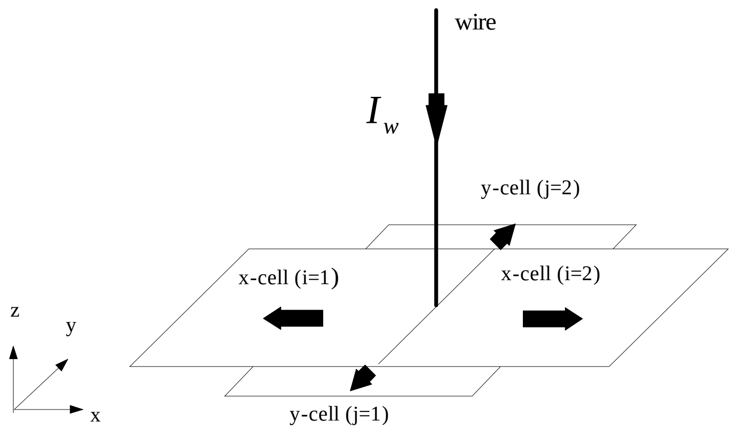

Figure 7.2 Joint of a wire and a plate

2) Set the node voltage of a wire at the joint to be equal to the voltage at the voltage cell where the joint is located. The current conservation law is applied at the joint. So the current in the wire is equal to the sum of the current in the current cells connected at the joint. Since the current has an approximate double exponential distribution inside a plate as described in (6.39), the Kirchhoff's Current Law (KCL) equation at the joint is expressed by

$$I = \sum_{i=1}^{2} w_{xi} \int_0^d \left(J_{xi,1} e^{-\frac{z}{\tau}} + J_{xi,2} e^{-\frac{d-z}{\tau}} \right) dz + \sum_{j=1}^{2} w_{yj} \int_0^d \left(J_{yj,1} e^{-\frac{z}{\tau}} + J_{yj,2} e^{-\frac{d-z}{\tau}} \right) dz \qquad (7.1)$$

where I is the current in the wire, d is the thickness of the plate, and w_i is the width of the cell i.

3) With these additional KVL and KCL equations, the EC model of the wire and the PEEC model of the plate are combined to an integrated equivalent circuit network. Since there is no mutual inductance between orthogonal conductors according to Neumann's theory [Andre et.al., 2001], there is no mutual inductance between the wire and current cells in the plate while there is mutual capacitance between them.

4) By solving the KVL and KCL equations of the equivalent circuit network of a wire-plate structure, the current in the wire and current density inside the plate can be evaluated numerically. Consequently, the magnetic field can be evaluated by the Bio-savart law as stated in Chapter 6.

7.4 Priliminary Study

With the integrated modeling approach, a preliminary study was conducted on a simple and small scale wire-plate model, as shown Figure 7.3. In this model, two aluminum plates with the thickness of 1.5mm were connected with four aluminum cylindrical conductors. An a.c. current source was connected at two terminals of a conductor.

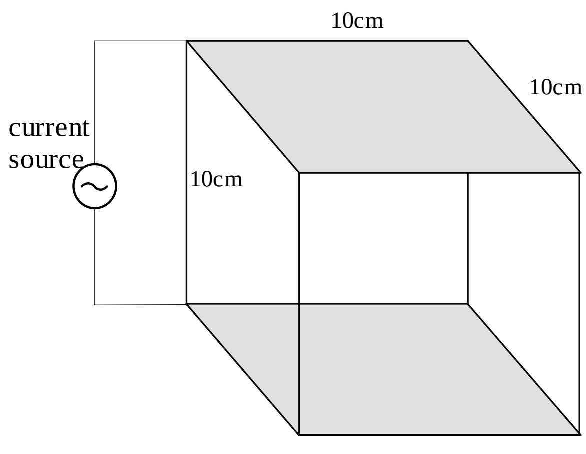

Figure 7.3 A small scale wire-plate model

This wire-plate model was transformed to an equivalent circuit network by integrating the model of plates and cylindrical conductors. The current distribution in the plates is evaluated at harmonic frequencies ranging from extremely low frequency to high frequency. From the evaluation results, some observations were found and presented, as follows

1) With increasing frequency, the required number of cells on the plates will increased rapidly to ensure the evaluation accuracy. Consequently, the requirement of the memory capacity and calculation time will increase significantly.

2) The proximity effect between two parallel plates is very small when the source current flows through the plates directly. So the current distribution inside a plate along the normal direction is nearly symmetrical. Then the double exponential function (6.39) which is used to approximate the current distribution can be replaced with a hyperbolic function.

$$J(z) = J\cosh\left(-\frac{z}{\tau}\right) \quad z \in \left[-\frac{d}{2}, \frac{d}{2}\right] \tag{7.2}$$

where J is a unknown variable, d is the thickness of the plate, and τ is the skin depth of the plate under the angular ω where $\tau = \sqrt{\omega u \sigma / 2}$.

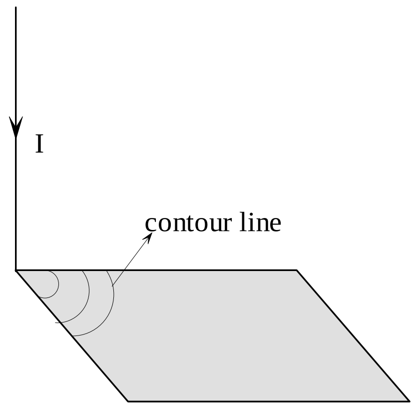

(a) at low frequency

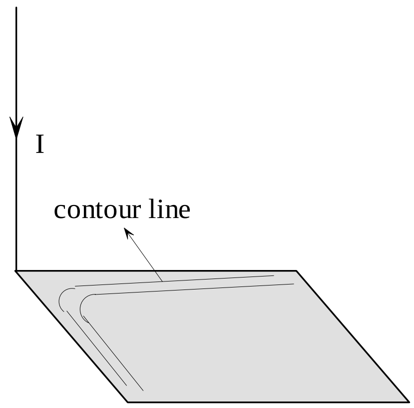

(b) at high frequency

Figure 7.4 Contour lines of current density on a plate around a joint

3) The variation of the current distribution along the tangential direction with frequency inside the area around a joint shows inherent patterns. At low frequencies, the current diverges evenly from the joint as seen in Figure 7.4(a). With increasing frequency, the current will gather at the area near the edges of the plates as Figure 7.4(b) shows.

4) The susceptance on the wire-plate model has little influence on the current distribution from the extremely low frequency to the frequency as high as 1MHz which is about the dominant frequency spectrum of lightning discharge

current. For the lightning discharge current source, the susceptance of the wire-plate model can be neglected.

7.5 Hybrid Analytical-Numerical Equivalent Cirucit Technique

With the observations from the preliminary study, following modifications in the modeling approach were proposed in order to reduce the requirement of memory and accelerate solution for a wire-plate structure under a direct lightning stroke.

7.5.1 Uneven Cell Generation Method

In the EC modeling method, the current cells and voltage cells were generated evenly in both tangential directions. In each current cell, the assumption was adopted that the current density on each cells is uniform. From the preliminary study, it was found that with increasing frequency, the current distribution on the plate became uneven. The current density on the center area of a plate became small. On the contrary, the current density in the area around the wire-plate joint and near the boundary became large. In another word, the gradient of current density in these areas increased significantly with increasing frequency. At this time, a large number of even cells were required to ensure the evaluation accuracy.

In order to decrease the cell number, uneven cells generation method is proposed in this section. Usually, uneven cells are generated by dividing the plate unevenly into small voltage cells with different sizes on the plate directly. With this method, the inductance between every two cells in the same direction should be calculated. Assuming the cell number is N×M, the number of inductance to be calculated may be $(N\times M)^2$. From Section 6.2, it is known that there are 5 folds of numerical integration in calculating each partial inductance. When the cell number is large, calculating all the mutual inductance is quite time-consuming. In this thesis, a novel uneven cell generation method is proposed to reduce the computation time of inductance.

Step 1: Locating Voltage Cells

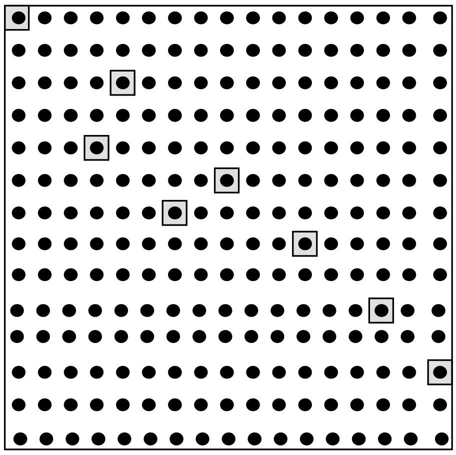

Figure 7.5 Center points of voltage cells

Firstly, a plate in the wire-plate structure is divided into a lot of identical small voltage cells. In Figure 7.5, the grey squares represent some of voltage cells and the black points represent the centers of voltage cells. Since each voltage cell is the same in size, the current cells generated from voltage cells are also identical. Thus, the mutual inductances between one cell and the others include all the values of the mutual inductance between any two cells. For example, the number of identical current cells is N×M. Then only N×M inductance should be calculated which holds all the value of inductance for N×M cells, unlike $(N\times M)^2$ in other grid generation methods.

Step 2: Rarefaction of Voltage Cells

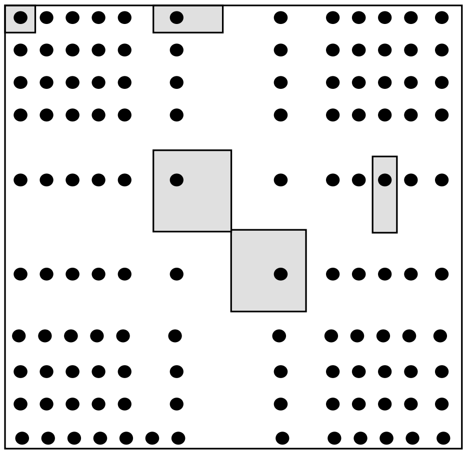

Figure 7.6 Rarefaction of voltage cells

On the plate with even voltage cells, some of voltage cells can be combined into one bigger cell if potential on these cells changes slightly, as illustrated in Figure 7.6. The rarefaction rules obtained from the preliminary study are stated, as follows:

1) In the area away from the wire-plate joints, a large number of voltage cells can be combined into a large cell since the current density in this area changes slightly.

2) When the area moves towards to the joint, the number of cells to be combined gets smaller and smaller.

3) In the area close to a joint no change of voltage cell size is recommended.

Step 3: Generation of Current Cells

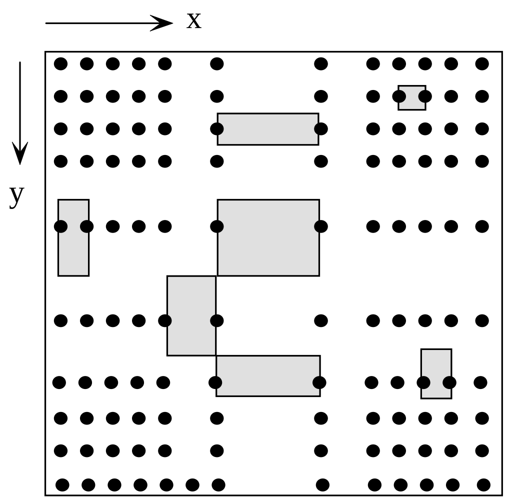

(a) x-cells

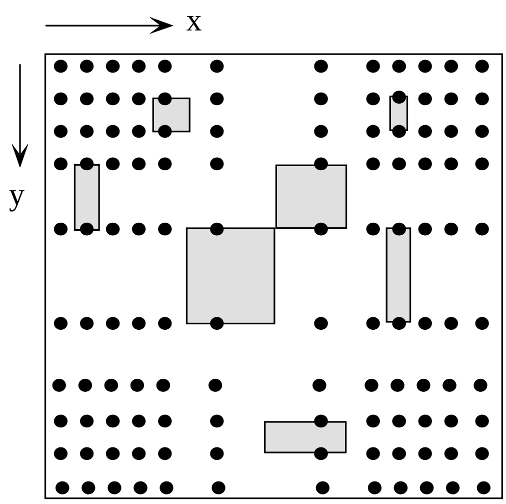

(b) y-cells

Figure 7.7 Uneven current cells generated from simplified voltage cells

Current cells in both x and y directions are generated individually from the revised voltage cells. Figure 7.7 illustrates some generated x-cells and y-cells with different shapes. Since one combined current cell contains several original current cells generated in Step 1, the inductance of this bigger cell is obtained from the calculated inductances of those original current cells through a combination procedure. This procedure is superior to calculating the mutual inductance of uneven current cells directly in terms of the memory requirement and CPU time.

Step 4: Combination Procedure for Calculating Inductance

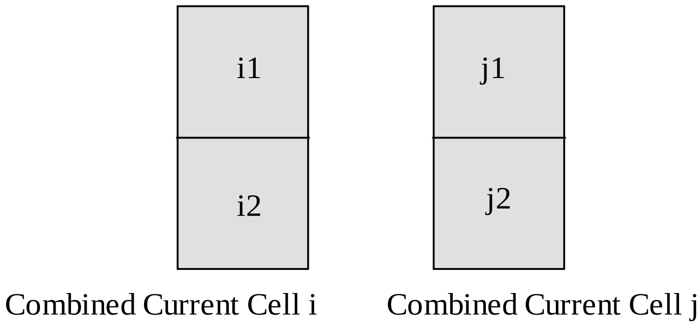

Figure 7.8 Two combined current cells

The combination procedure is introduced via the example given below. Figure 7.8 shows two combined current cells. Cell i contains two original current cells i_1 and i_2. Cell j contained two original current cells j_1 and j_2.

The inductance matrix of the original cells i_1, i_2, j_1 and j_2 is obtained from the calculation in Step 1, and is given by

$$L_{ij} = \begin{bmatrix} L_{i1i1} & L_{i1i2} & L_{i1j1} & L_{i1j2} \\ L_{i2i1} & L_{i2i2} & L_{i2j1} & L_{i2j2} \\ L_{j1i1} & L_{j1i2} & L_{j1j1} & L_{j1j2} \\ L_{j2i1} & L_{j2i2} & L_{j2j1} & L_{j2j2} \end{bmatrix} \tag{7.3}$$

Then the self inductance of the combined Cell i is as follows

$$L_{ii} = L_{i1i1} + L_{i2i2} + L_{i1i2} + L_{i2i1} \tag{7.4}$$

The self inductance of the combined Cell j is as follows

$$L_{jj} = L_{j1j1} + L_{j2j2} + L_{j1j2} + L_{j2j1} \quad (7.5)$$

The mutual inductance between Cell i and Cell j is as follows

$$L_{ij} = L_{i1j1} + L_{i2j1} + L_{i1j2} + L_{i2j2} \quad (7.6)$$

From (7.4) and (7.5), it shows that the self inductance of a combined cell is the sum of all the self inductance of its original cells and the mutual inductance between its original cells. It should be emphasized that the mutual inductance between Cell i_1 and Cell i_2 and that between Cell i_2 and Cell i_1 are considered two individual mutual inductances in calculation, although they are identical in fact.

From (7.6), it shows that the mutual inductance between combined cells is the sum of all the mutual inductance between their original cells. Similarly, the mutual inductance between Cell i_1 and Cell j_2 and that between Cell j_2 and Cell i_1 are considered two individual mutual inductances in calculation, although they are identical in fact.

7.5.2 Symmetrical Current Distribution inside Plates

From preliminary study, it is found that the eddy current generated from the induction effect between two plates is much smaller than the shunt current from the lightning discharge current. Then the proximity effect can be neglected. At this time, the current density inside a plate can be approximated by a double exponential equation as shown in (7.2).

With (6.39), the number of unknown variables in each cell is reduced from 2 to 1. Thus, (6.40) and (6.41) in Section 6.2 is modified to be

$$U_{si} = R_i J_i + j\omega M_{ii} J_i + j\omega u \sum_{j=1, j\neq i}^{N} M_{ij} J_j + U_n - U_m \tag{7.7}$$

where J_i is the current density at the middle level of Cell i. U_n is the voltage of the voltage cell n, i.e. one end of a current cell i. U_{si} is the voltage imposed on the current cell i. M_{ii} is the partial inductance between the middle level and the volume of Cell i. M_{ij} is the mutual partial inductance between the middle level of Cell i and the volume of Cell j.

The formula of inductance M_{ii} is given by

$$M_{ii} = \frac{u_0}{4\pi w_i} \int_{S_i} \int_{V_i} \frac{\cosh\left(-\frac{z}{\tau}\right)}{\left|r_i - r_i'\right|} dSdV \tag{7.8}$$

$$M_{ij} = \frac{u_0}{4\pi w_i} \int_{S_i} \int_{V_j} \frac{\cosh\left(-\frac{z}{\tau}\right)}{\left|r_j - r_i\right|} dSdV \tag{7.9}$$

The explicit expressions of (7.8) and (7.9) can be obtained with the results presented in Appendix B.

7.5.3 Analytical Expression of Current Distribution around a Wire-plate Joint

The current density gradient around a wire-plate joint increases significantly with increasing frequency. Thus at high frequency the size of the cells in these areas should be extremely small to meet the assumption of uniform current density. This will result in a large memory capacity required and make the solution unachievable. In order to solve this problem, an analytical function is developed for preliminary study to describe the current distribution around a wire-plate joint.

7.5.3.1 Current Distribution around a Wire-Plate Joint

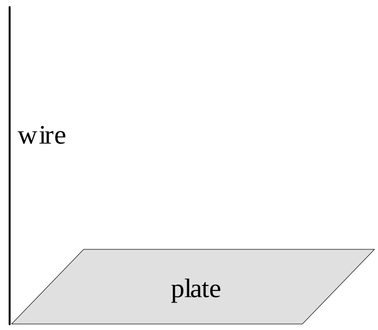

(1) at a corner of the plate

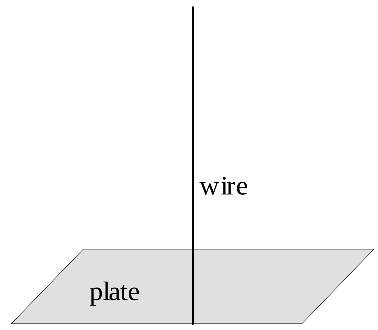

(2) at the side of the plate

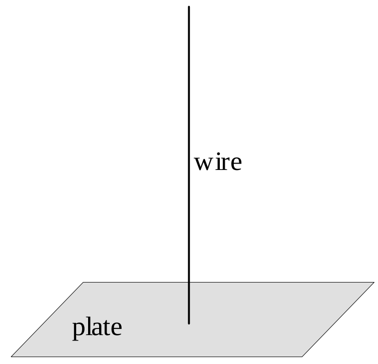

(3) inside the plate.

Figure 7.9 Joint of a wire and a plate

The wire-plate joint inside a plate can be divided into three types as shown in Figure 7.9. Type (1) joint is considered as a wire connected with a sector of 90 degree. Type (2) joint is considered as a wire connected with a sector of 180 degree. Type (3) joint is considered as a wire standing in the middle area of a plate.

Assuming the current is injected from the wire into the plate, the current will defuse outward inside the plate from the joint. If the current distribution along the radial direction and circumferential direction can be represented with an analytical function, the discretization in the area will be not necessary any more.

For Type (3) joint, because the area around the joint is axial symmetric, it is obvious that the current is distributed uniformly along the circumferential direction around the joint. For Type (1) and (2) joints, the current distribution along the circumferential direction should be derived by using the conformal mapping technique.

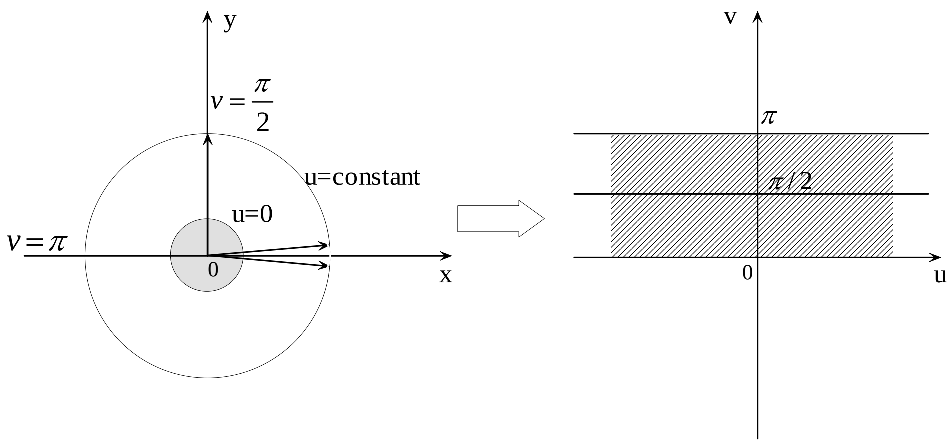

Figure 7.10 Conformal mapping from a sector to a rectangle

As Figure 7.10 shows, a sector with any degree can be conformal mapped to a 2-D rectangle with the transformation function [Binns et.al., 1992]

$$\begin{cases} \sqrt{x^2+y^2} = e^u \\ \tan^{-1}\left(\dfrac{y}{x}\right) = v \end{cases} \tag{7.10}$$

From the conformal mapping function, it is shown that the radius of the sector in xy plane is mapped to the u coordinate in uv plane. The angle of the sector is mapped to the v coordinate in uv plane. Then Type (1) joint is mapped to a rectangle with coordinate $v = \dfrac{\pi}{2}$; Type (2) joint is mapped to a rectangle with coordinate $v = \pi$. Thus, if the current distribution in the rectangle along v coordinates in uv plane is revealed, the distribution in the sector can also be obtained consequently.

7.5.3.2 Current Distribution in 2D Rectangle Plate

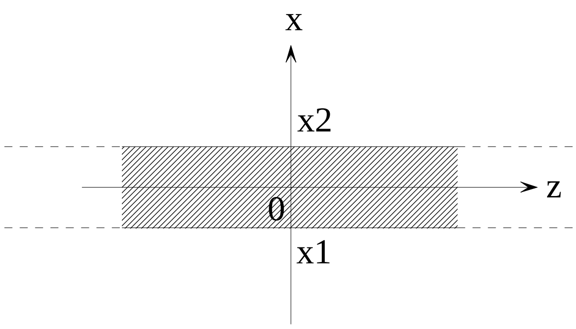

Figure 7.11 A 2D rectangle plate

The current distribution along the z direction in a 2D rectangle plate shown in Figure 7.11 can be derived by the following procedure.

The Maxwell equations in metal plate are given by

$$\begin{cases} \nabla \times H = (\sigma + j\omega\varepsilon) E \\ \nabla \times E = -j\omega u H \\ \nabla \cdot H = 0 \\ \nabla \cdot E = 0 \end{cases} \tag{7.10}$$

The electric field E inside the plate is expressed in terms of the scalar electric potential Φ and vector magnetic potential A, as follows

$$E = -j\omega A + \nabla\Phi \tag{7.11}$$

The current density J inside the plate is given by

$$J = -j\omega\sigma A + \sigma\nabla\Phi \tag{7.12}$$

In the 2-D infinite long plate shown in Figure 7.11, E, J and A have the z-direction component only. Equation (7.12) can be rewritten, as follows

$$J_z = -j\omega\sigma A_z + \sigma \frac{\partial\Phi}{\partial z} \tag{7.13}$$

From (7.13), it is noted that the current inside the plate not only depends on the scalar electric potential variation in space, but also the vector magnetic potential in time. In our discussion, $\frac{\partial\Phi}{\partial z}$ is a constant.

Since the vector potential A can be derived from the D'Alembert Equation

$$\nabla^2 A_z + \omega^2 u\varepsilon A_z^2 = -uJ_z \tag{7.14}$$

The solution of A_z on the plate is given by

$$A_z(x,z) = \frac{u}{4\pi} \int_{x_1}^{x_2} \int_{-\infty}^{+\infty} \frac{J_z(x') e^{-j\omega\sqrt{u\varepsilon}r}}{r} dx' dz' \tag{7.15}$$

where $r=\sqrt{(x-x')^2+(z-z')^2}$

Since A_z is symmetrical with respect to the axis z=0 and A_z is uniform at any z coordinate along the z axis, (7.15) can be modified to be

$$A_z(x)=\frac{u}{2\pi}\int_{x_1}^{x_2}\int_{0}^{+\infty}\frac{J_z(x')e^{-j\omega\sqrt{u\varepsilon}r}}{r}dx'dz' \tag{7.16}$$

where $r=\sqrt{(x-x')^2+z'^2}$

By substituting (7.16) into (7.13),

$$J_z(x)+j\omega\sigma\frac{u}{2\pi}\int_{x_1}^{x_2}\int_{0}^{+\infty}\frac{J_z(x')e^{-j\omega\sqrt{u\varepsilon}r}}{r}dx'dz'=\sigma\frac{\partial\Phi}{\partial z} \tag{7.17}$$

where $r=\sqrt{(x-x')^2+z'^2}$

Equation (7.17) is the second kind of Fredholm Integral Equation. This kind of equation can be solved numerically by the moment method.

7.5.3.3 Integration of Sector Area and Cell Area

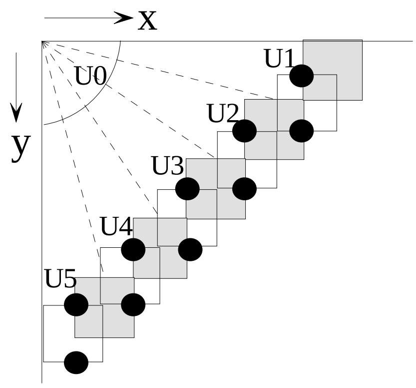

Figure 7.12 Boundary between analytical area and cell area

The area around a wire-plate joint is considered as an independent region with one analytical equation for describing the current distribution. The coupling between this region and other current cells on the plate should be considered.

Figure 7.12 shows an analytical region around a joint and its adjacent rectangle current cells. The grey cells represent 5 x-cells and the white cells represent 5 y-cells. The voltage of an arc with radius r_1 around the joint is assumed as U_0.

The analytical region is divided into several small regions between two dotted lines shown in Figure 7.12. The current density on each small region is assumed constant along the circular direction which is determined from the distribution equation. The current density decreases along the radial direction according to current conservation law by combining with (7.2)

$$J_i(r,z) = J_{arc-i}\frac{R_{acr-i}}{r}\cosh\left(-\frac{z}{\tau}\right) \qquad z\in\left[-\frac{d}{2},\frac{d}{2}\right] \tag{7.18}$$

where J_{arc-i} is the current density at arc of region i (i=1,2,..,5) and R_{arc-i} is the radius of arc i. J_i is the current density at a point inside region i with radius r to the joint.

The voltage difference between the arc and point n satisfies the KVL equation

$$U_n - U_0 = \underbrace{\frac{\int_l J_i(r,0)\,dr}{\sigma}}_{\text{resistance}} + \underbrace{\frac{j\omega}{4\pi w_n}\int_{S_n}\int_{V_k}\frac{J_i(r,z)\,dSdV}{|r_k - r_n|}}_{\text{self inductance}} + \underbrace{\frac{j\omega}{4\pi w_n}\sum_{t=1,t\neq i}^{T}\int_{S_n}\int_{V_t}\frac{J_t(r,z)\,dSdV}{|r_t - r_n|}}_{\text{mutual inductance between small regions}}$$
$$+\underbrace{\frac{j\omega}{4\pi w_n}\sum_{j=1,j\neq i}^{N}\int_{S_n}\int_{V_j}\frac{J_j(z)\,dSdV}{|r_j - r_n|}}_{\text{mutual inductance between the region and cells}} - U_{si} \tag{7.19}$$

where U_0 and U_n are respectively the voltage at arc 1 and point n. $J_t(r,z)$ is the current density inside region t. $J_j(z)$ is the current density inside other regions or current cells. S_n is the layer at the middle of region . V_i is the volume of region i.

In (7.19), the first item at the right side represents the resistance component of KVL. The second item represents the self inductance component and the third item represents the mutual inductance between the region i and other regions or current cells. The last item U_{si} is the induced voltage at the region i from the incident field. By substituting (7.18) and (7.2) into (7.19), (7.19) is transformed into a concise equation, as follows

$$U_n - U_0 = R_i J_{arc-i} + j\omega \sum_{t=1}^{T} M_{it} J_{arc-t} + j\omega \sum_{j=1, j\neq i}^{N} M_{ij} J_j - U_{si} \tag{7.20}$$

where

$$R_i = \frac{R_{acr-i} \ln\left(\frac{R_i}{R_{acr-i}}\right)}{\sigma} J_{arc-i} \tag{7.21}$$

$$M_{it} = \frac{u_0}{4\pi w_i} \int_{S_i} \int_{V_t} \frac{R_{arc-t}}{r_t} \frac{\cosh\left(-\frac{z}{\tau}\right)}{|r_t - r_i|} dSdV \tag{7.22}$$

$$M_{ij} = \frac{u_0}{4\pi w_i} \int_{S_i} \int_{V_j} \frac{\cosh\left(-\frac{z}{\tau}\right)}{|r_j - r_i|} dSdV \tag{7.23}$$

where V_t is the volume of the analytical region t, and R is an integral variable from R_t to the adjacent rectangle voltage center along the radial direction from the joint.

The explicit expressions of (7.22) and (7.23) can be obtained by replacing $e^{-K_2 z}$ with $\cosh\left(-\frac{z}{\tau}\right)$ in Appendix B.

The KCL equation established at the center of a voltage cell is given by

$$J_t \theta_t R_t \int_{-d/2}^{d/2} \cosh\left(-\frac{z}{\tau}\right) dz + J_{xn} d\Delta x + J_{yn} d\Delta y = 0 \tag{7.24}$$

where θ is the angle of the analytical region t. d is the thickness of the plate. Δx and Δy are respectively the lengths of the side orthogonal to the current direction.

7.5.4 Integrating Models of Wire and Plate

In Section 1.2, the EC model of cylindrical conductors and the PEEC model of plates are integrated to transform a wire-plate model of building structure into an equivalent circuit network. When the HANEC technique applied, the integration of two kinds of models will be modified, as follows.

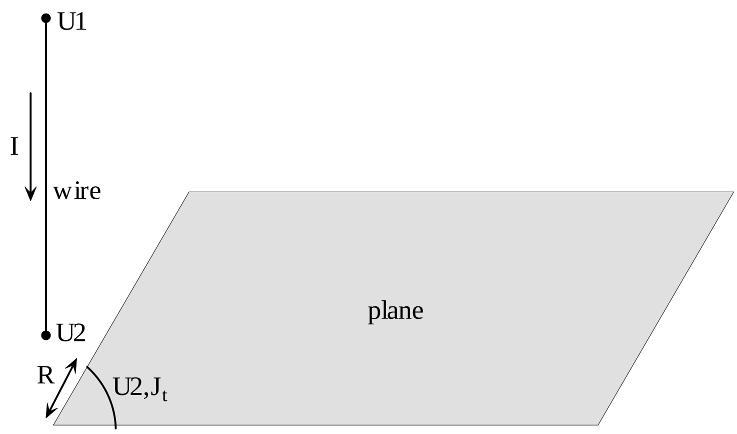

Figure 7.13 Integration the models of a cylindrical conductor and a plate

As Figure 7.13 shows, the voltage difference between the two terminals of a wire conductor are U_1 and U_2. When the wire is connected with the plate at a corner, it is assumed that the voltage at the arc around the joint is equal to U_2. Furthermore, the total current flowing outward through the arc section is supposed to be equal to the current in the wire conductor as (7.25) reveals.

$$I = \sum_{t=1}^{T} \int_{-\frac{d}{2}}^{\frac{d}{2}} J_{arc-t} R_{arc-t} \theta_{arc-t} \cosh\left(-\frac{z}{\tau}\right) dz \tag{7.25}$$

where I is the current in the conductor. d is the thickness of the plate. T is the number of current cells connected at the joint. J_{arc-t} is the current density at the arc. R_{arc-t} and θ_{arc-t} are respectively the radius and angle of the arc.

With these two boundary conditions, the EC models of cylindrical conductors can be integrated with the HANEC model of the plate network and finally form an equivalent electric network for the wire-plate model of building structure.

7.5.5 Simplification of Coefficient Matrix and Solution Procedure

For the complete equivalent circuit network built in Section 7.5, the current distribution in the wire conductors and on plates can be calculation with the similar solution procedure stated in Section 6.2.2.

The matrix equation of this equivalent circuit network is given by

$$\begin{bmatrix} A & 0 \\ Z & G \end{bmatrix} \begin{bmatrix} \dot{I}_b \\ \dot{V}_s \end{bmatrix} = \begin{bmatrix} \dot{I}_s \\ 0 \end{bmatrix} \tag{7.26}$$

where A and G are respectively the node relationship matrix and the branch relationship matrix I_b is the current and current density vector and V_s is the voltage scalar. I_s is the source current vector; Z is the impedance matrix which has a structure like follows

$$Z = \begin{bmatrix} Z_{wires} & 0 \\ 0 & Z_{plates} \end{bmatrix} \tag{7.27}$$

where Z_{wires} is the inductance matrix of wire conductors and Z_{plates} is the inductance matrix of plates. According to the observation (2) of the preliminary study, the proximity effect of two plates can be neglected. Then the mutual impedance between two plates can be considered as zero. Then the impedance matrix of plates has following structure

$$Z_{plates} = \begin{bmatrix} Z_{plate1} & 0 & 0 & \cdots \\ 0 & Z_{plate2} & 0 & \cdots \\ 0 & 0 & Z_{plate3} & \cdots \\ \vdots & \vdots & \vdots & \ddots \end{bmatrix} \tag{7.28}$$

where $Z_{platei}\left(i = 1, 2, 3, \ldots\right)$ is the inductance matrix of a single plate.

Since most of the elements in A and G are zero, (7.28) becomes a sparse matrix equation which can be solved by the solution technique of sparse matrix equation.

By solving the matrix equation, the current in wire conductors and current density in plates are obtained. The magnetic field generated by wire conductors can be calculated by (3.47) directly. The magnetic field generated by plates can be computed with the same method introduced in Section 6.2.2. Then the magnetic fields around the wire-plate structure are obtained according to the superposition theorem.

The solution procedure for a transient current source like the lightning discharge current is similar to the procedure introduced in Chapter 6, which converts a transient problem into an a.c. harmonic problem through Fourier transform and inverse Fourier transform.

7.6 Summary

In this chapter, the EC model of cylindrical conductors was integrated with the PEEC model of plates. Then the wire-plate model of building structure was transformed into an equivalent circuit network. Based on this integrated modeling approach, a preliminary study was conducted on a small scale model connected with an a.c. current source. From the preliminary study, some interesting observations were revealed, as follows

- The computer memory size and CPU time increased quickly with increasing dimension of plates and increasing frequency of concern.

- The proximity effect between two adjacent plates was neglected in the frequency spectrum of lightning. The current distribution inside a plate was approximated by a hyperbolic function.

- The variation of the current distribution along the tangential direction in the area around a joint had inherent patterns, which were approximated by analytical functions.

- The susceptance of the wire-plate model was neglected in the dominant frequency spectrum of lightning discharge current.

With above observations, modifications were adopted to optimize the PEEC modeling approach of plates. A novel hybrid analytical-numerical equivalent circuit (HANEC) modeling technique was then developed. These modifications included

- Generating even cells on the plates according to the predicted current distribution.
- Applying a hyperbolic function to approximate the normal current distribution inside plate.
- Deriving analytical functions to describe the tangential current distribution around wire-plate joints.
- Integrating the EC model of a cylindrical conductor and HANEC model of a plate.
- Simplifying the impedance matrix of the model matrix equation.

With the HANEC technique, it is possible to handle large wire-plate structure under a direct lightning stroke with reasonable memory size and high efficiency. Consequently, LIMF inside a wire-plate building structure under a direct lightning stroke can be evaluated accurately and efficiently.

Chapter 8

Characterization of LIMF Distribution inside a Scaled Wire-plate Structure

8.1 Introduction

Chapter 7 described the hybrid analytical-numerical equivalent circuit (HANEC) technique for modeling the wire-plate building structure under a direct lightning stroke. With this novel modeling technique, the current distribution in the structure can be evaluated in the frequency domain. Consequently, the lightning-induced impulse magnetic field (LIMF) inside the structure can be calculated. The characterization of LIMF inside a wire-plate building structure has been little addressed because this type of structure becomes popular in building construction in the recent years. With the proliferation of the wire-plate structure in high-rise buildings, the knowledge of LIMF distribution inside those buildings becomes critical in the protection of sensitive electronic equipment.

In order to provide fundamental knowledge about LIMF distribution in a building with the wire-plate structure, this chapter characterizes of LIMF inside a scaled room with the wire-plate structure under a direct lightning stroke. Firstly, the configuration of the wire-plate model is introduced. Secondly, LIMF distribution inside this model is characterized and compared with that around an independent downconductor. Finally, the magnetic fields in the wire-plate model are compared with those in the wire-grid model.

8.2 Configuration of a Scaled Wire-plate Model

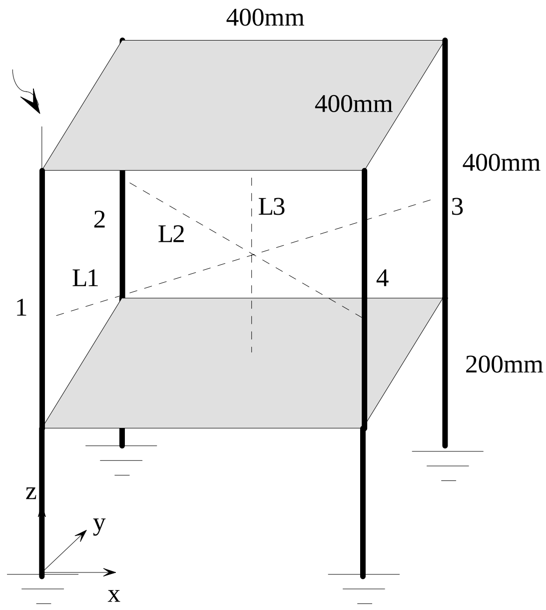

Figure 8.1 A scaled wire-plate model

Figure 8.1 illustrates the configuration of the scaled wire-plate model under discussion. This model is for a scaled room inside a building. Once LIMF distribution inside this room is revealed, the result can be applied to other rooms in the building.

As shown in Figure 8.1, the model is made of two aluminum plates and a number of vertical columns. The length and width of these plates inside this model are equal to 400mm. The length of the vertical columns between two layers is also equal to 400mm. The thickness of the plates is 1.5mm and the radius of columns is equal to 2mm. The lightning stroke terminates at a corner of the model, and is represented by a current source as stated in Chapter 3. The source current has a normalized peak value 1A and a waveform of 8/20μs (time to peak value/time to half peak value). In addition, the following assumptions are adopted in modeling:

- The influence of a lightning channel on LIMF distribution is not taken into consideration because its influence can be addressed separately.

- The ground is considered to be perfectly conductive.

8.3 Distrubtion of LIMF in the Wire-plate Model

Using the HANEC modeling technique and corresponding solution procedure proposed in Chapter 7, the impulse magnetic field inside this wire-plate model can be evaluated. In order to show clearly the distribution of the impulse magnetic field inside the structure, three observation lines inside the model were selected and the peak values of the impulse magnetic fields along these lines are calculated during a direct lightning striking at the air terminal. In order to study the shielding effect of the wire-grid structure, a reference model with only an independent downconductor was selected. The peak values of the impulse magnetic field generated by lightning discharge current in the reference model are evaluated.

Since the magnetic field is a spatial vector, its peak value in a Cartesian coordinate system is obtained by

$$B = \sqrt{B_x^2 + B_y^2 + B_z^2} \tag{8.1}$$

where B_x, B_y and B_z are respectively the peak values of the magnetic field in three orthogonal directions .

These three observation lines are, respectively, orthogonal and cross over at the center point of the model. As shown in Figure 8.1, L1 is the diagonal line between Column 1 to Column 3. L2 is the diagonal line between Column 2 to Column 4. L3 is in parallel with the z axis.

A. Magnetic Field Distribution along L1

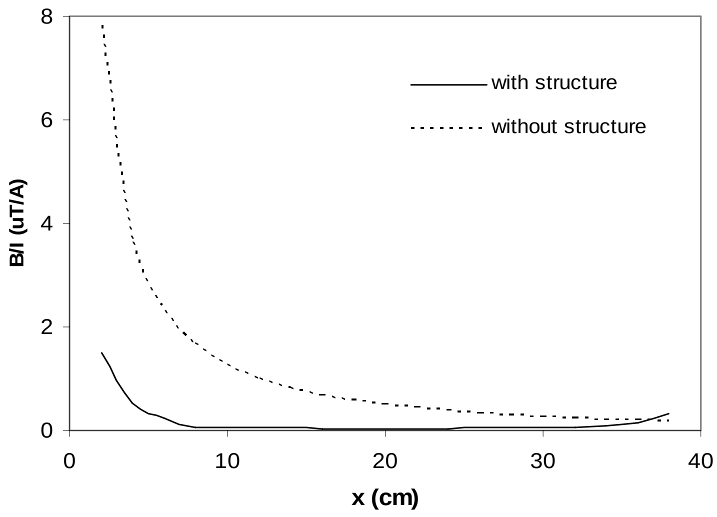

Figure 8.2 Magnetic field distribution along L1

Figure 8.2 shows the peak values of the impulse magnetic fields along L1 with respect to x coordinate when with and without the wire-plate structure. From Figure 8.2, it can be found that the magnetic fields decrease rapidly with increasing distance from the striking position. By comparing two curves, it is found that

- In the adjacent area around the striking position, the magnetic fields with structure are about 20% of that without structure. Although the magnetic fields in the wire-plate structure are greatly attenuated in this area, they could be still intense enough to threaten sensitive electronic equipment.

- In the middle area, the ratio of the magnetic fields in two situations decreases to 8% or so. It shows that the wire-plate structure has significant shielding effect. Then the sensitive equipment will be well protected in this area generally.

- In the far area, it is found that the ratio will increase even over 1. This is because the magnetic fields generated from current in the independent downconductor have decreased to a very low level while the current flowing in the far column is the major contributor of the magnetic fields there.

B. Magnetic Field Distribution along L2

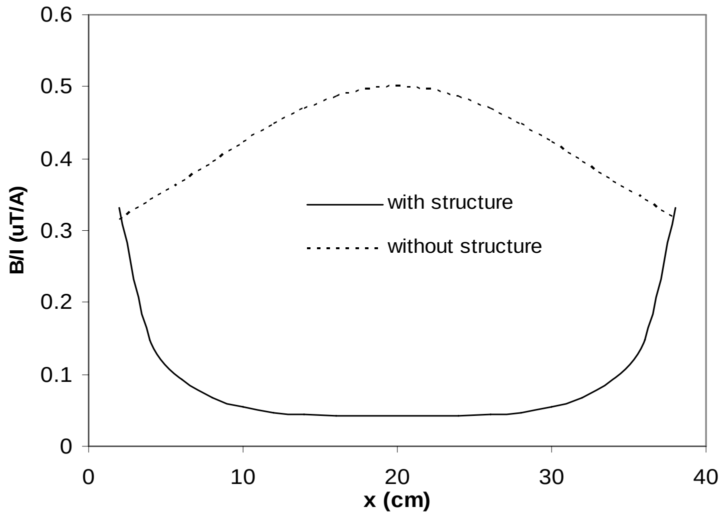

Figure 8.3 Magnetic field distribution along L2

Figure 8.3 shows the peak values of the impulse magnetic field along L2 with respect to x coordinate when with and without the wire-plate structure By comparing the two curves in Figure 8.3, it is again found that the magnetic fields inside the middle area of a wire-plate structure are much less than those with an independent downconductor. The minimal ratio between them in the middle area is 8%. In the adjacent areas around two columns, the magnetic fields will increase quickly and the ratio of between situations will approach 1. This is also because of the contribution from the current in the two columns which intensifies the magnetic fields there.

C. Magnetic Field Distribution along L3

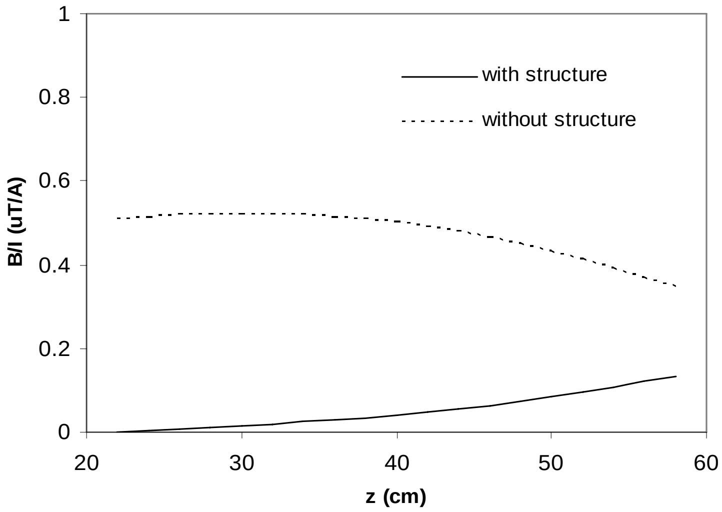

Figure 8.4 Magnetic field distribution along L3

Figure 8.4 illustrates the peak value of impulse magnetic fields along L3 with respect to z coordinate with and without the wire-plate structure. By comparing two curves in Figure 8.4, it is noted that the magnetic fields from the current in the isolated downconductor keep comparatively stable. However, the magnetic fields inside the wire-plate structure long L3 will increase with increasing height. This is because the contributed magnetic fields from the current distribution in the upper plate become larger when the observation point approaches it. So it is better to avoid placing sensitive equipment close to the roof of buildings with wire-plate structures.

On the contrary, the magnetic fields decease when the observation point approaches the low plate. This is because the lower plate is earthed by four lower columns through which most currents from upper columns are injected into the earth. So the current following in the lower plate is small and its contributed magnetic fields are cancelled by the increasing magnetic fields from the low columns.

8.4 Compasion with LIMF in a Wire-grid Structure

By replacing the two plates with four cylindrical conductors, the wire-plate model in Figure 8.1 is transformed into a wire-grid model as Figure 8.5 shows. Using the equivalent circuit (EC) approach proposed in Chapter 3, the magnetic fields inside the wire-grid structure can be calculated.

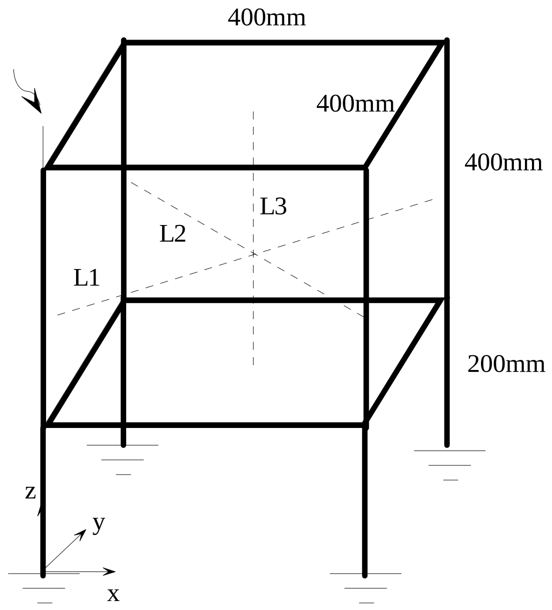

Figure 8.5 A scaled wire-grid model

Similar to the case for the wire-plate model in Section 8.3, the peak values of magnetic fields along three observation lines L1, L2 and L3 inside the wire-grid model are evaluated. The evaluation results are plotted together with those of the wire-plate model along three lines respectively.

A. Magnetic Field Distribution along L1

Figure 8.6 shows the peak values of impulse magnetic fields along L1 with respect to x inside the wire-plate model and the wire-grid model. From Figure 8.6, it is noted that the magnetic fields inside two models both decreases with increasing distance to the striking position. But the magnetic fields inside the wire-plate model are much less than those inside the wire-grid model. In the position of x=10cm, the minimal ratio between the magnetic fields inside the wire-plate model and the wire-grid model is as small as 5%. This shows the shielding effect of the wire-plate structure is superior to that of the wire-grid model.

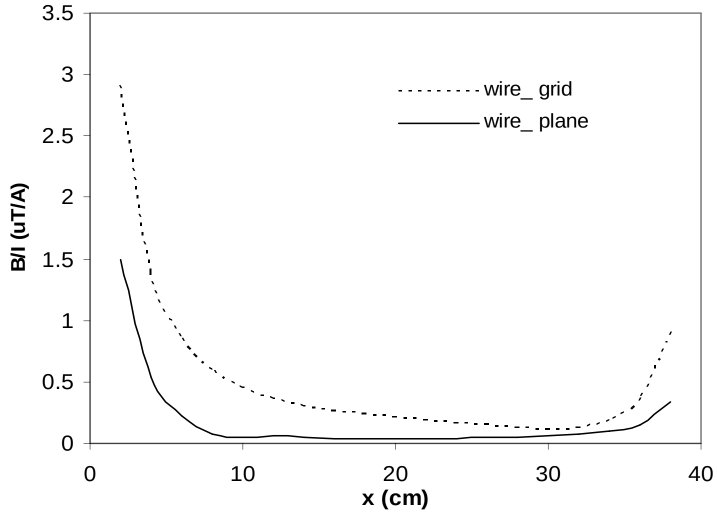

Figure 8.6 Comparison of magnetic field distribution along L1

B. Magnetic Field Distribution along L2

Figure 8.7 shows the peak values of impulse magnetic fields along L2 with respect to x inside the wire-plate model and the wire-grid model. From Figure 8.7, detailed comparison between the magnetic fields inside the middle area inside two models is revealed. It is noted that the average magnetic fields inside the middle area of the wire-plate model are about 17% of those inside the middle area of the wire-grid model. So the sensitive equipment is safer if they are placed inside a wire-plate building structure than inside the wire-grid structure.

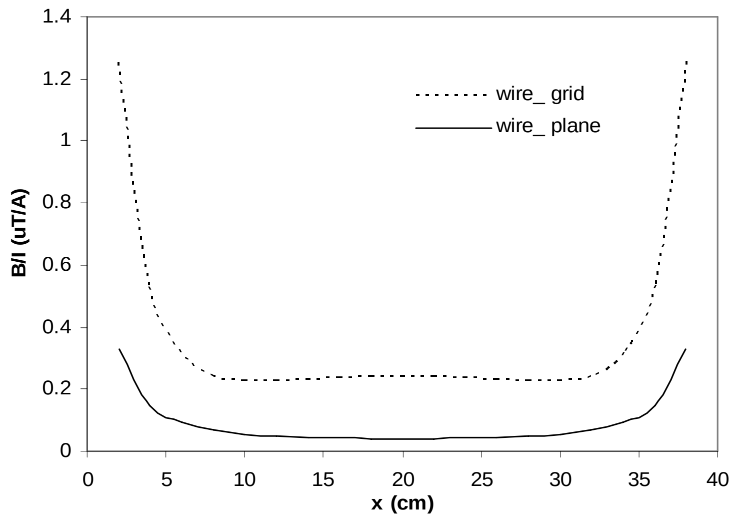

Figure 8.7 Comparison of magnetic field distribution along L2

C. Magnetic Field Distribution along L3

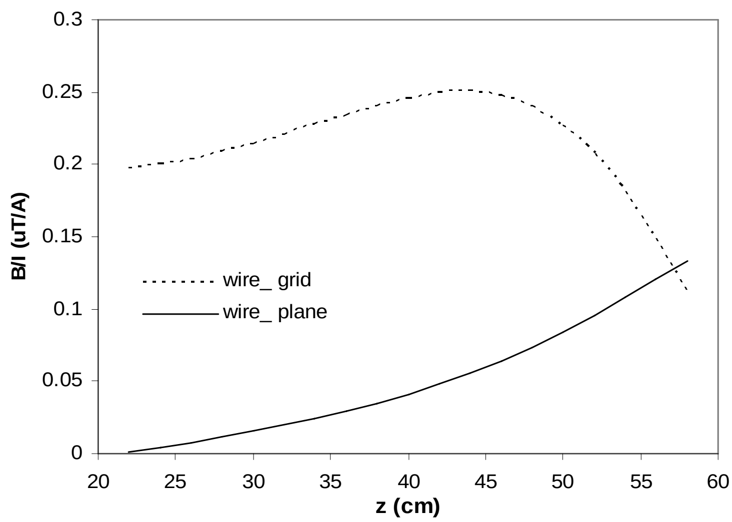

Figure 8.8 Comparison of magnetic field distribution along L3

Figure 8.8 shows the peak values of impulse magnetic fields along L3 with respect to z inside the wire-plate model and the wire-grid model. By comparing two curves in Figure 8.8, it can be seen that the magnetic fields at different heights inside the middle region of the wire-plate model are much less than those inside the wire-grid model except in the region very close to the upper plate. It again proves that the wire-plate model has better shielding effect than the wire-grid structure.

In addition, it is found that when the observation point approaches the roof, the magnetic fields inside the wire-grid model decrease rapidly. The reason is that the currents flowing in upper four horizontal branches are symmetrical. According to the superposition theorem, the magnetic fields generated by the currents in four branches will counteract when the observation point approaches the roof center.

8.5 Summary

This chapter characterized LIMF distribution inside a scaled wire-plate room inside a building. Using the HANEC modeling technique, the magnetic fields inside this model were evaluated and compared with the magnetic fields generated from an independent downconductor. It is found that the wire-plate structure has good shielding effect. By comparing the magnetic fields inside the wire-plate model and inside a wire-grid model, it is found that the shielding effect of the wire-plate model is much better than that of wire-grid model. In the middle region, the shielding effect of the wire-plate model is six times of that of the wire-grid structure.

Chapter 9

Experimental Study

9.1 Introduction

The equivalent circuit (EC) modeling approach for wire-grid building structures was proposed in Chapter 3. Afterward, the partial element equivalent circuit (PEEC) modeling approach for non-ferromagnetic plates was developed in Chapter 6. In Chapter 7, this approach was further developed and the hybrid analytical-numerical equivalent circuit (HANEC) technique was proposed for modeling wire-plate structures under direct lightning strokes. In this chapter, laboratory experiments are presented to validate these modeling approaches addressed in those chapters. Since all the validation experiment were conducted on scaled and simplified models in laboratories, when the proposed modeling approaces are applied to real buildings, some extra errors are expected due to the simplification of the complicated building structures when building their models.

This chapter starts with an introduction on the equipment and measuring apparatuses used in the experiments. Four validation experiments are then presented. The first experiment was intended to validate the EC modeling approach proposed in Chapter 3, and was conducted on the wire-grid structure with an isolated downconductor under a lightning stroke. The second and third experiments were intended to validate the PEEC modeling approach proposed in Chapter 6, and were conducted on independent aluminum plates and on an aluminum wire-plate structure in a.c. magnetic fields respectively. The fourth experiment validated the HANEC modeling technique proposed in Chapter 7 on an aluminum wire-plate structure under a direct lightning stroke.

9.2 Equipment and Measuring Apparatuses used in Experiments

9.2.1 Impulse Current Generator

Figure 9.1 Impulse current generator (ICG)

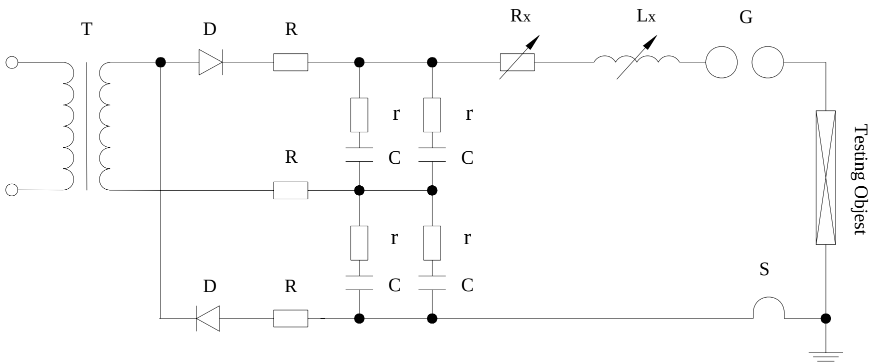

Figure 9.2 Schematic diagram of ICG

In the experiments associated with a lightning stroke, the lightning return stroke current was simulated and was generated by an impulse current generator (ICG). Figure 9.1 is a photo of the ICG used in the experiments for this thesis. This ICG is a commercial product developed by Shanghai Jiaotong University. It can generate an impulse current with the peak value up to 40KA. Figure 9.2 illustrates the schematic diagram of ICG.

As shown in Figure 9.2, ICG consists of two major parts: a charging circuit and a discharging circuit. The charging circuit includes a test transformer (T), two diodes (D), and three charging resistors (R). The energy is stored in capacitors (C) via the charging circuit. The discharging circuit includes discharging resistors and inductors (Rx and Lx), a spark gap (G) for triggering, and the equipment under test (R).

During a discharge phase, the schematic diagram of ICG can be simplified to a simple discharge circuit shown in Figure 9.3. C is the total capacitance of the group of capacitors. L and R are, respectively represent the total inductance and resistance of capacitors, discharging resistors, discharge inductors, loop wires, the shunt, the gap and the tested object.

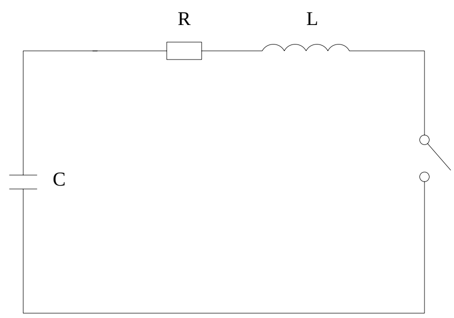

Figure 9.3 Equivalent discharge circuit of ICG

According to the basic circuit theory, if a group of capacitors is charged to a voltage U_0, the following equation is applied if the gap is broken down.

$$U_0 - \frac{1}{C}\int i dt = L\frac{di}{dt} + Ri \tag{9.1}$$

From (9.1), it is noted that the magnitude and waveform of an impulse current in the circuit is dependent on resistance R, inductance L and capacitance C as well as the charging voltage U_0 .By altering resistance, inductance and capacitance in the discharge circuit, both the desired magnitude and waveform of the impulse current from ICG are obtained.

In order to avoid elevation of the earth potential, the whole test circuit was earthed at a common earthing point.

9.2.2 Apparatuses for Measuring Impulse Currents

The duration of the impulse current generated by ICG lasts for only several microseconds. The apparatuses for measuring such a short impulse current should have a wide enough linear frequency band with adequate linearity and accuracy. Two current measuring systems were set up. One is the shunt plus digital oscilloscope (shunt-CRO) system which is used to measure the total current generated from ICG. The other is the Rogowaski plus digital oscilloscope (Rogowaski-CRO) system which is used to measure currents in the structure under test.

A. Shunt-CRO System

Figure 9.4 illustrated the configuration of a shunt plus digital oscilloscope (shunt-CRO) system which is used in measuring the impulse current. In the shunt-CRO system, the shunt is a resistor with very low resistance and extremely low inductance. It has a fairly wide band. The peak value of an impulse current to be measured can be as high as several hundred kilo ampere. The shunt is connected seriesly into the discharge loop of ICG. The output signal of the shunt is transferred to the digital oscilloscope through a shielded coaxial cable. The waveform of the impulse current can be caught by the oscilloscope

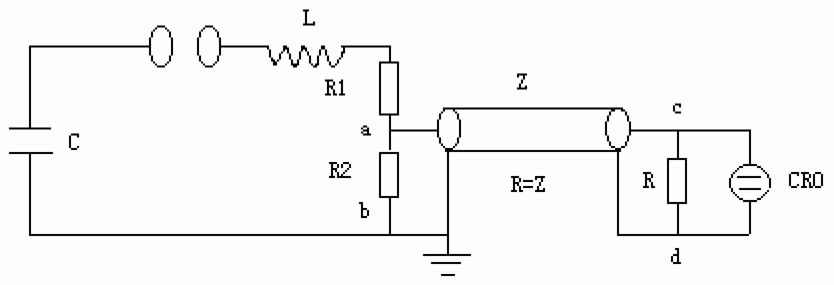

L —— discharge inductor R1—— object under test (EUT)

R2—— shunt Z —— wave impedance

R —— matched resistor

Figure 9.4 Shunt-CRO current measuring system

When the impulse current flows through the shunt, a voltage drop yields between its two terminals of a and b, as shown in Figure 9.4

$$U_{ab}(t) = i(t) \times R_2 \tag{9.12}$$

The signal of the voltage drop is sent to CRO by the shielded coaxial cable equipped with a match resistor at the cable end. The wave form of the impulse current can be obtained with the following equation

$$i(t) = U_{cd}(t) / R_2 = U_{ab}(t) / R_2 \tag{9.13}$$

Figure 9.5 shows the shunt used in the experiments which was developed by the Shanghai Jiaotong University. The sensitivity of the shunt is 0.0052421V/A and maximal impulse current is 40kA. Its accuracy has been calibrated with an error less than 0.5%. The digital oscilloscopes used in the experiments were TDS7104 from the Techtronic Company and Wavesurfer 454 from the Lecroy Company.

Figure 9.5 Shunt

B. Rogowaski Coils

Although the shunt-CRO system has a high accuracy in impulse current measurement, the shunt can not be used in the structures under test. For example, in the wire-grid structure, it is not possible to insert a shunt to a branch. Another non-contact measuring method, namely Rogowaski-CRO system plays an important role in impulse current measurement. The great advantage of the Rogowaski-CRO system is that it doesn't need direct connection with the discharge circuit. So there is no dynamical and thermal problem. In addition, since the Rogowaski coil is independent to the discharge circuit, the interference due to the earthy potential elevation can be avoided completely.

Figure 9.6 illustrates the configuration of a Rogowaski-CRO system used to measure an impulse current. When an impulse current flows through the Rogowaski coil, there is a signal of voltage generated from the Rogowaski coil. Similar to the shunt-CRO system, this signal is transferred to CRO by a shielded coaxial cable, as seen in Figure 9.6.

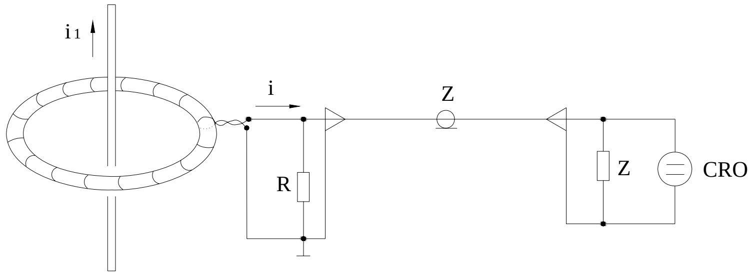

Figure 9.6 Rogowaski-CRO current measuring system

The output voltage has a linear relationship with the impulse current flowing through the Rogowaski coils as follows

$$U(t) = S \cdot i_1(t) \tag{9.14}$$

where S is the sensitivity of the Rogowaski coil in the unit V/kA.

Figure 9.7 Rogowaski coil

The Rogowaski coils of CM-10-L and CM-1-L shown in Figure 9.7 used in the experiments were manufactured by the Ion Physics Corporation Company in USA. The output sensitivities are respectively 0.1V/A and 0.01V/A. The maximal impulse currents to be measured are respectively 5kA and 50kA. From the calibration report provided by the manufacturer, the measuring error is less than 5%. The waveforms of an impulse current measured by shunt-CRO system and by Rogowaski-CRO system are both shown in Figure 9.8. It is noted that the waveform from both measuring systems have the same waveform although the peak values are different due to their different sensitivities.

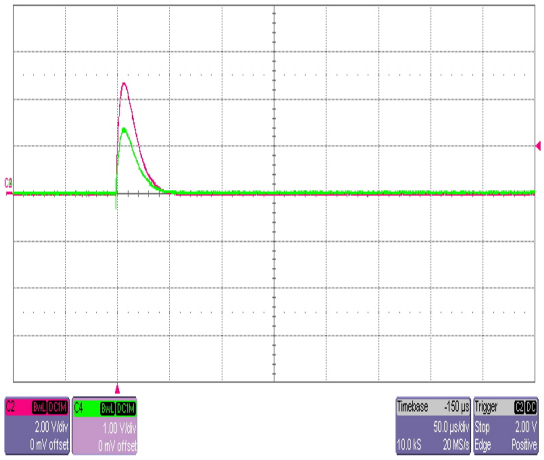

upper- measured by shunt-CRO system

lower- measured by Rogowaski-CRO system

Figure 9.8 Waveforms from Rogowaski coils and ICG shunt

9.2.3 Apparatuses for Measuring Impulse Magnetic Fields

9.2.3.1 Tailor-made Magnetic Field Probe

To measure the impulse magnetic fields arising from the simulated lightning stroke in the structure under test, there are no commercial products available to output the waveform of a transient magnetic field. So a magnetic field probe was designed and manufactured by the author in the laboratory.

A. Measurement principle

For the measurement of a non-uniform impulse magnetic field, the magnetic field probe designed from the induction effect is simple and reliable. The equivalent circuit of the probe is shown in Figure 9.9

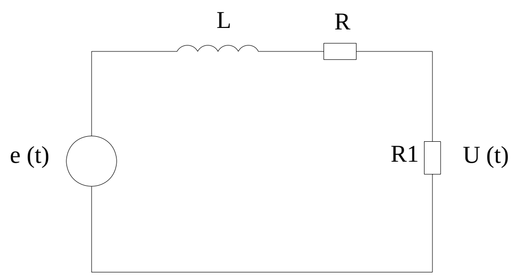

Figure 9.9 Equivalent circuit of self-inductance integral circuit

In Figure 9.9, e(t) is the induced electrical force in the coil. R and L are respectively the internal resistance and inductance of the coil. R1 is the external resistance connected between the two terminals of the coil.

Assuming the number of coils in the probe is N and the section area is S, the electrical force produced in the probe is

$$e(t) = -\frac{d\Phi}{dt} = -NS\frac{dB}{dt} \tag{9.15}$$

In the equivalent circuit, an equation according to Kirchhoff’s Voltage Law (KVL) is obtained

$$\begin{cases} e(t) = L\dfrac{di(t)}{dt} + (R_0 + R)i(t) \\ i(t) = \dfrac{U(t)}{R} \end{cases} \tag{9.16}$$

Combining (9.15) and (9.16), the magnetic field penetrating the probe perpendicularly is obtained

$$B(t) = \frac{L}{NSR}U(t) - \frac{(R_0 + R)}{NSR}\int_0^t U(\tau)d\tau \tag{9.17}$$

In (9.17), when $L\frac{di(t)}{dt} >> (R_0 + R)i(t)$, namely $\omega L >> R_0 + R$, (9.17) can be simplified as

$$B(t) = -\frac{L}{NSR}U(t) \tag{9.18}$$

Then, once U is measured by an oscilloscope, B can be calculated by (9.18) directly.

B. Probe Construction

In order to measure magnetic field distribution within the structure, the magnetic field probe should be as small as possible. Figure 9.10 shows the geometric construction parameters of the probe.

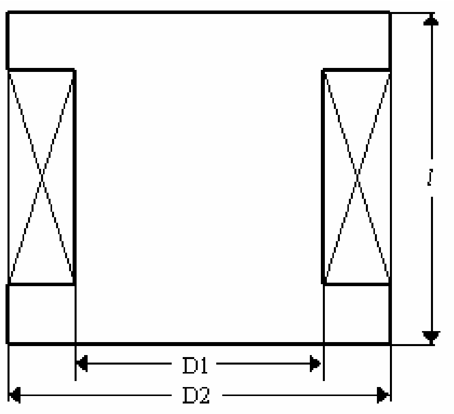

D1 = 20mm, D2=32mm and l=23mm

Figure 9.10 Geometric construction

In the measurement the field probe is likely subject to intense electromagnetic field radiated from spark gaps and other devices in ICG. To minimize the induced voltage caused by any unwanted electric field, a thin copper slice was applied to cover both inner and outer surfaces of the coil, as illustrated in Figure 9.11. This copper slice was designed to be an open-ring layer to prevent an induced current on the shielding layer.

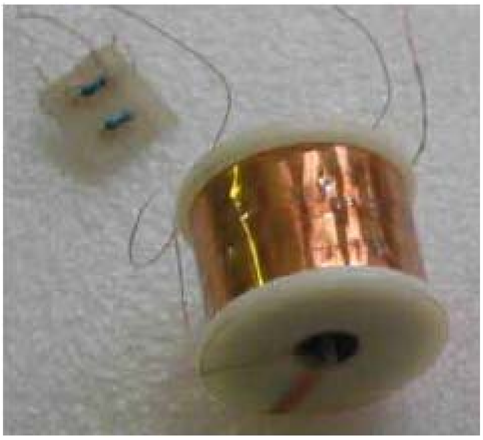

Figure 9.11 Cooper shielding on probe coils

C. Calibration

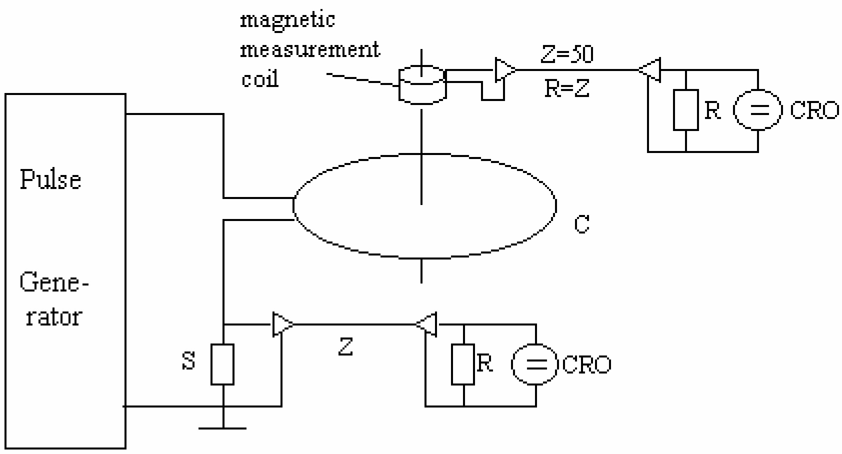

Figure 9.12 Circuit for calibrating the magnetic field probe

In order to calibrate the linearity and sensitivity of the tailor-made probe, a calibration experiment was setup as shown in Figure 9.12. C is a single-turn coil with radius r to produce magnetic field; S is the current shunt which is used to measure the current flowing through C. The magnetic field in the center of C can be calculated by $B = \frac{\mu_0 I}{2r}$.Then, the ratio between the calculated magnetic field B and the measured output voltage of the probe can be obtained by $K = \frac{B}{U}$. The measurement results are shown in Table 9.1.

Table 9.1 Measured sensitivity and linearity of the magnetic probe

X(m)	I×10^3 (A)	B×10^{-4}(T)	Vp(V)	K(=B/Vp)
1.365	1.7744	0.7265	0.4760	1.5263
1.365	1.4856	0.6083	0.3960	1.5360
1.365	1.1692	0.4787	0.3080	1.5543
1.365	0.9904	0.4055	0.2560	1.5840
1.365	0.8583	0.3514	0.2280	1.5414
1.365	0.7648	0.3131	0.2020	1.5502
1.365	0.5887	0.2410	0.1580	1.5256
1.365	0.4237	0.1735	0.1120	1.5488
1.365	0.3906	0.1599	0.1020	1.5681
0.865	1.6919	2.2387	1.5000	1.4925
0.865	1.5543	2.0567	1.3800	1.4904
0.865	1.4856	1.9657	1.3100	1.5006
0.865	1.2930	1.7109	1.1400	1.5008
0.865	1.1417	1.5107	0.9900	1.5260
0.865	1.0564	1.3979	0.9500	1.4714
0.865	0.9188	1.2158	0.8300	1.4649
0.865	0.8088	1.0702	0.7300	1.4661

0.865	0.6602	0.8737	0.5880	1.4858
0.865	0.5557	0.7353	0.4800	1.5319
0.865	0.5117	0.6771	0.4520	1.4980
0.865	0.4347	0.5752	0.3840	1.4978
0.635	1.5681	4.1194	2.9000	1.4205
0.635	1.4305	3.7580	2.6200	1.4344
0.635	1.3480	3.5412	2.4600	1.4395
0.635	1.2380	3.2521	2.2400	1.4518
0.635	1.1692	3.0715	2.1400	1.4353
0.635	0.9904	2.6017	1.8000	1.4454
0.635	0.9216	2.4210	1.6600	1.4585
0.635	0.8088	2.1247	1.4700	1.4454
0.635	0.6878	1.8067	1.2600	1.4339
0.435	1.4856	7.6138	5.3200	1.4312
0.435	1.3893	7.1203	4.9600	1.4355
0.435	1.2242	6.2743	4.3600	1.4391
0.435	1.1554	5.9218	4.1600	1.4235
0.435	1.0591	5.4283	3.7600	1.4437
0.435	0.9491	4.8643	3.4000	1.4307
0.435	0.8803	4.5119	3.1600	1.4278
0.435	0.7648	3.9197	2.7400	1.4305

In Table 9.1, X means the distance between the probe and the center of the circular loop. Is means the magnitude of the impulse current from ICG. Vp means the output voltage of the magnetic probe. B is the magnetic field at the loop center which is calculated from the Is by Bio-savart Law. K is the ratio between B and Vp. From

Table 9.1, the average value of K is obtained as K=1.4813 which is applied in the measurements in following experiments.

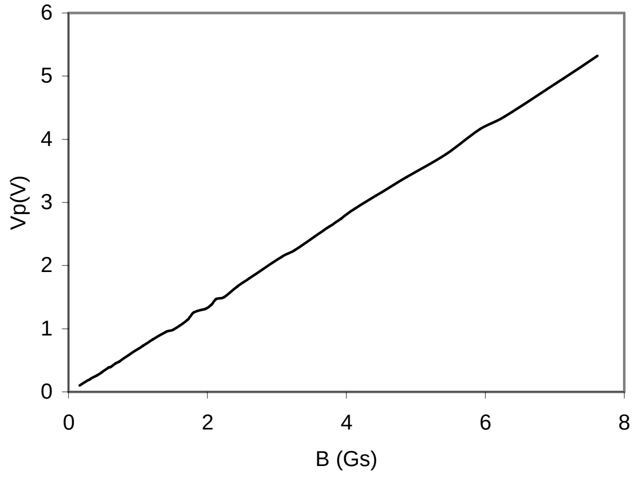

Figure 9.13 Linearity of the magnetic field probe

Figure 9.13 illustrated the linearity of the magnetic field probe. It can be calculated that the linearity error is less than 7%.

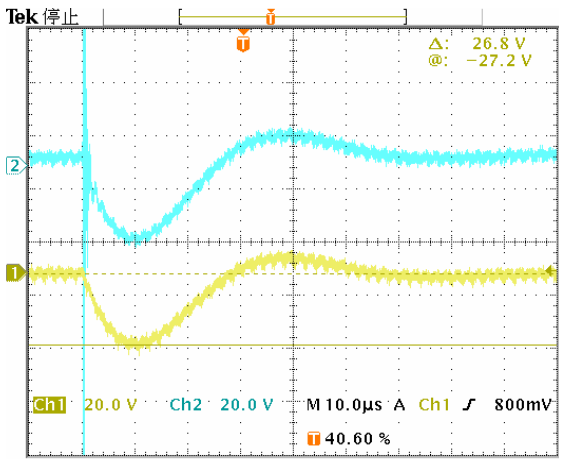

upper waveform – the impulse current

low waveform – the magnetic field

Figure 9.14 Waveforms from the shunt and from the magnetic field probe

Figure 9.14 shows the two waveforms: one is of the impulse current measured by a current shunt; the other is of the output voltage from the magnetic field probe. From these two waveforms, it is noted that the frequency characteristics of the probe is good enough to measure the impulse magnetic field. In addition, it shows that little disturbance appears in the waveform of the output voltage after the shielding measure was implemented.

9.2.3.2 EMDEX II Magnetic Field Exposure System

EMDEX II shown in 9.15 is a commercial product to measure to measure magnetic fields under steady state. According to the calibration report provided by the manufacturer, it has a frequency band from 40Hz to 800Hz and a typical accuracy of ±1%.

Figure 9.15 EMDEX II

9.3 Wire-grid Structures with an Isolated Downconductor

A. Experimental Setup

A scaled model of building structure was set up in the laboratory, as Figure 9.16 shows, to validate EC modeling approach proposed in Chapter 3,. The scaled model included an isolated downconductor and a wire-grid structure formed by a number of interconnected RC bars, as illustrated in Figure 9.16. A large metal plate was placed under the wire-grid structure to represent a perfect conductive earth. The wire-grid structure was constructed with 260 bars, each of which was 0.5m long and had a diameter of 5mm. The downconductor was erected vertically and stood on the metal plate. Its lower ends of core and screening were bonded together on the metal plate. The downconductor was 2.5m long, and had mean diameters of 12.3mm and 24.1mm for its core and screening, respectively. The upper end of the downconductor core was connected to ICG with copper wires.

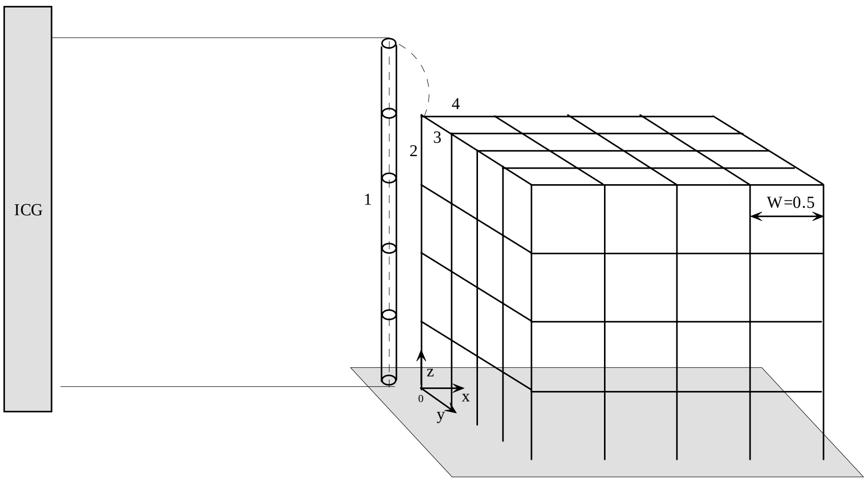

Figure 9.16 Configuration of the wire-grid experiment

In each test an impulse current from ICG was injected into the core of the downconductor. The impulse current had a nominal peak value of 11kA. Because the structure was a large inductive load, the steepest rising time to the peak value of the obtained impulse current from ICG was 7.8μs, and the time to its half peak value was 17.6μs. During the test induced currents were generated in the branches of the wire grid as well as in the screening of the downconductor. These currents were measured with the Rogowaski-CRO system. The resulting impulse magnetic fields at several points inside the structure were measured with the tailor-made magnetic field probe. The peak value of the impulse magnetic field was normalized by dividing the peak value of the impulse current from ICG.

B. Comparison between Measured and Calculated Results

Two configurations of the downconductor were tested in the experiment. These configurations included (a) the downconductor was electrically isolated from the wire grid except on the metal plate; (b) the upper end of the downconductor screening was bonded to a corner of the wire grid, as illustrated in Figure 9.16. It should be mentioned that configuration (b) was not recommended by the manufacturer, but was selected for model validation only. For simplicity, both impulse current and magnetic field were normalized with the peak value of the impulse current from ICG.

1) Current Distribution

Table 9.2 shows both calculated and measured peak values of the normalized currents in screening (Branch 1) and 3 branches. In configuration (a), the current in screening was too small to measure because of electrical isolation of the screening. The current in screening, however, became significant in configuration (b) because of bonding at the upper end. The induced current was allowed to circulate between the screening and the wire grid. It is noted from the table that both measured and calculated currents match very well with an average error of less than 5%.

Table 9.2 Normalized peak values of the impulse currents in four branches

Test Configuration		Branch 1	Branch 2	Branch 3	Branch 4
(a)	Measured	0.0%	13.1%	8.66%	4.46%
	Calculated	0.0%	13.5%	8.98%	4.77%
(b)	Measured	54.9%	13.7%	22.9%	18.3%
	Calculated	54.2%	13.9%	21.7%	17.4%

2) Magnetic Field distribution

The impulse magnetic fields were measured at three typical points within the wire grid. Table 9.3 shows the peak value of the x components of the impulse magnetic fields for comparison. In both configurations, the measured and calculated results match well, with an average error of less than 5%. It is noted from Table 9.3 that the impulse magnetic fields in configuration (b) are much less than those in configuration (a). As seen in Table 9.3, the screening carried a significant induced current. This current flowed in the opposite direction of the downconductor current, which led to a significant cancellation of the field within the wire grid.

Table 9.3 Normalized peak values of the impulse magnetic field B_x/I (10^{-4}T/kA)

Test Configuration		Point 1 (0.0, 0.25, 0.75)	Point 2 (0.125, 0.25, 0.75)	Point 3 (0.25, 0.25, 0.75)
(a)	Measured	3.41	2.40	1.59
	Calculated	3.49	2.37	1.62
(b)	Measured	1.21	0.70	0.36
	Calculated	1.17	0.73	0.38

9.4 Aluminum Plates Excited by an a.c. Magnetic Field

In order to validate PEEC modeling approach for a non-ferromagnetic plate in Chapter 6, a series of experiments are conducted in the laboratory. In these experiments, three different configurations of aluminum plates were applied. The measured results are compared with the calculated results with PEEC approach in Chapter 6 for each experimental configuration.

9.4.1 Singe Plate on Parallel with the Source Coil

A. Experimental Setup

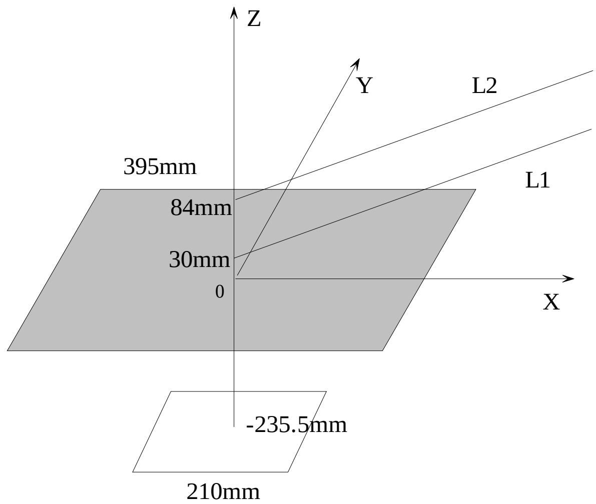

Figure 9.17 Configuration of the singe plate experiment

The physical model in the experiment is illustrated in Figure 9.17. A square aluminum plate was placed above a square coil. The width of the square plate was 395mm and the thickness was 1.5mm. The width of the square coil was 210mm. The distance between the plate and coil was 235.5mm. An a.c. source current of 700Hz was injected into the square coil. The magnetic fields in the z direction along the line

L1 and the line L2 were measured with the EMDEX II. L1 was 30mm above the plate and L2 was 84mm above the plate.

B. Comparison between Measured and Calculated Results

The measured magnetic fields in the z direction were normalized by dividing the current in the squash coil. The normalized magnetic fields along L1 and L2 from measurement together with those obtained from calculation were plotted in Figure 9.18 and Figure 9.19. In the calculation, the plate was divided into 30×30 identical x-cells and y-cells. In both figures, the coordinate d represents the distance between the measuring point and the origin point, i.e. $d = \sqrt{x^2 + y^2}$.

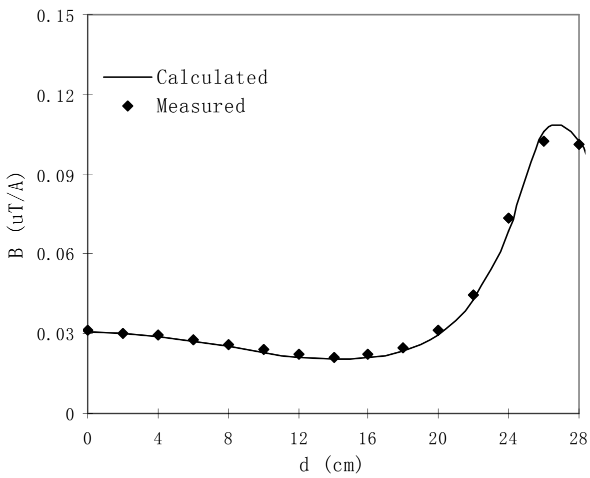

Figure 9.18 Comparison of the normalized magnetic field in the z direction along L1

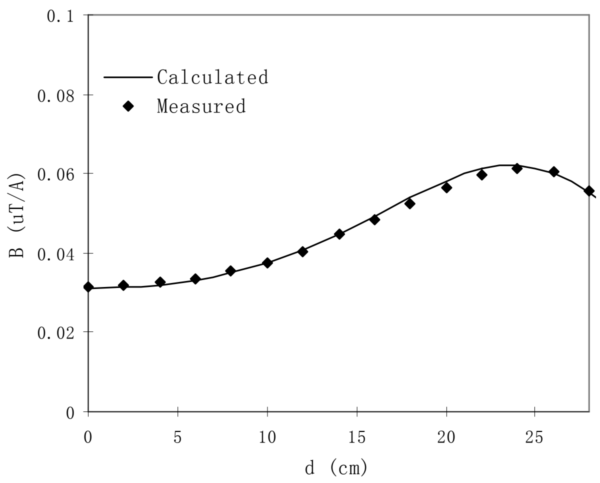

Figure 9.19 Comparison of the normalized magnetic field in the z direction along L2

From Figures 9.18 and 9.19, it is noted the results from measurement and calculation match very well. In Figure 9.18, the maximum error between them is less than 5.5%. In Figure 9.19, the maximum error is as small as 3.3%. It is found that the accuracy of the PEEC approach is increased with increasing distance from the plate. This is because the calculated eddy current distributed in the aluminum plate is an approximation of the actual current. At the place close to the plate, the error of the magnetic fields calculated from the eddy current distribution by Bio-savart Law becomes obvious.

9.4.2 Two Parallel Plates Perpendicular to the Source Coil

A. **Experimental Setup**

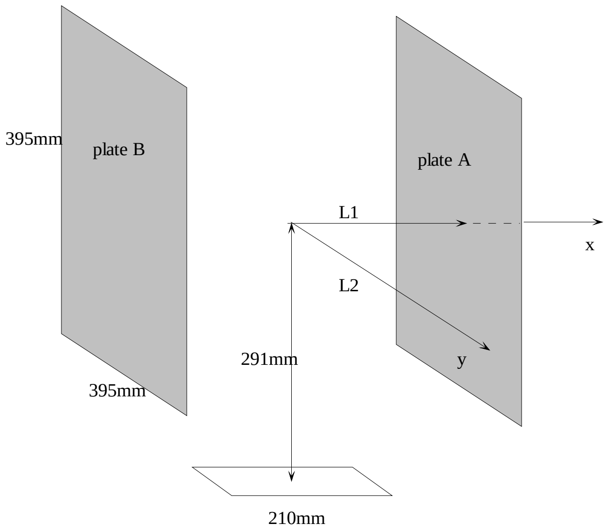

Figure 9.20 Configuration of two parallel plates experiment

To investigate the proposed modeling approach for a combination of independent plates, a different experimental model was setup as shown in Figure 9.20. Two identical square aluminum plates were placed parallel to each other with a separation distance of 400mm. They were erected perpendicularly above a square coil. The distance between the center of plates and the coil center was 291mm. The width of each square plate was 395mm and the thickness was 1.5mm. The width of the square coil was 210mm. An a.c. current of 700Hz was injected into the square coil. The magnetic fields in the z direction along the line L1 and the line L2 were measured with the EMDEX II. As seen in Figure 9.20, L1 was perpendicular to the plate A passing the plate center and L2 was parallel to plate A with a distance 200mm.

B. Comparison between Measured and Calculated Results

The measured magnetic fields in the z direction were normalized by dividing the current flowing in the square coil. Then the normalized measured results together with those obtained from the proposed method were both plotted in Figure 9.21 and

Figure 9.22. In the calculation, the plate was modeled by 30×30 identical x-cells and y-cells.

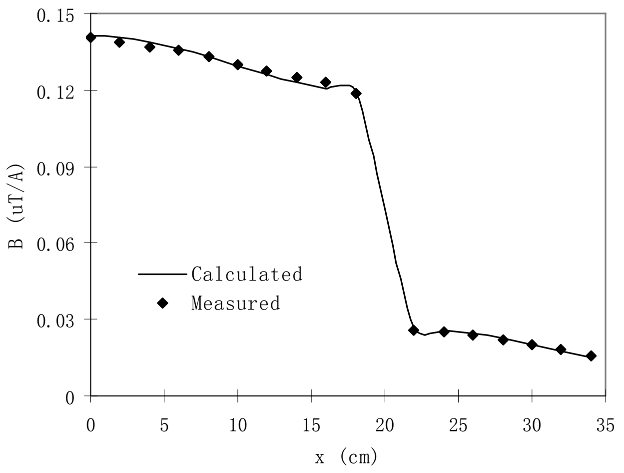

Figure 9.21 Comparison of the normalized magnetic field in the z direction along L1

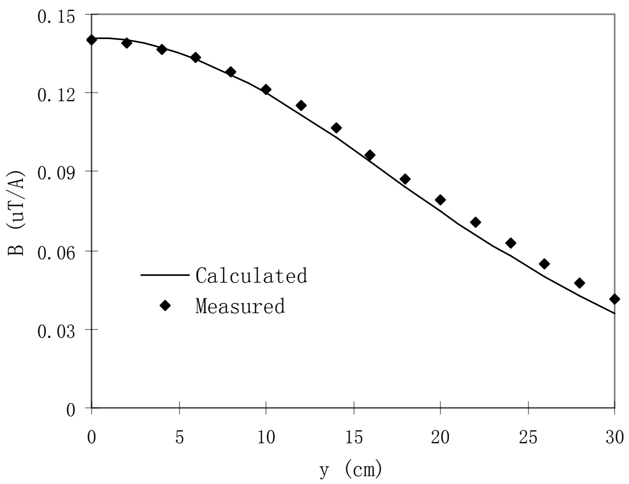

Figure 9.22 Comparison of the normalized magnetic field in the z direction along L2

From Figure 9.21 and Figure 9.22, it is noted the results from the measurement and the calculation match very well. The maximum error of the field on L1 is less than 6%. The maximum error of the field on L2 is less than 8%. In Figure 9.21, it is found that the magnetic field in the z direction drops significantly when the observatory point is moved from one side of a plate to the other. While in Figure 9.22, the magnetic fields in the z direction decrease with increasing y coordinate gradually.

9.5 Aluminum Wire-plate Structure Excited by an a.c. Magnetic Field

A. Experiment Setup

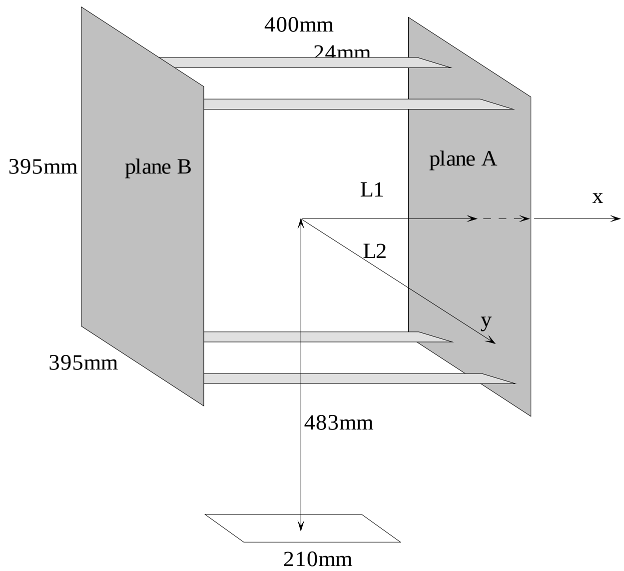

Figure 9.23 Configuration of a wire-plate structure

The PEEC modeling approach in Chapter 6 was experimentally investigated by using a wire-plate structure. The experimental model is shown in Figure 9.23. The structure was made from two identical square aluminum plates and four aluminum columns. A square coil was placed below the structure and perpendicular to the two parallel plates. The width of the square plate was 395mm and the thickness is 1.5mm. The width of the square coil was 210mm. The distance between the center points of the structure and the coil was 483mm. An a.c. current of 700Hz was injected into the square coil. The magnetic fields in the z direction along L1 and L2 were respectively measured with EMDEX II.

B. Comparison between Measured and Calculated Results

The measured magnetic fields in the z direction were normalized by dividing the current flowing in the square coil. Then the normalized measured results together with those obtained from the proposed method were both plotted in Figure 9.24 and Figure 9.25. In the calculation, the plate was modeled by 30×30 identical x-cells and y-cells.

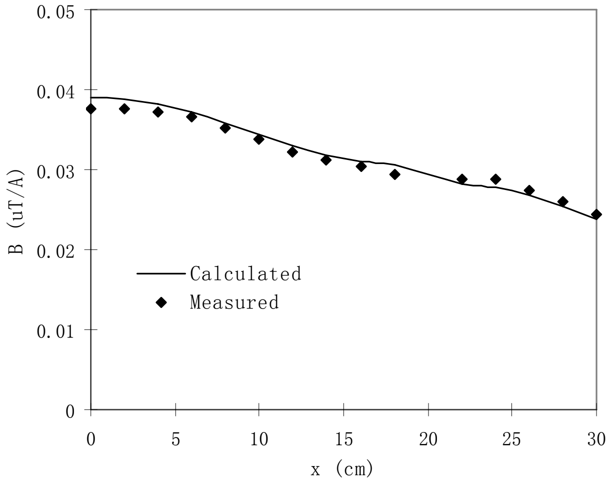

Figure 9.24 Comparison of the normalized magnetic field in the z direction along L1

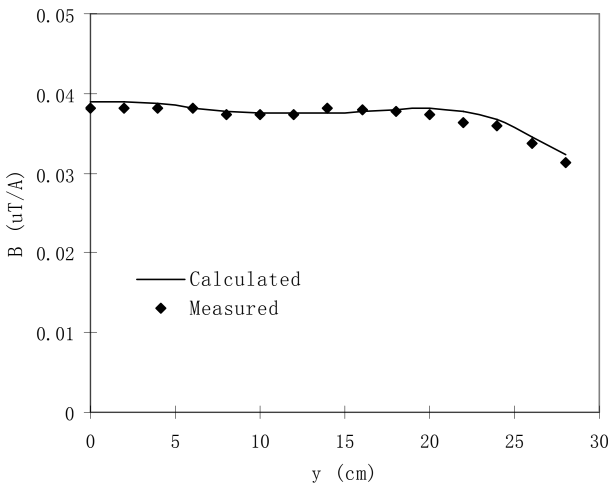

Figure 9.25 Comparison of the normalized magnetic field in the z direction along L2

From Figure 9.24 and Figure 9.25, it is noted the results from the measurement and the calculation match very well. The maximum error of the field on L1 is 4.1%. The maximum error of the field on L2 is 3.7%. In Figure 9.24, it is found that unlike the configuration of two parallel plates, the magnetic field drops significantly when the observatory point on L1 is moved from one side of a plate to the other. The magnetic fields decrease gradually when crossing the plate. In Figure 9.25, the magnetic fields decrease gradually along L2.

9.6 Aluminum Wire-plate Structure under a Direct Lightning Stroke

A. Experiment Setup

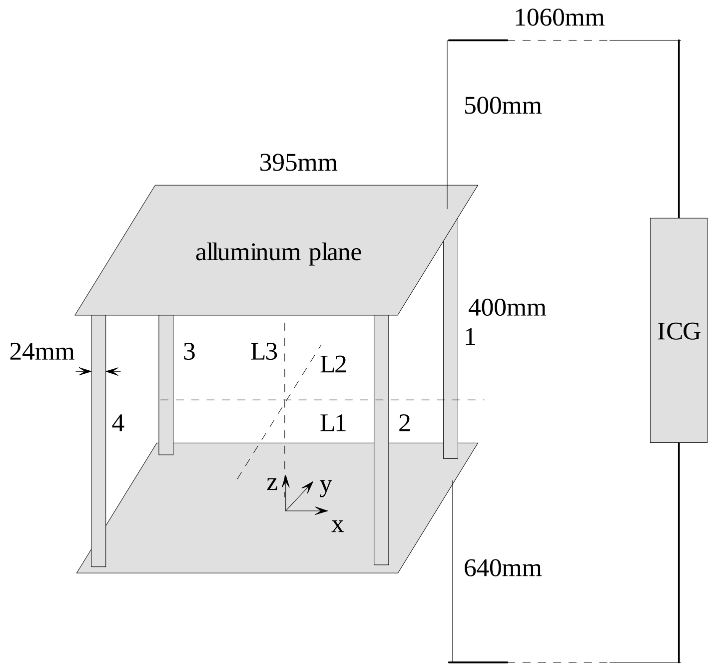

Figure 9.26 Configuration of an aluminum wire-plate structure

To validate the HANEC modeling technique for a wire-grid structure, the experimental model in the experiment was set up in the lab, as shown in Figure 9.26. The structure used in this experiment is the same as that used in Section 9.5. One column of the structure was connected to ICG through copper wires. The rectangle loop connecting ICG and the structure was in the same plane made from Column 1 and Column 3, as shown in Figure 9.26. An impulse current with the waveform 7.8/18.9μs was generated from ICG and injected into the structure. The impulse currents in four columns were measured with the Rogowaski-CRO system. The magnetic fields in the x direction along three orthogonal lines inside the structure were measured with the tailor-made magnetic field probe. The line L1 and the line L2 were located above plate B with height of 205mm. The line L3 was between the center points of two plates.

B. Comparison of Measured and Calculated Results

1. Current Distribution in Four Columns

The peak values of the measured currents in four columns were normalized by dividing the peak value of the total current injected into the structure from ICG. Thus the shunt ratio of each column is obtained. The shunt ratios from the measurement and the calculation are illustrated in Table 9.4.

Table 9.4 Shunt ratio of four columns

Column No.	Measured (%)	Calculated (%)	Error (%)
1	41.18	41.8	1.50
2	25.22	23.9	5.24
3	18.13	19.15	5.64
4	15.47	15.15	2.06

From Table 9.4, it is noted that the measured results match with the calculated results well. The maximum error is less than 6%. It is also found that over 40% of the impulse current from ICG flows through Column 1. The remained current flows through the plates and the other three columns. Although the structure is symmetrical with respect to diagonal plate, the currents in Column 2 and Column 3 are different. This is due to the influence of the copper wires loop which connects the structure and ICG.

2. Magnetic Field Distribution inside the Wire-plate Structure

The measured magnetic fields in the x direction were normalized by dividing the total current injected into the structure. The normalized measured results together with those obtained from the HANEC modeling technique were both plotted in Figure 9.27, Figure 9.28 and Figure 9.29.

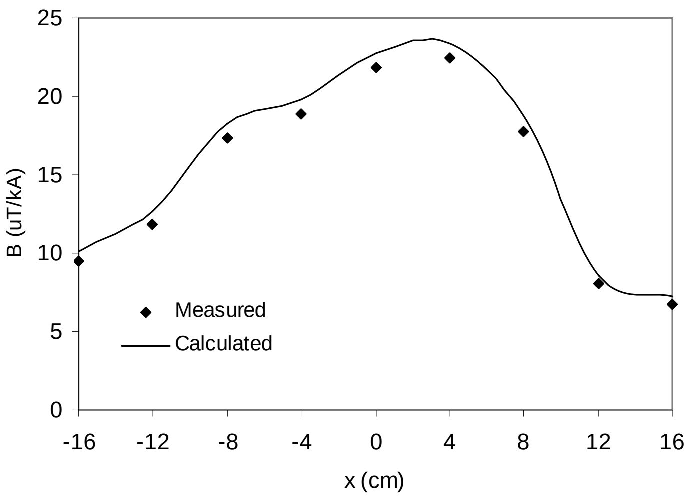

Figure 9.27 Comparison of the normalized magnetic field in the x direction along L1

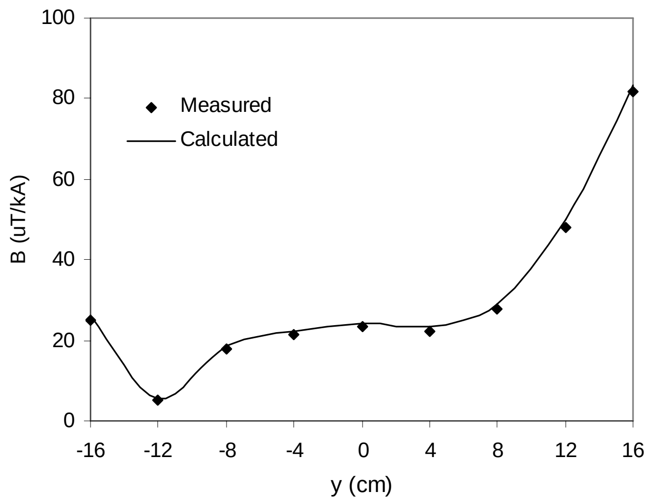

Figure 9.28 Comparison of the normalized magnetic field in the x direction along L2

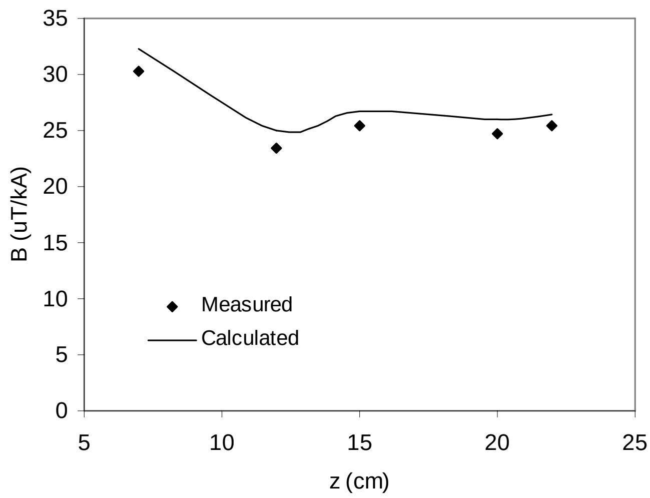

Figure 9.29 Comparison of the normalized magnetic field in the x direction along L3

From these figures, it is noted the results from the measurement and the calculation match very well. The maximum error of the field on L1 is 7.4%.The maximum error of the field on L2 is 8.3%. The maximum error of the field on L3 is 6.8%.

9.7 Summary

This chapter described four different experiments for validating and studying the proposed modeling approach for evaluating the current/field in wire-grid structures, non-ferromagnetic plates and wire-plate structure. The EC modeling approach proposed in Chapter 3 was validated experimentally when it is applied to a wire-grid structure with an isolated downconductor under a direct lightning stroke. The second and third experiment validated the PEEC modeling approach introduced in Chapter 6 when it is respectively applied on isolated aluminum plates and on an aluminum wire-plate structure inside a.c. magnetic fields. The fourth experiment validated the HANEC modeling technique proposed in Chapter 7 on an aluminum wire-plate structure under a direct lightning stroke.

Chapter 10

Conclusions and Future Work

10.1 Conclusions

It is known that electromagnetic interference due to lightning is one of the major threats to electronic equipment. To investigate protection concepts and provide mitigation methods, a study on lightning-induced impulse magnetic field (LIMF) in high-rise buildings was conducted in this thesis.

Firstly, the metal structure of buildings found in Hong Kong was introduced, which included the reinforcing concrete structure and the steel skeleton structure. Lightning protection systems (LPS) commonly adopted in high-rise buildings were reviewed. A detailed review of the studies on LIMF in literatures was conducted. The reviewed results on the modeling approaches of building structure, coaxial cable, metal plates and lightning strokes were presented.

The equivalent circuit (EC) modeling approach was proposed in this thesis to model the wire-grid structure with an isolated downconductor. The corresponding solution procedure in the time domain by using electromagnetic transient program (EMTP) was developed. Based on the EC modeling approach, LIMF in a typical building in Hong Kong was characterized and empirical formulas for evaluating the shielding effect of a wire-grid structure were derived. From the results, recommendations were presented for the protection of critical equipment in the building, as follows:

1. It is highly recommended not placing sensitive equipment in the area near the downconductor because LIMF around the downconductor is significantly high.

2. It is recommended placing the downconductor next to a column or outside the building in order to achieve significant field compensation in the area around the downconductor.

3. To enhance the field compensation further it is recommended housing the downconductor with a metal pipe, and bonding both the metal pipe and metal structure of the building together.

Metal plates are increasingly adopted in the construction of modern high-rise buildings and become part of the internal metal structure of the buildings. To study LIMF in such buildings with metal plates, a partial element equivalent circuit (PEEC) approach was proposed for modeling metal plates in the buildings. By integrating the EC modeling approach and the PEEC modeling approach, a special modeling technique, named as the hybrid analytical-numerical equivalent circuit (HANEC) modeling technique, was developed and the corresponding solution procedure in the frequency domain was provided. With the HANEC modeling technique, LIMF inside a scaled wire-plate structure was characterized. From the characterization results, it was concluded that a wire-plate structure could attenuate LIMF significantly and its shielding effect is much superior to that of a wire-grid structure.

Finally, four experiments were conducted in the laboratory to validate the proposed modeling approaches and technique in this thesis. By comparing the experimental results and the simulation results, it was proved that the EC modeling approach for a wire-grid structure, the PEEC modeling approach for non-ferromagnetic plates and the HANEC modeling technique for a wire-plate structure are all adequate to provide an accurate evaluation of LIMF.

10.2 Future Works

In order to study LIMF in a building with metal plates, the PEEC modeling approach and the HANEC modeling technique were proposed to model the wire-plate structure of the building in this thesis. These two approaches are available for non-ferromagnetic plates, e.g. aluminum plates. In the practical engineering, ferromagnetic plates such as steel plates are also widely applied to reduce the construction cost. At this time, the proposed modeling approaches are not applicable. In order to study LIMF in a building with ferromagnetic plates, a new modeling approach for ferromagnetic plates is expected to be developed in future. LIMF distribution inside a building with ferromagnetic plates is also expected to be characterized in future. From the characterization results, guideline and recommendation will be provided for practical engineers to protect sensitive equipment against LIMF.

Appendix A

Formulas to Calculate Partial Parameters in Non-ferromagnetic Plates for ELF

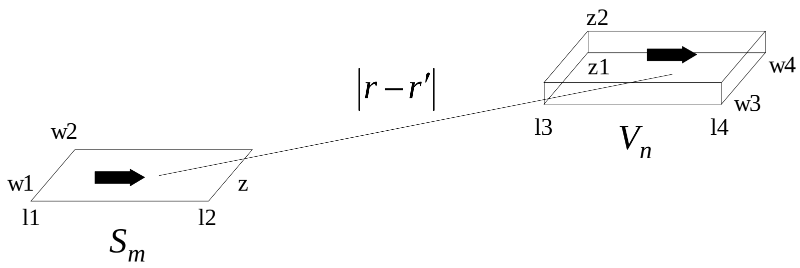

Figure app.A.1 A cell and a layer in partial inductance calculation

Equation (6.36) and (6.37) in Chapter 6 which is used to calculate the partial inductance and partial potential coefficient for extremely low frequency (ELF) are rewritten as follows

$$\begin{aligned} M_{mn} &= \frac{u}{4\pi w_{21}} \int_{S_m} \int_{V_n} \frac{1}{|r-r'|} dSdV \\ &= \frac{j\omega u_0}{4\pi w_{21}} T_{mn} \end{aligned} \tag{app.A.1}$$

$$\begin{aligned} P_{mn} &= \frac{1}{4\pi\varepsilon_0 S_m} \int_{S_m} \int_{V_n} \frac{1}{|r-r'|} dSdV \\ &= \frac{1}{4\pi\varepsilon_0 S_m} T_{mn} \end{aligned} \tag{app.A.2}$$

where $w_{21} = w_2 - w_1$. S_m is the center layer area of the potential cell m.

T_{mn} in (app.A.1) and (app.A.2) is a general five-folds integration which is expanded as follows

$$
\begin{aligned}
T_{mn} &= \int_{S_m}\int_{V_n}\frac{1}{|r-r'|}dSdV \\
&= \int_{d_1}^{d_2}\int_{w_1}^{w_2}\int_{w_3}^{w_4}\int_{l_1}^{l_2}\int_{l_3}^{l_4}\frac{dx_1dx_2dy_1dy_2dz'}{\sqrt{(x_1-x_2)^2+(y_1-y_2)^2+(z'-z)^2}}
\end{aligned}
\qquad \text{(app.A.3)}
$$

The meanings of the variables are illustrated in Figure app.A.1.

Equation (app.A.3) can be simplified and integrated under following three situations.

1. When the distance between two cells is much larger than width, length and thickness of the cell , there is

$$
T_{mn} = \frac{d_{21}l_{21}l_{43}w_{21}w_{43}}{\sqrt{(x_{i1}-x_{i2})^2+(y_{i1}-y_{i2})^2+(z_{i1}-z)^2}} \qquad \text{(app. A.4)}
$$

where $x_{i1}, y_{i1,} z_{i1}$ and x_{i2}, y_{i2} are respectively the coordinate of center point inside cell and the layer. $d_{21} = d_2 - d_1$, $l_{21} = l_2 - l_1$, $l_{43} = l_4 - l_3$, $w_{21} = w_2 - w_1$ and $w_{43} = w_4 - w_3$.

2. When the distance between two cells is comparable to the width and length of cells, but much larger than the distance in the z direction, (app.A.3) is simplified, as follows

$$T_{mn} = d_{21} \int_{w_1}^{w_2} \int_{w_3}^{w_4} \int_{l_1}^{l_2} \int_{l_3}^{l_4} \frac{dx_1 dx_2 dy_1 dy_2 dz'}{\sqrt{(x_1 - x_2)^2 + (y_1 - y_2)^2}}$$

$$= d_{21} \int_{w_1}^{w_2} \int_{w_3}^{w_4} \begin{bmatrix} -l_{24} \sinh^{-1}\left(\frac{l_{24}}{y_1 - y_2}\right) \\ +l_{14} \sinh^{-1}\left(\frac{l_{14}}{y_1 - y_2}\right) \\ -l_{13} \sinh^{-1}\left(\frac{l_{13}}{y_1 - y_2}\right) \\ +l_{23} \sinh^{-1}\left(\frac{l_{23}}{y_1 - y_2}\right) \\ +\sqrt{(y_1 - y_2)^2 + l_{24}^2} \\ -\sqrt{(y_1 - y_2)^2 + l_{14}^2} \\ -\sqrt{(y_1 - y_2)^2 + l_{23}^2} \\ +\sqrt{(y_1 - y_2)^2 + l_{13}^2} \end{bmatrix} dy_1 dy_2 \qquad \text{(app. A. 5)}$$

where $d_{21} = d_2 - d_1$, $l_{24} = l_2 - l_4$, $l_{14} = l_1 - l_4$, $l_{23} = l_2 - l_3$ and $l_{13} = l_1 - l_3$.

The complete integration result of (app.A.5) is very complicated. A two-dimensional numerical integration with Gaussian Quadratures Algorithm can simplify and accelerate the integration.

3. When the cell and the layer are very close, especially the layer is inside the cell, no approximation can be adopted. The integration result of (app.A.3) is given by

$$T_{mn} = \int_{d_1}^{d_2}\int_{w_1}^{w_2}\int_{w_3}^{w_4} \begin{bmatrix} -l_{24}\sinh^{-1}\left(\frac{l_{24}}{A}\right) \\ +l_{14}\sinh^{-1}\left(\frac{l_{14}}{A}\right) \\ -l_{13}\sinh^{-1}\left(\frac{l_{13}}{A}\right) \\ +l_{23}\sinh^{-1}\left(\frac{l_{23}}{A}\right) \\ +\sqrt{A^2+l_{24}{}^2} \\ -\sqrt{A^2+l_{14}{}^2} \\ -\sqrt{A^2+l_{23}{}^2} \\ +\sqrt{A^2+l_{13}{}^2} \end{bmatrix} dy_1 dy_2 dz' \qquad \text{(app.A.6)}$$

where $A = \sqrt{\left(y_1 - y_2\right)^2 + \left(z' - z\right)^2}$.

Since the complete integration result of (app.A.6) is extremely complicated, a three-dimensional numerical integration with Gaussian Quadratures Algorithm can be used to simplify and accelerate the integration.

Appendix B

Formulas to Calculate Partial Parameters in Non-ferromagnetic Plates for Full-wave Frequency

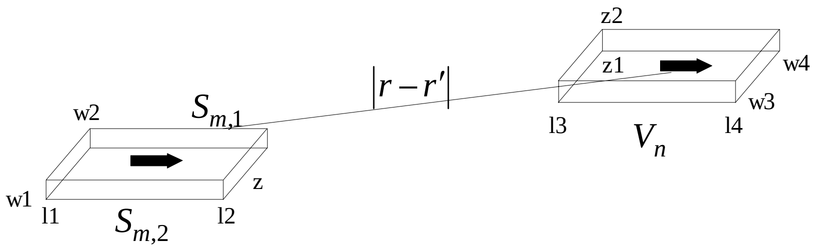

Figure app.B.1 A cell and two layers in partial inductance calculation

Equation (6.42), (6.43) and (6.44) in Chapter 6 which are used to calculate the partial inductance and partial potential coefficient for full-wave frequency are rewritten as follows

$$
\begin{aligned}
M_{m1,n} &= \frac{u_0}{4\pi w_{21}} \int_{S_{m,1}} \int_{V_n} \frac{e^{-z/\tau}}{|r-r'|} dSdV \\
&= \frac{u_0}{4\pi w_{21}} T_1
\end{aligned}
\tag{app.B.1}
$$

$$
\begin{aligned}
M_{m2,n} &= \frac{u_0}{4\pi w_{21}} \int_{S_{m,2}} \int_{V_n} \frac{e^{-(d-z)/\tau}}{|r-r'|} dSdV \\
&= \frac{u_0}{4\pi w_{21}} T_2
\end{aligned}
\tag{app.B.2}
$$

$$
\begin{aligned}
P_{mn} &= \frac{1}{4\pi\varepsilon_0 S_m} \int_{S_m} \int_{V_n} \frac{1}{|r-r'|} dSdV \\
&= \frac{1}{4\pi\varepsilon_0 S_m} T_{mn}
\end{aligned}
\tag{app.B.3}
$$

where $w_{21} = w_2 - w_1$, $S_{n,1}$ and $S_{n,2}$ are, respectively, the upper and lower layer of current cell m . S_m is the center layer area of the potential cell m .

It is found that the formula for calculate the partial potential coefficient P_{mn} is identical to that in ELF which has been discussed in Appendix A. The resultant T_{mn} in Appendix A can be applied to calculate P_{mn} here directly.

T_1 and T_2 in (app.B.1) and (app.B.2) can be represented by a general expression T_{FW} with five-folds integration

$$\begin{aligned} T_{FW} &= \int_{S_m} \int_{V_n} \frac{K_1 e^{-K_2 z}}{|r - r'|} dSdV \\ &= K_1 \int_{d_1}^{d_2} \int_{w_1}^{w_2} \int_{w_3}^{w_4} \int_{l_1}^{l_2} \int_{l_3}^{l_4} \frac{e^{-K_2 z} dx1dx2dy1dy2dz}{\sqrt{(x_1 - x_2)^2 + (y_1 - y_2)^2 + (z_0 - z)^2}} \end{aligned} \qquad \text{(app. B.4)}$$

where $K_1 = 1, K_2 = 1/\tau$ for (app. B.1) and $K_1 = e^{-d/\tau}, K_2 = 1/\tau$ for (app. B.2). The meanings of the variables are given in Figure app.B.1.

1. When the distance between two cells is much large than width, length and thickness of the cell , there is

$$T_{FW} = -K_1 \frac{l_{21} l_{43} w_{21} w_{43}}{\sqrt{(x_{i1} - x_{i2})^2 + (y_{i1} - y_{i2})^2 + (z_{i1} - z)^2}} \frac{e^{-K_2 d_{21}}}{\tau} \qquad \text{(app. B.5)}$$

where $x_{i1}, y_{i1,} z_{i1}$ and x_{i2}, y_{i2} are respectively the coordinate of center point inside cell and the layer. $d_{21} = d_2 - d_1$, $l_{21} = l_2 - l_1$, $l_{43} = l_4 - l_3$, $w_{21} = w_2 - w_1$ and $w_{43} = w_4 - w_3$.

2. When the distance between two cells is comparable to the width and length of cells, but much larger than the distance in the z direction, (app.B.4) can be simplified to

$$T_{FW} = -\frac{K_1}{K_2} e^{-K_2 d_{21}} \int_{w_1}^{w_2} \int_{w_3}^{w_4} \int_{l_1}^{l_2} \int_{l_3}^{l_4} \frac{dx_1 dx_2 dy_1 dy_2 dz'}{\sqrt{\left(x_1 - x_2\right)^2 + \left(y_1 - y_2\right)^2}}$$

$$= -\frac{K_1}{K_2} e^{-K_2 d_{21}} \int_{w_1}^{w_2} \int_{w_3}^{w_4} \begin{bmatrix} -l_{24} \sinh^{-1}\left(\dfrac{l_{24}}{y_1 - y_2}\right) \\ +l_{14} \sinh^{-1}\left(\dfrac{l_{14}}{y_1 - y_2}\right) \\ -l_{13} \sinh^{-1}\left(\dfrac{l_{13}}{y_1 - y_2}\right) \\ +l_{23} \sinh^{-1}\left(\dfrac{l_{23}}{y_1 - y_2}\right) \\ +\sqrt{\left(y_1 - y_2\right)^2 + l_{24}{}^2} \\ -\sqrt{\left(y_1 - y_2\right)^2 + l_{14}{}^2} \\ -\sqrt{\left(y_1 - y_2\right)^2 + l_{23}{}^2} \\ +\sqrt{\left(y_1 - y_2\right)^2 + l_{13}{}^2} \end{bmatrix} dy_1 dy_2 \qquad \text{(app. B.6)}$$

where $d_{21} = d_2 - d_1$, $l_{24} = l_2 - l_4$, $l_{14} = l_1 - l_4$, $l_{23} = l_2 - l_3$ and $l_{13} = l_1 - l_3$.

The complete integration result of (app.B.6) is very complicated. A two-dimensional numerical integration with Gaussian Quadratures Algorithm can simplify and accelerate the integration.

3. When the cell and the layer is very close, especially the layer is inside the cell, no approximation can be adopted. The integration result of (app.B.4) is transformed to

$$T_{FW} = K_1 \int_{d_1}^{d_2} \int_{w_1}^{w_2} \int_{w_3}^{w_4} e^{-K_2 z} \begin{bmatrix} -l_{24} \sinh^{-1}\left(\dfrac{l_{24}}{A}\right) \\ +l_{14} \sinh^{-1}\left(\dfrac{l_{14}}{A}\right) \\ -l_{13} \sinh^{-1}\left(\dfrac{l_{13}}{A}\right) \\ +l_{23} \sinh^{-1}\left(\dfrac{l_{23}}{A}\right) \\ +\sqrt{A^2 + l_{24}{}^2} \\ -\sqrt{A^2 + l_{14}{}^2} \\ -\sqrt{A^2 + l_{23}{}^2} \\ +\sqrt{A^2 + l_{13}{}^2} \end{bmatrix} dy_1 dy_2 dz \qquad \text{(app.B.7)}$$

where $A = \sqrt{\left(y_1 - y_2\right)^2 + \left(z_0 - z\right)^2}$.

Since the complete integration result of (app.B.7) is extremely complicated, a three-dimensional numerical integration with Gaussian Quadratures Algorithm can be used to simplify and accelerate the integration.

Reference

Ala G., Buccheri P. and Campoccia A., 1993, High frequency coupling among buried electrodes, *CIGRE Symposium on Power System Electromagnetic Compatibility*, pp.300-305

Ala G., Buccheri P., Francomano E. and Tortorici A., 1994, An advanced algorithm for transient analysis of grounding systems by Moments Method, *IEEE 2nd International Conference on Computation in Electromagnetic*, pp.363-366

Ala G., Francomano E., and Tortorici A., 2000, The method of moments for electromagnetic transients in grounding systems on distributed memory multiprocessors, *Parallel Algorithms Application Journal*, Vol. 14, No. 3, pp.213-233

Alvarado F. L. and Betancourt R., 1983, An accurate closed-form approximation for ground return impedance calculations, *Proceedings of the IEEE*, Vol.71(2), pp.279-280

Ametani A., Kasai Y., Sawada J., Amochizuki A. and Yamada T., 1994, Frequency-dependent impedance of vertical conductors and a multiconductor tower model, *IEE Proceedings Generation, Transmission and Distribution*, Vol 141, No. 4, pp.339-345

Antonini G., Cristina S. and Orlandi A., 1998, PEEC modeling of lightning protection systems and coupling to coaxial cables, *IEEE Transactions on Electromagnetic Compatibility*, Vol. 40, pp.481-491

Arrillaga J., 2001, Computer modeling of electrical power systems, Chichester, New York : John Wiley & Sons

Beierl O. and Steinbigler H., 1989, Simplified and fast estimation of induced voltages caused by lightning currents, *The 6th International Symposium on High-Voltage Engineering*, New Orleans, LA, Aug. 28-Sept.1, pp.635-638

Binns K. J., Kaurenson P. J. and Trowbridge C. W., 1992, The analytical and Numerical solution of electric and magnetic fields, Wiley Publisher

BS 6651, 1999, Code of Practice for Protection of Structures against Lightning, British Standard Institution

Buccella C., Cristina S. and Orlandi A., 1992, Frequency analysis of the induced effects due to the lightning stroke radiated electromagnetic field, *IEEE Transactions on Electromagnetic Compatibility*, Vol. 34, pp.338-344

Buccella C. and Orlandi A., 2000, Induced potentials inside vessels containing flammable liquids during direct lightning strike, *Conference Record of IEEE 2000 Industry Applications Conference*, Vol. 1, pp. 670–674

Buccella C., 2001, Calculation of current distribution in a lightning stroked metal structure considering the nonlinear ground impedance, *Conference Record of IEEE 2001 Industry Applications Conference*, Thirty-Sixth IAS Annual Meeting., Vol.4, pp.2703-2708

Buccella C. and Feliziani M., 2003, A Hybrid Model to Compute the Effects of a Direct Lightning Stroke on Three-Dimensional Structures, *IEEE Transaction on Magnetic*, Vol.39, No.3, pp.1586-1589

Bueno, 2001, Inductance and force calculations in electrical circuits, Nova Science Publishers, Huntington, New York

Bueno and Marcelo de Almeida, 2001, Inductance and force calculations in electrical circuits, Huntington, N.Y.: Nova Science Publishers

Carson J. R., 1926, Wave propagation in overhead wires with ground return, *Bell System Technical Journal*, Vol.5, pp.539-554

Chisholm W. A. and Janischewskyj W., 1988, Lightning surge response of ground electrodes, *The IEEE/PES 1988 Summer Meeting*, Portland, Oregon, pp.24-29

Clayton R. P., 1994, Analysis of Multiconductor Transmission Lines, New York, Wiley

Cristina S., Amore M. D. and Orlandi A., 1989-1, Lightning stroke to a structure protection system—Part I: Current distribution analysis, *The 6th International Symposium on High-Voltage Engineering*, New Orleans, LA, Aug. 28-Sept. 1, pp.104-108

Cristina S., Amore M. D. and Orlandi A., 1989-2, The Electromagnetic Environment in A Structure Stroke by lightning, *Proceedings of the IEEE International Symposium on Electromagnetic Compatibility*, Nagoya, Japan, pp.670-675

Cristina S. and Orlandi A., 1990-1, Current distribution calculation in a lightning stroked structure in presence of nonlinear ground impedance, *Proceedings of the 20th International Conference on Lightning Protection (ICLP7)* , Interlaken, Switzerland, Sept. 24-28

Cristina S. and Orlandi A., 1990-2, Lightning channel's influence on currents and electromagnetic fields in a building struck by lightning, *IEEE International Symposium on Meeting on Electromagnetic Compatibility*, Aug.21-23, pp.338-342

Cristina S. and Orlandi A., 1991, EMC effects of the lightning protection system: Shielding properties of the roof grid, *IEEE 1991 International Symposium on Electromagnetic Compatibility*, Vol. 1, pp.78-83

Cortina S. and Porrino A., 1992, Calculation of impulse current distributions and magnetic fields in lightning protection structures - a computer program and its laboratory validation, *IEEE Transactions on Magnetism*, Vol. 28, pp.1134-1137

Cristina S. and Orlandi A., 1992, Calculation of the induced effects due to a lightning stroke, *IEE Proceedings, Part B: Electric Power Applications*, Vol.139, No. 4, pp.374–380

Darveniza M. and Sargent M. A, 1979, Modeling for lightning performance calculations, *IEEE Transactions on Power Apparatus and Systems*, Vol. PAS-98, pp.1900-1908

Das B. N. and Chakrabarty S. B., 1997, Capacitance and charge distribution of two cylindrical conductors of finite length, *IEE Proceedings: Science, Measurement and Technology*,Vol.144, No.6, pp.280-286

Dawalibi F. and Selby A., 1993, Electromagnetic fields of energized conductors, *IEEE Transactions on Power Delivery*, Vol. 8, pp.1275-1284

Dawalibi F., Xiong W., and Ma J., 1995, Transient performance of substation structures and associated grounding systems, *IEEE Transactions on Industry Applications*, Vol. 31, pp.520-527

DeriA., Tevan G., Semlyen A. and Castanheira A., 1981, The complex ground return plane: a simplified model for homogeneous and multi-layer earth return, *IEEE Transactions on Power Apparatus and Systems*, Vol.PAS-100, pp.3686—3693

Dommel H. W., 1986, EMTP Theory Book, BP Administration

Du Y, Chen. S. M. and Burnett J., 2001, Experimental and Numerical Evaluation of Surge Current Distribution in Building During a Direct Lightning Stroke, *HKIE Transaction*, Vol. 8, No.1, pp.4-6

ESET Ltd. Company, 1998, E.F. Carrier System of Lightning Protection, the product manual of ESET Ltd. Company

Feliziani M. and Orlandi A., 1989, Lightning stroke to a structure protection system-Part II: Electromagnetic fields analysis, *The 6th International Symposium on High-Voltage Engineering*, New Orleans, LA, Aug. 28-Sept. 1, pp.109-112

French Standard NF C 17-102, 1995, Lightning Protection - Protection of Structures and Open Areas against Lightning Using Early Streamer Emission Air Terminals

Gary C., 1976, Approche complète de la propagation multifilaire en haute fréquence par utilisation des matrices complexes, *EDF Bulletin de la Direction des Études et echerches*, Série B, No.3/4, pp. 5-20

Gasinovi G., Geri A. and Veca G. M., 1989, Magnetic field near a concrete wall during a lightning stroke, *IEEE transaction on Magnetics*, Vol. 25(5), pp. 4006-4008

Geri A. and Veca G. M., 1991, A complete lightning protection system simulation in the EMI analysis, *IEEE 1991 International Symposium on Electromagnetic Compatibility*, pp.90-95

Geri A., 1999, Behavior of grounding systems excited by high impulse currents: The model and its validation, *IEEE Transactions on Power Delivery*, Vol.14, No. 3, pp.1008-1017

Grcev L. and Dawalibi F., 1990, An electromagnetic model for transients in grounding systems, *IEEE Transactions on Power Delivery*, Vol. 5, pp.1773-1781

Grcev L., 1994, Analysis of the possibility of soil breakdown due to lightning in complex and spacious grounding systems, *The 22nd International Conference on Lightning Protection (ICLP 94)* , Vol.1, pp.86-91

Grcev L., 1996, Computer analysis of transient voltages in large grounding systems, *IEEE Transactions Power Delivery*, Vol.11, pp.815-823

Grcev L. and Heimbach M., 1997, Frequency dependent and transient characteristics of substation grounding systems, *IEEE Transactions on Power Delivery*, Vol. 12, pp.172-178

Grover F. W., 1946, Inductance Calculations- Working Formulas and Tables, Van Nostrand, New York

Guido A. and Maria L. D. S., 2002, A Simulation Model for Electromagnetic Transients in Lightning Protection Systems, *IEEE Transactions on Electromagnetic Compatibility*, Vol. 44, No.4, pp.539-554

Gunter W. and Andre G., 1999, Analysis of 3-D Interconnect Structure with PEEC Using Spice, *IEEE Transactions on Electromagnetic Compatibility*, Vol.41, No.4, pp.412-417

Gupta B. R. and Thapar B., 1980, Impulse impedance of grounding grids, *IEEE Transactions on Power Apparatus and Systems*, Vol. 99, pp.2357-2362

Gutiérrez J. A., Moreno P., Naredo J. L. and Guardado L.,2001, Non uniform line tower model for lightning transient studies, *The International Conference on Power Systems Transients*, Rio de Janeiro, Brazil, Jun. 24–28,

Harrington R. F, 1968, Field computation by moment methods, Macmillan, New York

Heidler F., Cvetic J. M. and Stanic B. V., 1999, Calculation of Lightning Current Parameters, *IEEE Transaction on Power Delivery*, Vol. 14, No.2, pp.399-404

IEC Standard 61024-1-2, 1998, Protection of Structures Against Lightning—Part 1–2: General Principles—Guide B—Design, Installation, Maintenance and Inspection of Lightning Protection Systems

IEC Standard 61312-2, 1995, Protection against Lightning Electromagnetic Impulse Part 2: Shielding of Structures, Bonding inside Structures and Earthing

Karwowski A. and Zeddam A., 1995, Transient currents on lightning protection systems due to the indirect lightning effect, *IEE Proceedings: Science, Measurement and Technology*, Vol. 142, No. 3, pp.213-222

Li G. F., Zheng J. C., 1998, Lightning current distribution calculation for metallic structures, *Proceedings of POWERCON '98. 1998 International Conference on Power System Technology*, Vol.1, pp.18-21

Liew C. and Darveniza M., 1974, Dynamic model of impulse characteristics of concentrated earth, *Proceedings of the Institution of Electrical Engineers* (London), Vol. 121, no. 2, pp.123-135

Marcelo A. B. and Andre K. T. A., 2001, Inductance and Force Calculations in Electrical Circuits, Nova Science Publishers Inc.

Mattos M. A. F. and Caixeta G. P., 1992, Interaction structure lightning and the generated electromagnetic fields, *IEEE symposium on Electromagnetic Compatibility' 92*, Beijing, China, pp.281-285

Mazzetti C. and Veca G. M., 1983, Impulse behavior of grounding electrodes, *IEEE Transactions on Power Apparatus and Systems*, Vol. PAS-102, pp.3148-3156

Meliopoulos A. P. and Moharam M. G., 1983, Transient analysis of power systems, *IEEE Transactions on Power Apparatus and Systems*, Vol. PAS-102, pp.389-399

Meliopoulos A. P., 1988, Power System Grounding and Transients, Marcel Dekker, New York, NY, U.S.A.

Menter F. and Grcev L., 1994, EMTP-Based model for grounding system analysis, *IEEE Transactions on Power Delivery*, Vol. 9, pp.1838-1849

Morita N., Kumagai N. and Mautz J. R., 1990, Integral Equation Methods for Electromagnetics, Boston , Artech House

Mousa A. M., 1994, The soil ionization gradient associated with discharge of high currents into concentrated electrodes, *IEEE Transactions on Power Delivery*, Vol. 9, pp.1669-1677

Orlandi A., 1991, EMC effects of the lightning protection systems shielding properties of the roof-grid, *IEEE International Symposium on Electromagnetic Compatibility*, Cherry Hill, NJ, pp.78-83

Orlandi A., 1995, Attenuation of electric field by small reinforced concrete building: measured and computed results, *IEICE Transactions on Communications, Special Issue on Electromagnetic Compatibility*, Vol. E78-B, No. 2, pp.212-217

Orlandi A., Piparo G. B. L and Mazzetti C., 1995, Analytical expressions for current share by means of a lightning protection system model, *European Transactions on Electrical Power Engineering/ETEP*, Vol. 5, No. 2, pp.1-8

Orlandi A., Lo Piparo G. B. and Mazzetti C., 1995, Analytical expressions for current share in lightning protection systems, *European Transactions on Electrical Power Engineering(ETEP)*, Vol. 5, No. 2, pp.107-114

Orlandi A. and Schietroma F., 1996, Attenuation by a lightning protection system of induced voltages due to direct strikes to a building, *IEEE Transactions on Electromagnetic Compatibility*, Vol. 38, pp.43-50

Orlandi A., 1996, Lightning induced transient voltages in presence of complex structures and nonlinear loads, *IEEE Transactions on Electromagnetic Compatibility*, Vol. 38, pp.150-155

Orlandi, A. and Schietroma F., 1996, Attenuation by a lightning protection system of induced voltages due to direct strikes to a building, *IEEE Transactions on Electromagnetic Compatibility*, Vol. 38, pp. 43-50

Orlandi A., Mazzetti C., Flisowski Z. and Yarmarkin M., 1998, Systematic approach for the analysis of the electromagnetic environment inside a building during lightning strike, *IEEE Transactions on Electromagnetic Compatibility*, Vol. 40, pp.521-535

Orlandi, A., Mazzetti C., Flisowski Z. and Yarmarkin M., 1998, Systematic approach for the analysis of the electromagnetic environment inside a building during lightning strike, *IEEE Transactions on Electromagnetic Compatibility*, Vol. 40, pp.521-535

Papagiannis, G. K., Triantafylids D. G. and Labrids D. P., 2000, One-step finite element formulation for the modeling of single and double-circuit transmission lines, *IEEE Transactions on Power Systems*, Vol.15, No.1, pp.33-38

Papalexopoulos A. D. and Meliopoulos A. P., 1987, Frequency dependent characteristics of grounding systems, *IEEE Transactions on Power Delivery*, Vol. PWRD-2, pp.1073-1081

Paul C. R., 1994, Anaylsis of multiconductor transmission lines, Wiley-Interscience Publication, New York

Pollaczek F., 1926, Uber das feld einer unendlich langen wechselstromdurchflossenen Einfachleitung, *Elektrische Nachrichlen Technik*, Vol.3(9), pp.339-359

Pollaczek F., 1931, Sur le champ produit par un conducteur simple infiniment long parcouru par un courant alternatif, *Revue Générale d'Électricité*, Vol.29(22), pp.851-867

Rakov V. A. and Uman M. A., 1998, Review and evaluation of lightning return stroke models including some aspects of their application, *IEEE Transactions on Electromagnetic Compatibility*, Vol. 40 , Issue: 4, pp.403-426

Rakov V. A. and Uman M. A., 2003, Lightning : physics and effects, Cambridge ; New York : Cambridge University Press

Ramamoorty M., Narayanan M. M. B., Parameswaran S., and Mukhedkar D., 1989, Transient performance of grounding grids, *IEEE Transactions on Power Delivery*, Vol. 4, pp.2053-2059

Ramo Simon, 1994, Fields and Waves in Communication Electronics, New York :

Wiley

Rao S. M., Sarkar T. K. and Harrington R. F., 1984, The Electrostatic Field of Conducting Bodies in Multiple Dielectric Media, *IEEE Transactions on microwave theory and techniques*, Vol.Mtt-32, No.11, pp.1441-1448

Roger E. J. and White J. F., 1990, Mutual coupling between horizontal earth return conductors using actual routing parameters, *IEEE Transactions on Power Delivery*, Vol.5 , Issue 3 , pp.1266 -1274

Roymand Wong Wai Man, 1998, 15 Most Outstanding Projects in Hong Kong, *China Trend Building Press Ltd*

Roymand Wong Wai Man, 2003, International Finance Center, Phase II, *Construction & Contract News*, No. 1,

Rubinstein M. and Uman M. A., 1991, Transient electric and magnetic fields associated with establishing of finite electrostatic dipole, revisited, *IEEE Transactions on Electromagnetic Compatibility*, Vol. 33, Issue 4, pp. 312-330

Ruehli A. E., 1972, Inductance calculation in a complex integrated circuit environment, IBM J. Res. Develop., Vol. 16, pp. 470-481

Ruehli A. E., 1974, Equivalent circuit models for three-dimensional multiconductor systems, *IEEE Transactions on Microwave Theory Technology*, Vol. MTT-22, pp.216-221

Ruehli A. E., Garret J. and Paul C. R., 1993, Circuit models for 3-D structures with incidents fields, *in Proc. IEEE International Symposium Electromagnetic Compatibility*, Dallas, TX, pp.28-32

Sartori C. A. F. and Cardoso J. R., 1994, Evaluation of electromagnetic environment around a structure during a lightning stroke, *International Symposium on Electromagnetic Compatibility*, Rome, Italy, pp.246-251

Sartori C. A. F. and Cardoso J. R., 1995, EMC aspects in a steel structure struck by lightning, *in Proc. IEEE International Symposium on Electromagnetic Compatibility*, Atlanta, GA, pp.248-252

Sartori C. A. F., Cardoso J. R. and Orlandi A., 1998, Transient induced voltage computation in a high building struck by lightning, *IEEE Transaction on Magnetic*, Vol. 34, pp.2815-2818

Shi L.H, Li Y.X. and et al., 2003, Experimental Research on the Susceptibility of Intelligent Control System to EMP (in Chinese), *Lightning Protection and Standardization*, Vol. 3 , pp.18-21

Stevenson W. D., 1962, Elements of Power System Analysis. Second Edition. New York: McGraw-Hill

Takahashi H. and Kodama M., 2002, Theoretical derivation of surge impedance about a vertical conductor, *Transmission and Distribution Conference and Exhibition 2002: Asia Pacific. IEEE/PES*, Vol.2, pp.688- 693

Triantafyllidis D.G., Papagiannis G. K. and Labridis D. P., 1999, Calculation of overhead transmission line impedances: a finite element approach, *IEEE Transactions on Power Delivery*, Vol.14(1), pp.287-293

Uman M. A. and Rubinstein M., 1988, Methods for calculating the electromagnetic fields from a known source distribution: Application to lightning, *IEEE Transactions on Electromagnetic Compatibility*, Vol. 31, pp.183-189

Uman M. A., McLain D. K. and Kreider E. P.,1975, The electromagnetic radiation from a finite antenna, *Amer. J. Phys*., Vol. 43, pp.33-38

Velasquez R. and Mukhedkar D., 1984, Analytical modeling of grounding electrodes transient behavior, *IEEE Transactions on Power Apparatus and Systems*, Vol. PAS-103, Issue 6, pp.1314-1322

Verma R. and Mukhedkar D., 1981, Fundamental considerations and impulse impedance of grounding grids, *IEEE Transactions on Power Apparatus and Systems*, Vol. 100, pp.1023-1030

Wolfgang Schueller, 1995, The Design of Building Structures, Prentice Hall, Upper Saddle River, New Jersey

Woodruff L.F., 1938, Principles of Electric Power Transmission. 2nd Edition. New York: Wiley

Xiong W. and Dawalibi F., 1994, Transient performance of substation grounding systems subjected to lightning and similar surge current, *IEEE Transactions on Power Delivery*, Vol. 9, pp.1421-1427

Xu L., Du Y. and Zhou Q. B., 2004, The magnetic field and induced current arising from a cylindrical shell loop with an unbalanced current, *Electric Power System Research*, Vol.71, No.1, pp.21-26